Vision-based Sensing Mechanism for Soft Tissue Stiffness Estimation

Faragasso, Angela

Awarding institution:
King's College London

KING'S College LONDON

University of London

Vision-based Sensing Mechanism for Soft Tissue Stiffness Estimation

Author:
Angela Faragasso

Supervisor:
Prof. Kaspar Althoefer

A thesis submitted in fulfilment of the requirements for the degree of Doctor of Philosophy in Robotics

to

King's College London
School of Natural and Mathematical Sciences
Department of Informatics
Centre for Robotics Research

September 2016

Declaration of Authorship

I, Angela Faragasso, declare that this thesis titled, 'Vision-based Sensing Mechanism for Soft Tissue Stiffness Estimation' and the work presented in it are my own. I confirm that:

- This work was done wholly or mainly while in candidature for a research degree at this University.
- Where any part of this thesis has previously been submitted for a degree or any other qualification at this University or any other institution, this has been clearly stated.
- Where I have consulted the published work of others, this is always clearly attributed.
- Where I have quoted from the work of others, the source is always given. With the exception of such quotations, this thesis is entirely my own work.
- I have acknowledged all main sources of help.
- Where the thesis is based on work done by myself jointly with others, I have made clear exactly what was done by others and what I have contributed myself.

Signed: _____

Date: _____

"Research is creating new knowledge"

NEIL ARMSTRONG

KING'S COLLEGE LONDON

Abstract

Centre for Robotics Research
Department of Informatics

Doctor of Philosophy in Robotics

Vision-based Sensing Mechanism for Soft Tissue Stiffness Estimation

by Angela Faragasso

During the last few decades, advanced instrumentations have been widely explored for research and diagnostic applications in medical and life sciences. Traditionally, these instruments have been primarily found in laboratory environments. Yet, as the technology finds its way from research facilities to the point of care, diagnostic tools are increasingly used in hospitals and other near-patient settings.

In medical diagnosis, physicians palpate the anatomical surfaces with their fingertips to assess variations in stiffness across the surface of organs. Hence, they locate abnormally stiff areas by relying on their sense of touch. However, palpation is a highly sophisticated manual skill, which can only be performed in areas that are accessible to the hands, therefore it cannot be employed in minimally invasive procedures. Several instruments have been developed with the aim of reproducing the physician's "sense of touch". These devices should be inexpensive and thus affordable to point-of-care providers. They should also be versatile so that multiple tests can be performed to improve efficiency and, at the same time, reduce costs. Moreover, since operators may not be trained technicians, these devices need to be intuitive and easy to use. Furthermore, if designed for minimally invasive procedures, they should be small enough to fit through a standard trocar port. This thesis presents a novel vision-based sensor for soft tissue stiffness estimation, measuring multiple tool-tissue interaction forces in parallel employing a set of deformable elements. By means of an analysis of the differences between the measured forces the stiffness of the material the sensor is interacting with can be computed. The motion of the deformable elements whilst in contact with the environment are captured by a camera sensor and related to force and, subsequently, to stiffness exploiting knowledge of the spring constant of the deformable elements.

The developed system provides quantitative measurements of the tissue stiffness which can be used to diagnose abnormalities. The proposed sensing principle has been used

to develop a hand-held stiffness probe for tumour identification. In order to retrieve the "sense of touch" in minimally invasive procedures, a clip-on stiffness sensor has been developed that can be integrated with a surgical endoscopic camera. The new, integrated system extends the sensing capabilities of the camera: the system can be used to visualise the anatomical areas inside the human body as well as measure the stiffness of these abdominal structures. Adding a purely mechanical device to an endoscopic camera, proves to be a cost-effective way to introduce remote stiffness measurement capabilities to minimally invasive intervention. The experimental results demonstrate the effectiveness and accuracy of the proposed system, successfully discriminating soft tissues over a wide range of tissue stiffness values. To make the system intuitive, a colour-coded stiffness map that is generated in real-time is used to visualise the stiffness distribution of the examined soft object surface. Moreover, the sensory mechanism can be manufactured at a low price, does not use any electronic components; it is easy to use and does not require any calibration. The measurement range and resolution can be easily customised.

Acknowledgements

I would first of all like to thank my supervisors Prof. Kaspar Althoefer, Dr. Thrishantha Nanayakkara and Dr. Hongbin Liu without whom I would not have had the chance to embark on, conduct and complete my PhD. In particular, Prof. Althoefer strongly believed in my potential to carry out independent research and has encouraged and supported me throughout my PhD in the course of many productive meetings.

I am thankful to my colleagues Agostino Stilli, Ali Shafti, Lukas Lindenroth, Dr. Luc Marechal, Junghwan Back, Max Escudero and Allen Jiang who supported and endured me throughout my research and the challenges I've faced by sharing their thoughts in numerous technical discussions or funny jokes. I would like also to thank Ataka Ahmad, Jim Trotter, Ali Shiva, Dr. Min Li, Dr. Shan Luo, Dr. Jelizaveta Konstantinova, Dr. Anuradha Ranasinghe, Sarah Abad Guaman, Nantachai Sornkarn, Dr. Evangelos Emmanouil, Dr.Jamie Barras and Dr. Georgia Kyriakidou. In addition, I am indebted to all my colleagues from the Centre for Robotics Research at King's College London who supported and endured me during the most difficult times when writing this thesis (thanks guys for letting me use the Skype booth!).

I would like to thank especially Dr. Helge Arne Wurdemann who believed in me and supported me from the first day I joined the group and Dr. Yohan Noh for the constant enthusiasm and for making life fun while working.

My biggest gratitude goes to my colleague and friend Dr. João Bimbo for his willingness to help me throughout my study and for his priceless scientific discussions and advice. I am also thankful to Dimitris, Ankur, Hugo, Andreas, and Vahid for making me a member of the group, their friendship and the awesome and unforgettable times we spent together.

Also I would like to thank all the friends who have been supporting me during these years. In particular, Enrica Alteri and Janis who made me feel as part of their family, my mate-sister and friend Tugba, Zeynep, Federica, Gionata, Katerina, Stefania, Damiano, Giorgia, Vito, Bani, Luciano, Faith, Umut and my best friends Angela and Jenny. A big thanks also to my student and friend Senaka.

I finish by thanking my family. Words cannot express how grateful I am to my mum Silvana and my dad Mario for their love and for all of the sacrifices they've made in my behalf; to my brother Giovanni and my sister-in-law Luisa for their moral support and encouragement throughout my life; to my nephews Davide and Alessia for the happiness and inspiration they have brought to me. My deepest gratitude goes to my sister Sabina for giving me the strength to reach out and chase my dreams.

Contents

List of Figures

List of Tables

Abbreviations

AI	**A**rtificial **I**ntelligence
MIS	**M**inimally **I**nvasive **S**urgery
PVDF	**P**oli**V**inyli**D**ene **F**louride
MEMS	**M**icro**E**lectro**M**echanical **S**ystems
FEA	**F**inite **E**lement **A**nalysis
MESA	**M**iniature **E**lectrostatic **A**ccelerometer
DOF	**D**egree **O**f **F**reedom
OpenCV	**O**pen source **C**omputer **V**ision
ROS	**R**obot **O**perating **S**ystem
CHT	**C**ircle **H**ough **T**ransform
RMSE	**R**oot **M**ean **S**quare **E**rror
FBG	**F**iber **B**ragg **G**rating
TI	**T**actile **I**maging
AJCC	**A**merican **J**oint **C**ommittee on **C**ancer
TNM	**T**umour **N**odes **M**etastasis
EP	**E**xploratory **P**rocedures
DOF	**D**egree **O**f **F**reedom
FSR	**F**orce **S**ensor **R**esistor
IGS	**I**mage **G**uided **S**urgery
EMTS	**E**lectromagnetic **T**racking **S**ystems
NDI	**N**orthern **D**igital **I**nc
DH	**D**enavit **H**artenberg
ABS	**A**crylonitrile **B**utadiene **S**tyrene
SCU	**S**ystem **C**ontrol **U**nit
SIU	**S**ensor **I**nterface **U**nit

EMA	**E**uropean **M**edicines **A**gency
FDA	**F**ood and **D**rug **A**dministration
LMA	**L**evenberg **M**arquardt **A**lgorithm

Symbols

E	Young's modulus	Pa (N/m^2)
F	force	N
k	stiffness	(N/mm)
Δx	displacement	mm
P	3D point	**P**=(X,Y,Z)
Q	pixel coordinates	**Q**=(u,v)
C	centroid	C=(C_x,C_y)
θ	pan angle	∘
α	tilt angle	∘
${}^{\mathrm{A}}T_B$	transformation matrix	

To whom believes in research

CHAPTER 1

Introduction

Over the last centuries, there have been many changes in the field of healthcare and medicine. In the 1970s, the AI boom triggered the development of diagnosis tools in the form of physical robot and software expert systems. Technological advances involving the creation of robotic devices and of complex imaging have revolutionised the medical field. However, health providers have been relatively slow to endorse robotic systems and this is due mainly to safety concerns. Nonetheless, the introduction of the first robotic surgical device in 1985 promised to dramatically change the way surgeons operate and diagnose pathologies [1]. Although the developments in medical robotics have made operations much less invasive and improved medical examination, robotics systems have disadvantages and limitations that prevent them from replacing medical experts. For instance, although highly desirable, a surgical device able to compute soft tissue stiffness in real time is still lacking. Such a device would be beneficial in medical inspection allowing quantitative measurements of the mechanical properties of soft tissues; in minimally invasive interventions, it would allow the reproduction of the sense of touch which is completely lost during non-invasive procedures. The aim of this thesis is the development of a sensory mechanism that uses vision to compute soft tissue stiffness. This chapter provides a comprehensive outline of the motivation of this thesis as well as the background to the research and its objectives, the contributions and structure of the thesis.

1.1 Background

During the last century, scientific advances have been continually reshaping the practice of medicine. From innovative tests in tertiary medical centres to the advanced technology available nowadays in outpatient settings, it is clear that new discoveries have redefined the way in which physicians diagnose, treat and alleviate diseases [2]. New methods and paradigms for training and teaching the clinicians how to perform physical examinations are continuously being proposed and tested in order to improve the diagnostic assessment. In general, clinicians learn and practice their skills during their training years and refine them with experience. The physical examination is one of the most important skill for a clinician to develop. It can also be one of the most challenging. It has been proved that skills not honed during the training stage are unlikely to improve with time. Moreover, the learning curve, that is, the rate in which experience and new skills are gained when using the latest technologies, increases for seasoned physicians.

Although the physical exam remains a milestone of clinical medicine all over the world, doctors rely on physical touch as a diagnostic tool much less than in earlier times, and the mastery of examination skills at every level of training has decreased over the years [3]. Quantification of stiffness variation may provide important diagnostic information and aid in the early detection of minor abnormalities before they become serious; therefore, there is a need for medical instruments able to reproduce the same sensations that practitioners have when performing a physical examination through direct contact, i.e. palpation of the skin and anatomical landmarks to assess mechanical properties of soft tissue.

Diagnosis can be defined as the process whereby a disease or condition is identified by examining the patient's symptoms. Formerly, few diagnostic tests were available to assist clinicians and the primary presenting symptom of a cancer was a palpable mass, often initially detected by the patient. In the 20th century, numerous technological advances in medicine occurred, resulting in the development of a range of diagnostic techniques. The fusion of physical exam, technology and research made clinical diagnoses quicker and more accurate, leading to considerable improvement of patient care. Early cancer diagnosis means a more effective therapeutic strategy, with increased chances of recovery and prolongation of the patient's life expectancy.

Manual palpation is an important determinant of both sensitivity and specificity of the diagnosis and is used by medical experts to evaluated soft tissue stiffness without extensive and expensive medical tests. However, manual palpation is not completely reliable because subjective to the clinician's experience. In response to this problem, several devices have been developed to objectively quantify tissue tone, allowing researchers to

study the effectiveness of tissue therapies used by clinicians. The mechanical properties of soft tissues have been the focus of a number of medical applications because of the diagnostic information they provide. The links between biomechanics and human diseases have been the subject of scientific research for several decades. It has been proved that an easy-to-use instrument and the use of objective methods for quantitative analysis of soft tissue stiffness is needed to enhance the outcome of the diagnosis.

1.1.1 Manual Palpation

Palpation is the traditional diagnostic technique, classically defined as the "act of feeling with the hand". It involves the examination of the patient by means of direct physical contact [4]. During physical investigation, texture, size, consistency and location of soft tissue areas are examined by clinicians using vision combined with the sensations received from their finger tips. This diagnostic technique is called "manual palpation". Manual palpation can be employed on every part of the body accessible to the examining fingers: all external structures, all the structures accessible through body orifices, the bones, the joints, superficial nerves, abdominal viscera, etcetera. In most cases, the clinician aims to evaluate the stiffness distribution of the examined soft tissue organ or body part, and to distinguish between areas of higher and lower stiffness, since these stiffness variations can indicate the presence of abnormalities. The final diagnosis is a function of kinesthetic sensations: the indentation depth (i.e. how much the soft surface deforms) and the experienced reaction force. Thus, palpation is historically one of the most effective methods used by medical experts to determine pathologies [5]. When practitioners attempt to detect tumours in some specific area of the human body, they discriminate between healthy and abnormal areas through stiffness differences, as the stiffness of a tumour is different from the surrounding healthy tissue [6], [7], [8]. For instance, during breast examination, palpation should be conducted in a methodical way and performed over the entire breast. Suspicious breast lesions are hard and fixed rather than movable, as is the case for healthy tissue. Besides, it is noted that cancerous tumours are usually not tender, whilst benign lesions are more likely to be round, elastic or firm, movable, and well-defined [9]. Similarly, with the aim of early detection of prostate cancer, a digital rectal examination (DRE) is widely used to establish the presence of a tumour and to distinguish between malignant and benign tumours. Urologists insert a gloved and lubricated finger into the rectum of the patient and palpate the posterior region of the prostate in an effort to establish whether tumours are present in the prostate or its posterior region. Due to early detection and improvements in the treatment of prostate cancer, the 5-year relative survival rate for all patients has increased from 69 % to nearly 99 % in the last 25 years [5]. During medical examination, the stiffness variation of

(a) (b)

(c) (d)

FIGURE 1.1: Medical specialities employing palpation procedure: (a) Physical examination of the armpit is performed during lymph node inspection. (b) Feline abdominal palpation is used for training and examination in veterinary medicine (c) A training device for breast cancer detection (d) Palpation of the structures of the head, neck, and oral cavity it is performed during oral examination.

the area to be examined can be detected by moving the fingertip on the soft tissue with a certain level of force and perceiving the tissue's reaction force. During a manual palpation procedure, clinicians adjust the contact depth and force on the tissue in order to obtain the best tactile feedback according to their experience. For example, if the finger tip touches an object which is a little harder and the clinician senses an increased force level during the process, the exploration can be repeated with deeper contact depth in order to enhance the tactile feeling of hardness. Therefore, the result of the diagnosis is strictly related to the exploration scheme chosen by the clinician as well as his/her experience and tactile sensitivity. Many medical specialities, such as dermatology, gynaecology, oncology, dentistry, paediatrics, veterinary medicine, employ manual palpation procedures both during consultation and intra-operatively. Some of these procedures are shown in Figure 1.1.

It is reported that the sensitivity of palpation procedures, i.e. the clinician's ability to correctly identify the tumour, is subjective and highly dependent upon the skill and

the experience of the practitioner - a skill often difficult to master [4] [10] [11]. Inadequate training may contribute to a low and variable sensitivity range during medical examination. Tactile information is crucial in the early stage of diagnosis. However, a system able to give a quantitative measurement of the tissue stiffness does not yet exist. Such a system would improve the quality of the diagnosis and help clinicians during the examination [3].

1.1.2 Surgical Palpation

Besides direct palpation on the patient's skin, palpation of organs and anatomical areas can also be performed during surgery. In open procedures, it is possible to directly access soft tissue and organs. Hence, surgeons can use their sense of touch to identify organ margins and features as well as buried structures, such as nerves or arteries and prevent undesired cuts to healthy tissue. They can directly investigate the force-displacement response to acquire distributed tactile information which is then used to identity tumours, as the mechanical proprieties of a soft tissue can be altered by a pathological condition [12]. Moreover, tactile feedback is widely used to gather valuable information about the stiffness of the tissue which is an indicator of the tissue's health. Tumorous regions that cannot be visually identified can often can be detected using tactile feedback as they tend to be harder than the surrounding healthy tissues [7] [8].

Minimally invasive surgery (MIS), also called laparoscopic or keyhole surgery, is a new surgical technique which involves operating through small surgical cuts on the patient body using long and thin instruments that are inserted in one or more trocar ports (incisions of 10/12 mm in diameter), [13] [14] [15]. Robotic-assisted procedures represent the latest development in minimally invasive surgical techniques - surgeons are provided with precision tools that enter the abdominal cavity through the same small incisions as conventional laparoscopic tools. A key difference is that the robotic system can offer precision control and often a very intuitive control of the surgical instruments. With its stereoscopic, 3-D imaging and precision-guided wrist movements, robotic-assisted systems, such as the da Vinci surgical system, allow surgeons to combine the best of both laparoscopy and regular open surgery techniques [16].

Minimally invasive surgical procedures have become a well established practice and the preferred approach over open surgeries due to the substantial benefits they provide to the patients, such as improved therapeutic outcome, shortened postoperative recovery, reduced immunological stress response of the tissue and tissue trauma, and less postoperative pain. MIS is also cost-effective [17]. However, MIS hinders the surgeon's ability

to directly manipulate the tissue [18]; it is reported that the absence of physical tissue interaction is a major limitation of MIS compared to traditional open surgeries [19].

MIS has become a well-established and preferred approach to a growing number of major surgeries ranging from relatively simple procedures such as prostatectomy [20], cholecystectomy [21], and cystectomy [22] to more complex surgical operations which are very difficult to conduct laparoscopically such as coronary artery revascularization and mitral valve repair [23] [24]. Hence, haptic (force and tactile) feedback has become essential in MIS. In palpation procedures for tumour localization, clinicians press their fingers on the patient's body to assess the interaction forces and use the tactile feedback to distinguish between different types of tissues [25]. Stiffness variation of anatomical surfaces can be used to identify abnormal tissues (such as tumorous lumps), blood vessels, ureters, as well as bones and fatty tissues [16]. Since minimally invasive tools have been proven to noticably improve the outcome of surgical operations, they have been developed beyond the investigation stage. Currently, these devices continue to evolve as they become more ergonomic [26]. Although vision has been improved in MIS through the introduction of high-definition 2D and 3D vision systems, methods of direct palpation and haptic feedback in MIS are still in their infancy. The force applied to soft organs can only be estimated through visual feedback by observing the deformation of the tissue in the transmitted camera images, as shown in Figure 1.2. The need to perform surgeries safely in limited space and dynamic environments where surgeons have a restricted view and no sense of touch has created a growing demand for surgical vision techniques and sensor systems whereby to retrieve tactile feedback similar to traditional open surgery. Analysis shows that a new design is required to address these problems that occur with the current equipment [19].

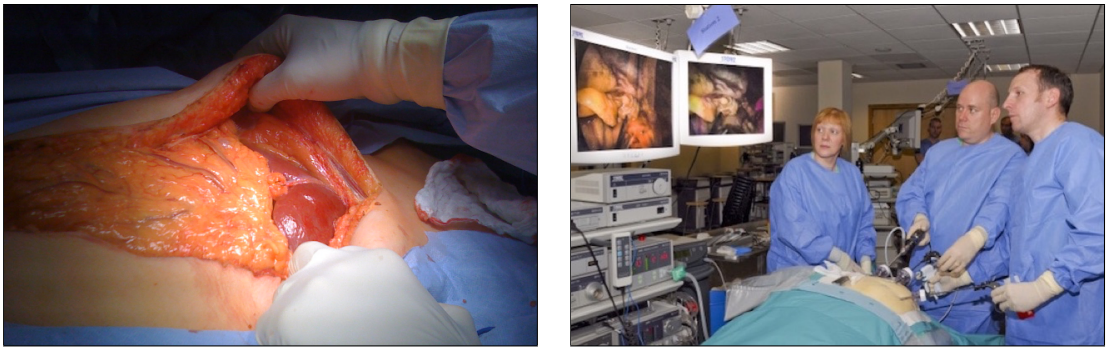

(a) (b)

FIGURE 1.2: Surgical Palpation: (a) Manual palpation of soft tissue area performed in open surgery scenario. (b) Surgical setup for a minimally invasive procedure; only visual feedback is available for the medical team to retrieve mechanical properties of the anatomical areas.

Overall, touch is an important sensory modality used by clinicians during different types of surgical procedures to identify subcutaneous or subserous inclusions such as blood vessels or tumorous that cannot be visually detected. In the last few years, researchers have increasingly developed instrumentations for soft tissue characterization which may be reliable, but are often difficult to use in a clinical setting. It is noted that, albeit highly desirable, a medical system able to provide real-time quantitative measurements of soft tissue properties such as stiffness, does not yet exist. [27] [28]. Satisfying the operating room requirements that put strict limits on size and robustness, and sterilization remain major hurdles when attempting to incorporate sensory systems in medical applications. Furthermore, the sensors must conform to surgical device regulations such as those imposed by the European Medicines Agency (EMA) or the American Food and Drug Administration (FDA) and, needless to say, ought to be made available to the customer at a reasonable cost. A very critical issue in the design of sensing instruments to be inserted inside the human body is sterilization. The most common method of sterilization is applying saturated steam to the instruments for a duration of about 15 minutes (autoclave) [29]. Therefore, any sensors used in such a device must be robust to heat, pressure and humidity. Another solution is to employ chemical agents for sterilization which increases the duration of sterilization. Equipment which cannot be sterilized by any of the sterilization methods cannot be reused and need to be economically disposed of [30].

1.1.3 Research Problem

Tactile information is crucial at the early stage of diagnosis when conditions such as breast and prostate cancer alter the elastic stiffness of tissue [8]. Manual palpation procedures are not thoroughly reliable as they are subject to human interpretation and therefore not repeatable. In response to this problem, several devices have been developed to objectively quantify the mechanical properties of soft tissue, and in particular the stiffness [31, 32].

In the last two decades, with the increased use of minimally invasive procedures in hospitals, research on palpation devices strived to restore tactile and kinesthetic sensation in minimally invasive intervention. This was pursued by performing tissue palpation with different techniques, such as indenting [33], grasping [34] or rolling [35]. These techniques have not as yet been incorporated into clinical practice. The design requirement of a palpation device for use in MIS heavily depends on the medical application it will be used in and presents several challenges in that the sensor must meet demanding size constraints, withstand temperature variations without affecting its sensing accuracy, address issues of sterilization, and use biocompatible materials, while achieving appropriate performance in terms of resolution and sensing range. Besides, surgeons do not welcome the option of devoting a surgical trocar port to an additional instrument such as a palpation device - the genreal approach is to keep the number of trocar ports, used to insert surgical instruments into the inside of the human, to a minimum. An objective in-vivo measurement technique for assessing the material properties of soft tissue will definitely be a valuable tool in the diagnosis of pathologies. For instance, a stiffness sensing tool is likely to improve the surgeon's appreciation of the tumour location and distribution within an organ such as the prostate, and thus lead to an improved outcome of a robot-assisted laparoscopic radical prostatectomy [36, 37]. The computation of the stiffness of the anatomical surfaces in minimally invasive practice will revolutionise this new technology and serve as a substitute to palpation by furnishing the surgeon with a sense of touch.

This thesis focuses on the development of a vision-based stiffness sensing mechanism. The system is composed of a camera sensor and a designed mechanical structure which encompasses elastic elements. The mechanical properties of soft tissue are computed relying only on the visual information provided by the camera. An image processing algorithm tracks the movements of the elastic mechanism in real time. A mathematical model relates the visual appearance of the elastic element in the images to the interaction forces which are used to estimate the stiffness of the examined soft tissue. Using a surgical endoscopic camera (a medical tool always present in the surgical theatre), the proposed mechanism could be integrated in minimally invasive scenario. Hence, the

integrated system could be used as a dual sensor: to visualise the anatomical area and to evaluate its stiffness, without making use of an additional trocar port. Hence, the proposed sensory mechanism can potentially improve the quality of the diagnosis and enhance the surgeon's understanding of tumour location and surgical margins during a minimally invasive intervention while solving some of the issues that currently preclude more widespread use of minimally invasive procedures.

1.2 Aims and Objectives

The aim of this thesis is to present a novel sensing mechanism which uses vision to determine the stiffness of soft tissue. The creation of the system requires the development of a sensorised device and the implementation of image processing algorithms.

The main objectives are:

1. **to create a disposable mechanism for commercially available cameras capable of measuring the stiffness of soft objects.**
   This innovation can be used in medical applications to define properties of tissue during operations or to find abnormal areas during medical inspection. However, the sensing principle can be used in other applications which involve probing and stiffness measurement.

2. **to implement real-time image processing algorithms that relate the movements of visual features to applied forces.**
   The image processing algorithm should filter the noise while robustly tracking the elastic movements of visual features.

3. **to map the measured stiffness to the anatomical surface.**
   The information acquired through the image processing can be used to compute a real time stiffness map of soft tissue surface.

4. **to make the system versatile and suitable for different medical applications.**
   The visual system can be adapted in several medical inspection procedures, for instance in external diagnosis but also in minimally invasive applications. The system has to be versatile to adapt to specific medical practice requirements.

1.3 Research Contributions

Research into soft tissue characterization provides the field of robotics with a fundamental road-map for developing advanced medical diagnostic tools and systems. Researchers have developed technologies that try to recover the sense of touch by estimating kinesthetic and tactile information. However, most of these methods use costly commercial electronic sensors. Here, the target is to develop low-cost mechanism that can operate in conjunction with available, generic cameras in order to characterize the stiffness of soft objects. The contributions of this thesis are:

1. **A consolidated literature review on different stiffness sensing mechanisms and methodologies for soft tissue characterization in order to determine the research gap and needs is provided;**

2. **The design of a novel sensory system that uses deformable elements and vision to compute forces is accomplished;**

3. **Algorithms for the robust computation of tissue stiffness as a function of relative forces inferred from the deformation of elastic elements under load are created;**

4. **A intuitive user interface for real-time stiffness mapping of soft tissues is designed, implemented and tested.**

1.4 List of the Publications Arising from this Thesis

The contributions of this thesis has led to the following publications:

[1] Angela Faragasso, Joao Bimbo, Yohan Noh, Allen Jiang, Sina Sareh, Hongbin Liu, Thrishantha Nanayakkara, Helge A Wurdemann, and Kaspar Althoefer. Novel uniaxial force sensor based on visual information for minimally invasive surgery. In *Robotics and Automation (ICRA), 2014 IEEE International Conference on*, pages 1405–1410. IEEE, 2014.

[2] Angela Faragasso, Agostino Stilli, Joao Bimbo, Yohan Noh, Hongbin Liu, Thrishantha Nanayakkara, Prokar Dasgupta, HA Wurdemann, and Kaspar Althoefer. Endoscopic add-on stiffness probe for real-time soft surface characterisation in mis. In *Engineering in Medicine and Biology Society (EMBC), 2014 36th Annual International Conference of the IEEE*, pages 6517–6520. IEEE, 2014.

[3] Angela Faragasso, Agostino Stilli, Joao Bimbo, Helge Arne Wurdemann, and Kaspar Althoefer. Multi-axis stiffness sensing device for medical palpation. In *IEEE/RSJ International Conference on Intelligent Robots and Systems*, 2015.

[4] Angela Faragasso, Agostino Stilli, Joao Bimbo, Helge Arne Wurdemann, and Kaspar Althoefer. Towards a novel clip-on sensor for endoscopic cameras using cantilever beam for stiffness computation. In *The 5th Joint Workshop on Computer/Robot Assisted Surger (CRAS)*, 2015.

[5] Angela Faragasso, Agostino Stilli, Joao Bimbo, Helge Arne Wurdemann, and Kaspar Althoefer. Visual-elastic mechanism for real-time soft tissue characterization. In *Robotics Science and System (RSS)*, 2015.

[6] Angela Faragasso, Agostino Stilli, Joao Bimbo, Helge Arne Wurdemann, and Kaspar Althoefer. Hand-held stiffness probe for real-time soft tissue identification using visual features and magnetic tracker. *IEEE Transactions on Robotics (T-RO-Under review)*, 2016.

[7] Allen Jiang, Samson Adejokun, Angela Faragasso, Kaspar Althoefer, Thrishantha Nanayakkara, and Prokar Dasgupta. The granular jamming integrated actuator. In *Advanced Robotics and Intelligent Systems (ARIS), 2014 International Conference on*, pages 12–17. IEEE, 2014.

[8] Jelizaveta Konstantinova, Agostino Stilli, Angela Faragasso, and Kaspar Althoefer. Fingertip proximity sensor with realtime visual-based calibration. In *IEEE/RSJ International Conference on Intelligent Robots and Systems*, 2016.

[9] Min Li, Angela Faragasso, Jelizaveta Konstantinova, Vahid Aminzadeh, Lakmal D Seneviratne, Prokar Dasgupta, and Kaspar Althoefer. A novel tumor localization method using haptic palpation based on soft tissue probing data. In *Robotics and Automation (ICRA), 2014 IEEE International Conference on*, pages 4188–4193. IEEE, 2014.

[10] Yohan Noh, Sina Sareh, Jessica Back, Helge A Wurdemann, Tommaso Ranzani, Emanuele Lindo Secco, Angela Faragasso, Hongbin Liu, and Kaspar Althoefer. A three-axial body force sensor for flexible manipulators. In *Robotics and Automation (ICRA), 2014 IEEE International Conference on*, pages 6388–6393. IEEE, 2014.

[11] Yohan Noh, Emanuele Lindo Secco, Sina Sareh, Helge Wurdemann, Angela Faragasso, Jessica Back, Hongbin Liu, Elizabeth Sklar, and Kaspar Althoefer. A continuum body force sensor designed for flexible surgical robotics devices. In *Engineering in Medicine and Biology Society (EMBC), 2014 36th Annual International Conference of the IEEE*, pages 3711–3714. IEEE, 2014.

[12] Sina Sareh, Allen Jiang, Angela Faragasso, Yohan Noh, Thrishantha Nanayakkara, Prokar Dasgupta, Lakmal D Seneviratne, Helge A Wurdemann, and Kaspar Althoefer. Bio-inspired tactile sensor sleeve for surgical soft manipulators. In *Robotics and Automation (ICRA), 2014 IEEE International Conference on*, pages 1454–1459. IEEE, 2014.

[13] A. Shiva, A. Stilli, Y. Noh, A. Faragasso, I. De Falco, G. Gerboni, M. Cianchetti, A. Menciassi, K. Althoefer, and H. A. Wurdemann. Tendon-based stiffening for a pneumatically actuated soft manipulator. *IEEE Robotics and Automation Letters*, PP(99):1–1, 2016.

[14] Elizabeth I Sklar, Sina Sareh, Emanuele L Secco, Angela Faragasso, and Kaspar Althoefer. A non-linear model for predicting tip position of a pliable robot arm segment using bending sensor data. *Sensors & Transducers*, 199(4):52, 2016.

[15] Helge A Wurdemann, Sina Sareh, Ali Shafti, Yohan Noh, Angela Faragasso, Damith S Chathuranga, Hongbin Liu, Shinichi Hirai, and Kaspar Althoefer. Embedded electro-conductive yarn for shape sensing of soft robotic manipulators. In *Engineering in Medicine and Biology Society (EMBC), 2015 37th Annual International Conference of the IEEE*, pages 8026–8029. IEEE, 2015.

1.5 Thesis Structure

This thesis contains eight chapters which explain the steps taken to achieve the aim presented in chapter 1.2. In line with the objectives, a detailed structure of this thesis is shown in Figure 1.3.

Chapter 1 presents the research motivation of this thesis, the research aim and objectives, the main contributions and the thesis' structure.

Chapter 2 introduces medical diagnostic techniques for tumour localization. The literature on palpation methods is reviewed. Among these methods, instrumented palpation based on force and tactile feedback is further investigated. Additional details on the

stiffness sensing mechanism based on the relative force principle are provided. In general, these systems employ elastic mechanisms used to indent the soft surface which will exhibit several deformations measured by sensory devices.

Chapter 3 presents the sensing principle. The development of a vision-based force sensor demonstrated that uni-axial interaction forces can be accurately estimated as means of visual processing algorithms.

Chapter 4 presents an uni-axial stiffness sensor for endoscopic camera. The estimation of the stiffness is a function of the relative force which is generated by the interaction of several elastic elements with the soft tissue.

Chapter 5 investigates the sensing principle and how it was improved with the addition of multi-directional capabilities. The development of a vision-based stiffness probe for medical palpation of a body part accurately evaluates the stiffness independently of the approaching direction.

Chapter 6 shows the realization of a clip-on sensor for endoscopic camera which uses cantilever beams to generate interaction force. Hence, the endoscopic camera becomes a dual sensor used for visualization but also for stiffness estimation without requiring the integration of additional instruments in the operating room.

Chapter 7 presents the real time stiffness mapping of the examined surface. The algorithm combines the 3D position of the stiffness probe (which is recorded by using a tracking system or robotics kinematics) with the estimated stiffness to create an intuitive representation of the overall soft surface through a colour-coded stiffness map.

Chapter 8 summarises the research findings and the contribution of the thesis to science and medical practice. Finally, future work resulting from the limitations of the proposed sensory mechanism is suggested and discussed.

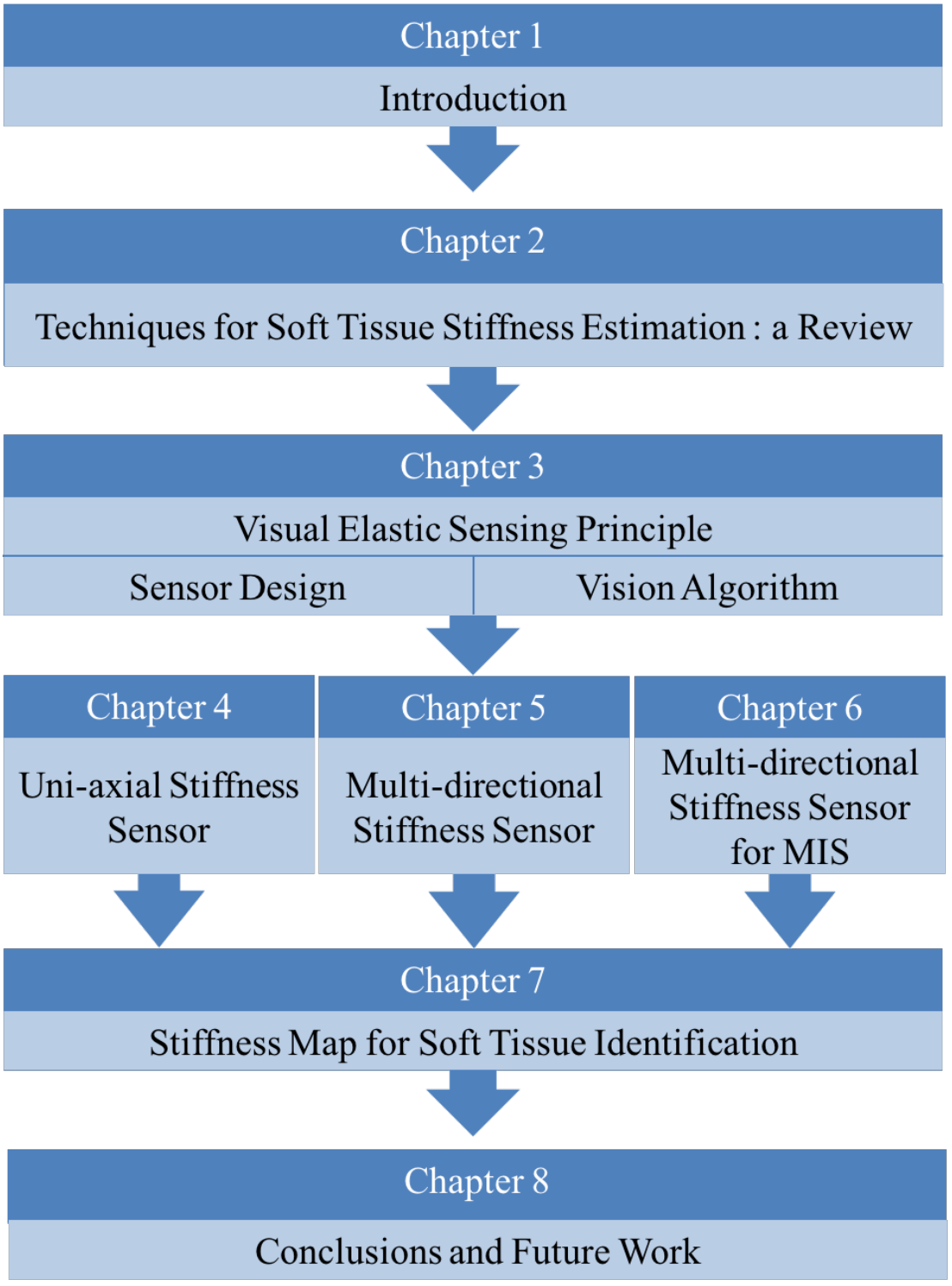

FIGURE 1.3: Thesis Outline

CHAPTER 2

Techniques for Soft Tissue Stiffness Estimation: a Review

This chapter describes the state of the art in stiffness sensing related technologies for medical diagnosis. In order to define a theoretical foundation for exploring diagnostic solutions in medical palpation, the importance of the "sense of touch" in tumour identification is examined. The main tumour identification methodologies, such as manual palpation, medical imaging and instrumented palpation are reviewed. This thesis focuses on instrumented palpation which employs palpation systems which induce deformation onto soft tissues and sensing technologies to measure it . The use of different palpation mechanisms generate different forces, thus, different deformations of the soft tissue. The stiffness of the soft tissue can be measured by means of the relative force.

2.1 Introduction

It has been proved that the mechanical properties of the skin vary for different layers or areas of skin [12, 32]. Age, sex, race as well as skin disorders are parameters that may alter these properties. Tumours that cause structural changes in human tissues also affect these tissues' mechanical properties, for example their elasticity. Physicians describe the size of a cancer, where it is located and how far it has grown, using the TNM (primary Tumour size, lymph Nodes, Metastases) scoring system, a standard developed by the AJCC (American Joint Committee on Cancer). According to this standard T tumours are classified according to their size in four categories: T1 stage tumours are less than 2 *cm*, T2 stage tumours are between 2 and 5 *cm*, T3 stage tumours are more than 5 *cm* but without extraglandular extension, T4 stage tumours are of any size and present the local extension of adjacent structures. The TNM stage describes the site and size/extent of primary tumours. The TNM system is a widely used cancer staging system by means of which cancer reporting is done, for instance a T1, N0, M0 cancer would mean that the primary tumour is less then 2 *cm* across (T1), has not affected any lymph nodes (N0) and has not spread in any other part of the body (M0). Successful medical treatment of cancer depends on timely and correct diagnosis. Early cancer detection, which literally means detection of T1 stage tumours, will in many cases lead to successful cancer treatment or a better prognosis [38]. Experts have proven that there is a link between the mechanical stiffness of the tumour and its invasiveness. Additionally, based on the affected area or organ, T1 tumours are between 3 and 6 times stiffer than the surrounding healthy tissues [39].

Soft tissue stiffness is traditionally evaluated by the subjective method of manual palpation during medical examination [6–8]. During palpation, the physician pushes a finger tip into the tissue with a certain level of force and observes the amount of displacement to gauge the reaction force. Manual palpation is the most commonly used method, although it is not completely reliable because it is subject to human interpretation and not repeatable [40–42]. Moreover, palpation can only be performed in areas accessible to human hands. This thesis proposes a novel sensing mechanism for soft tissue stiffness computation that uses visual information to retrieve the physician's sense of touch. Although, the sensing principle can be adapted and used in different applications, this chapter analyses the requirements of tactile sensing technologies in medical diagnosis. The research conducted in soft tissue characterization and the scientific findings are described and analysed.

2.2 Human Touch Sensing: Inspiration for Robotic Tactile Devices

The human skin acts as a protective barrier between the internal body system and the environment. The skin's ability to perceive touch sensations, that is, its capability to sense the physical properties of surfaces it comes into contact with, communicates to the brain a wealth of information about the outside world. The somatosensory system controls the human sense of touch. This system is involved in the inter-related and conscious perception of position of body parts (proprioception) and movements of the body (kinesthesis). Although some of our most intense sensory experiences originate from the acute sensitivity and intimate contact of touch, all three senses are fundamentally important and the absence of any one can be severely debilitating [43]. Traditionally, the process of exploring a three-dimensional object is believed to be the result of a cross-modal perception [43–47]. In this model, visual and haptic information are combined to obtain the representation of the object [46, 47]. Recently, new scientific findings, have challenged the common belief that the brain areas supporting object recognition are "multisensory". In support of this new theory, Snow et al. [48] have demonstrated that there are areas of the brain that allow humans to recognize and manipulate objects with their hands alone, without engaging the visual sensory system.

In 1987, Lederman and Klatzky [49] created the taxonomy for purposive hand movements that achieve object representation and classified them as exploratory procedures (EPs). The EPs are related to the desired knowledge about the object, as shown in Table 2.1.

TABLE 2.1: Correlation between object's model and EPs [49].

KNOWLEDGE ABOUT THE OBJECT	EXPLORATORY PROCEDURE
Substance-related Properties	
Texture	Lateral Motion
Hardness	Pressure
Temperature	Static contact
Weight	Unsupported Holding
Structure-related Properties	
Weight	Unsupported Holding
Volume	Enclosure, Contour Following
Global shape	Enclosure
Exact shape	Contour following
Functional Properties	
Part Motion	Part Motion Test
Specific Function	Function Test

TABLE 2.2: Robotic Tactile Sensors: Design guideline [50].

PARAMETER	GUIDELINES
Force Direction	Normal and tangential.
Temporal Variation	Dynamic and Static.
Time Response	1 ms.
Force Sensitivity	$0.01 - 10$ N.
Linearity/Hysteresis	Stable, repeatable and monotonic with low hysteresis.
Robustness	Withstand application defined environment.
Tactile cross-talk	Minimal cross-talk.
Shielding	Electronic and/or magnetic shielding.
Spatial Resolution	1 mm fingertips up to 5 mm in palm of hand.
Integration and Fabrication	Simple mechanical integration Minimal wiring Low power consumption and Cost.
Additional Requirements	Temperature tolerance. Size.Weight. Durability. Power Consumption.

In [50] the suggested guidelines for the design of tactile sensors are inspired by the human hand whose fingertips contain a very high density of mechanoreceptors; the authors outline the limitations and alternatives, as shown in the Table 2.2.

Following the biological inspiration used in [50], Yousef et al. [51] proposed the minimum functionality requirements for a robotic tactile sensing system emulating human in-hand manipulation: it should be able to detect contact; to lift, replace and release objects; to detect dynamic and static forces; to track the variation of the contact point during the manipulation and detection of the tangential force to prevent the slip. Multi-purpose sensors that address the requirements outlined in Table 2.2 remain a big challenge. In general, the constrains and limitations of the specific application are identified in the designed sensors in order to reduce the cost and complexity.

During the last decades, tactile sensors based on different sensing principles have been explored and used in many robotics applications, mainly in medical applications. Many classifications and taxonomies exist in the literature, based on:

- the transduction technique (capacitive, piezoresistive, piezoelectric, strain gauge and optoelectric) [52–54];
- the target industry (robotics, biomedical, sport, agriculture, aerospace and automotive industry);

- the sensor dimension (zero, one or two dimensions);
- the location of the sensor (intrinsic and extrinsic tactile sensing) [50];
- the sensing principle (array sensor or force/torque sensor) [51];
- the task to be accomplished (perception for action, action for perception) [50].

Developments in robotics technologies have had a consistent impact on industry, medicine, military, space and ocean exploration, domestic and household environments and hobby pursuits [55]. Medicine and in particular surgical applications have particularly benefited from robotics technologies[56]. Medical robotics has been revolutionising medical care both outside and inside the operating rooms. It is a field in which collaboration between medical practitioners and engineers is essential. The main fields of medicine employing robotics technologies are rehabilitation, surgery, pharmacy automation, disinfection, training, and medical diagnosis. In addition, telepresence robots can be used to remotely perform different medical tasks ranging from examination to surgery [34, 57].

Traditionally, medical diagnosis involved manual palpation, which requires physicians to palpate with their fingers the anatomical surfaces in order to asses the stiffness and size of tumours. Clinicians use distributed tactile feedback to localize lumps and detect abnormalities. Manual palpation is limited to tissues accessible to the physician's hands and highly dependent on the physician's skills. Additionally, manual palpation is completely impracticable in laparoscopic, robot-assisted and and remote procedures. Diagnostic robots (diagnosis tools in the form of physical robot or software expert system) supplement or replace the traditional palpation procedures to improve the outcome of the medical diagnosis.

Given the expected benefits of tactile feedback, many researchers have turned to sensory substitution techniques based on synaesthetic perception, wherein cutaneous perception is presented via an alternative feedback channel, such as vibrotactile, auditory, or visual cues [58, 59]. Although it has been shown that palpation based on electro-mechanical systems equipped with tactile/force sensors is more sensitive than human manual palpation [60], no current sensor is able to measure all the quantities perceived by the human finger. The challenge lies in developing effective systems that deliver realistic cues while fulfilling constraints on size, cost, compatibility, and sterilization [61].

Touch can reveal position, size, shape, texture, friction, force, temperature and other object properties. Gwilliam et al. [62] compared the performance of capacitive tactile sensors in lump detection with the performance of palpation with the human finger, as shown in Figure 2.1. The results showed that tactile sensing technologies can detect lumps at lower indentation depths and pressure than the human fingers.

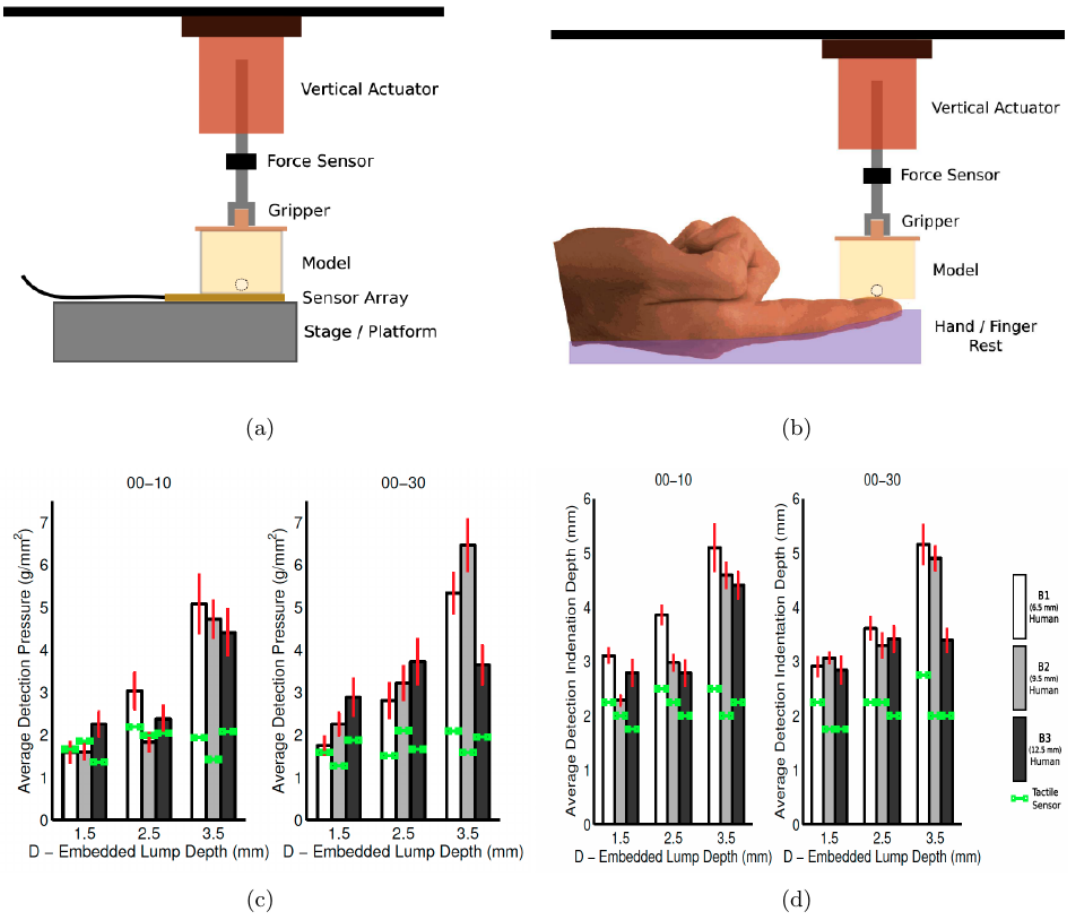

FIGURE 2.1: Human vs. Robotic Tactile Sensing [62]: (a) Human subject test: the hand was fixed under a servo-controlled linear motor indenting the rubber models. (b) Sensor test: the tactile sensor was mounted on a rigid platform, the rubber models are pushed against the sensor by the linear guide. (c) Error bars of the standard error for the required pressure. (d) Error bars of the standard error for the required indentation depth.

This chapter explores tactile sensing technologies developed for medical diagnosis focusing in particular on how indentation devices attempt to mimic the human "sense of touch".

2.3 Methodologies for Soft Tissue Stiffness Measurements

The properties of soft tissues have been widely investigated using compression, shear, tensile, aspiration or indentation methods. A compression test is a mechanical method in which the Young's modulus, that is the stiffness of the material, is estimated by measuring the compressive force and the corresponding deformation of the material. If F is the compression force, A the contact area, w the deformation and h the original

thickness of the material, then the Young's modulus can be expressed as:

$$E = \frac{\frac{F}{A}}{\frac{w}{h}}. \tag{2.1}$$

In equation 2.1, the size of the compressor is assumed to be bigger than the size of the material. If the compression force acts along one axis, the material exhibits lateral extension. The ratio of the axial deformation over the lateral deformation represents Poisson's ratio which expresses the compressibility of the material.
In the shearing test, the force applied is parallel to the material surface and the material deformation is evaluated. For a linear elastic material, the relationship between Young's modulus and the Poisson's ratio is:

$$\mu = \frac{E}{2(1-v)}; \tag{2.2}$$

where μ is the shear modulus, E is the Young's modulus and v the Poisson's ratio.
During tensile stress, pulling force is provided on the material and the tensile modulus, which is the ratio of the tensile stress to the deformation, is measured. If the specimen is pulled until fracture, it is then possible to calculate the tensile strength.
Aspiration which relies on pulling force is another method for computing properties of the material. In this procedure, a cylindrical probe endowed with a camera is applied on the material surface. This creates a negative pressure inside the cylindrical probe for sucking the material under test into the circular probe with unknown radius. The deformation of the material is captured by the camera. Tissue properties can be computed using the negative applied force and the visual information on the material deformation.
Indentation is another approach, similar to compression, and widely used in many applications. In contrast to the compression method, the device used in the indentation method is smaller in size than the material to analyse. In general, the diameter of the soft tissue at stake is at least five times bigger than the indenter's diameter. The main advantage of this technique, when compared with compression methods, is that an *in-vivo* test can be performed non-invasively, as shown in Figure 2.2. Indentation devices that attempt to reproduce the human sense of touch have been developed and used for characterizing the mechanical properties and in particular the stiffness of various soft tissues, such as breast, buttocks, skin, muscles and plantar foot [63]. The typical application of such type of devices is the detection and localization of soft tissue abnormalities.

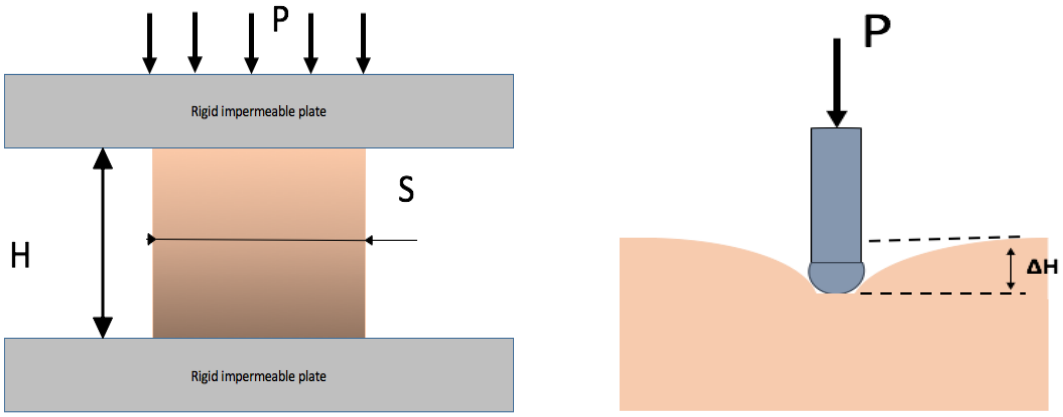

(a) (b)

FIGURE 2.2: Contact Based Approaches for Soft Tissue Characterization: (a) Compression test: the specimen (S) is placed between two plates; a load (P) pushes one plate toward the other decreasing their distance (H) and compressing the material. (b) Indentation device palpating a soft material.

2.4 Limitations of Minimally Invasive Interventions

Surgical procedures fall in three main categories: invasive procedures, also know as open surgeries, minimally invasive procedures, and non invasive procedures. While in non-invasive and open procedures manual palpation is limited to tissues accessible to the clinician's hands and highly dependent on the clinician's skills, more challenges arise in minimally invasive procedures in which manual palpation is completely impracticable.

Minimally Invasive Surgery (MIS), also known as keyhole surgery or laparoscopic surgery, is one of the most effective methods of modern surgical intervention. MIS involves procedures performed by entering the human body using instruments that are inserted via 12-15 mm incisions (trocar ports) or natural orifices using surgical tools and endoscopic cameras. Laparoscopy is a form of MIS that is performed in the abdominal area. Its inception has revolutionised the surgical care significantly reducing postoperative pain, recovery time and hospital stay with marked improvements in cosmetic outcome and overall cost-effectiveness [14]. Since the early 1990s, surgeons have been pushing the limits of MIS by attempting the most complicated procedures known in surgery. During the last 10 years, minimally invasive surgery has influenced the techniques used in every speciality of surgical medicine. MIS has being applied not only in relatively routine operations such as prostatectomy [15], cholecystectomy [64], and gynaecology [65] but also in challenging procedures which are very difficult to conduct laparoscopically such as coronary artery revascularization and mitral valve repair [23] [13].

(a) (b)

FIGURE 2.3: Surgical Theatre for: (a) Conventional Endoscopic Surgery (CES) in which the surgeon manipulates the surgical instruments using his hands and (b) Robotic-assisted Minimally Invasive Surgery (RMIS) in which the surgeon operates remotely moving the robots from a console.

Among the various applications of MIS, a distinction can be made between conventional endoscopy surgery (CES) and Robotic assisted Minimally Invasive Surgery (RMIS). In CES the surgeon operates directly on the patient by using an endoscopic interface, whereas for RMIS a computer-instrumented interface (surgical robot) is positioned between the surgeon and the patient. The setup of the surgical theatre for both is shown in Figure 2.3. A potentially major drawback of RMIS is the absence of haptic feedback. In CES, force feedback is experienced by the surgeon through the laparoscopic instrument handles; force feedback is a product of the interaction of the laparoscopic instruments' tips with the tissue. In RMIS, the operation is performed by robotic arms, teleoperated through a console on which the surgeon executes his gestures [66]. No force feedback resulting from the interactions with the patient's tissue is provided.

Robot-assisted surgery is enhancing the ability of surgeons to perform minimally invasive procedures by scaling down motion and adding additional degrees of freedom to the instruments' tips. The number of surgery robots is growing rapidly. The most famous surgical robotic systems are the Da Vinci surgical System produced by Intuitive Surgical, the ZEUS robotic surgical system and the Automated Endoscopic System for Optimal Positioning (AESOP). These advanced robotic systems give doctors greater control and vision during surgery. In a typical robotic assisted surgery, surgeons operate from a console equipped with two master controllers that manoeuvre four robotic arms. The 3-D images of the operating site are shown to the surgeons on the console, as shown in Figure 2.3(b). Computer software takes the place of actual hand movements and can perform operations with high precision. Although rapidly developing, robotic surgical technology has not achieved its full potential owing to a number of limitations. In the current robot-assisted surgical system market which is heavily dominated by Intuitive Surgical, the main disadvantages of commercially-available robotic surgical systems are

(1) the purchase costs and (2) system maintenance. Other high costs are incurred for operative consumables per case, which often overshadow savings gained by shorter hospital stays. Other drawbacks to robotic surgery include the bulkiness of the robotic equipment currently in use and the lack of tactile and force feedback to the surgeon [67].

During open and non-invasive procedures, surgeons have direct access to affected organs and body parts. This allows clinicians to identify tumours and boundaries through manual palpation to ensure the removal of tumours with low positive and negative margins. Surgeons investigate manually the force-displacement response to acquire distributed tactile information. Tissue areas that are stiffer than the surrounding areas can be recognized as potentially abnormal [16]. Although vision has been improved in MIS through the introduction of high-definition systems, methods feeding back the sense of touch, kinaesthetic and tactile sensation are still in their infancy. The force applied to soft organs can only be estimated through visual feedback by observing the deformation of the tissue in the transmitted camera images, as depicted in Figure 2.3. The lack of direct palpation during MIS may lead to insufficient feedback and thus hamper identification of tumours. The importance of force feedback has been experimentally evaluated in [68] for a blunt dissection, a surgical manipulation task frequently employed in minimally invasive surgery. Although the force feedback is widely assumed to enhance the performance in robotic surgery, its implementation cost is prohibitive, due to the stringent design requirements imposed by the surgical environment. It is reported that the absence of physical tissue interaction is one of the most important limitations of MIS compared to traditional procedures [19].

In telerobotic systems, the surgeon operates from a console, which can be thousands of miles away from the slave robotic arm situated near the patient; the surgeon's commands are relayed to the slave manipulator through the telecommunication infrastructure. Using such a tele-operated approach to surgery, it is very difficult to preserve perceptual transparency, which quantifies human perception of the remote environment. A perfect teleoperation system must be perceptually transparent, meaning that the interface appears to be nearly nonexistent to the operator, allowing him or her to focus solely on the task environment, rather than on the teleoperation system itself. Furthermore, the ideal teleoperation system must give the operator a high sense of presence, meaning that the operator feels as though he or she is physically immersed in the remote task environment [69]. For this purpose, the human operator is coupled with the telerobotic system with all necessary senses: visual, auditory and haptic modalities. The first telerobotic surgery was performed by Professor Jacques Marescaux at the IRCAD/Hôpital Civil, Strasbourg, France on 7th September 2001 using the Zeus TS Surgical System. A dedicated asynchronous transfer mode (ATM) network was used to connect the surgical console of the Zeus TS system situated in New York City to three robotic arms at IRCAD/Hôpital

Civil, the site where the laparoscopic cholecystectomy was performed. The reported latency for this procedure was 155 ms. At this latency, Professor Marescaux reported no significant impact on his ability to perform fine surgical movements and successfully complete the procedure in 54 min [70]. Since then, many telerobotic operations have been performed. However, tele-surgery over longer distances is not yet feasible. Unpredictable time-delays, although brief, pose a major challenge and can lead to mechanical instabilities for such remote teleoperation that can disrupt procedures and injure patients [67]. A promising alternative is telementoring, which permits an expert surgeon, who remains in his/her own hospital, to guide another surgeon in a remote location; both surgeons "share" the view of the surgical field and control of the robotic system and communicate via an audio system. Telemonitoring —- TELEMENTORING??— can provides a superior degree of collaboration between surgeons in teaching hospitals and rural hospitals [71, 72].

In RMIS, transparency implies not only the matching between the position of the master and the slave but also between the indentation force applied at the tool tip and the feedback perceived remotely by the clinicians. At the current stage, the force feedback is not present in telerobotic systems. Thus, visual force feedback is considered as the only option. However, analysis performed in [66, 68] shows the minimization of palpation task error when direct force feedback is used.
While telepresence surgery holds much potential for fulfilling many of today's remote surgery requirements, it also brings with it a set of new challenges. First, the cost of equipment and communication links is high. Training surgeons with the technology and setting the equipment is time consuming. Second, it is essential that an adequately trained surgical team is present at the surgical site, ready for emergency intervention in case the equipment malfunctions, or the communications line is severed. With the possibility of telemedicine and robotics new legal and ethical issues arise. Questions about responsibilities and potential liabilities of healthcare professionals, duty to maintain confidentiality and privacy of patients' records, jurisdictional problems associated with cross-border consultations, must be answered before remote surgery can be widely adopted [73].

2.5 Instruments and Technologies for Tumour Identification in Medical Diagnosis

Although palpation has been successfully employed for centuries to assess soft tissue quality, it is a subjective test, and is therefore qualitative and depends on the experience of the practitioner. Medical Imaging is one of the main pillars of comprehensive cancer

care, has many advantages including real time monitoring, provides accessibility without tissue destruction, is minimally or non-invasive and can function over wide ranges of time and size scales with regards to biological and pathological processes. However, imaging modalities suffer from deficiencies in sensitivity and/or resolution that preclude their ability to solve important clinical problems in cancer screening, staging, and treatment [74]. Therefore, researchers have been developing diagnostic instruments for different medical specialities in order to analyse stiffness distribution on the skin or internal body parts. For this purpose, different sensing mechanisms have been exploited. A general distinction can be made between sensors measuring force and those measuring tactile properties of the anatomical surface.

Haptic or kinaesthetic devices are used to relay the sense of touch to the user through the transmission of forces, vibration or motion. These technologies are used in telerobotics and computer simulations to virtually reproduce the behaviour of the interaction with the environment back to the user. The incorporation of sensors on the remote side allows the evaluation of the forces exerted by the user. For instance, in haptic teleoperation, robotics tools are remotely controlled by the operator using the haptic interface, while force feedback is employed to characterise the interaction between the external environment and the tools. Thus, the operator receives "virtual" sensations which guide him or her to generate forces on to the environment.

This survey analyses the sensing technologies for tumour localization in medical diagnosis. Among these technologies, instrumented palpation is analysed in detail and classified in accordance to the sensing technique used to evaluate soft tissue properties, i.e., sensors based on electromechanical, piezoelectric, piezoresistive, vision/optics based methods. Additionally, palpation instruments where stiffness is determined based on the difference of measured forces are reviewed.

2.5.1 Palpation Instruments based on Force Feedback

Force feedback is a widespread method used in medical diagnosis to sense the mechanical properties of soft tissues and identify specific features that are difficult to access visually. Additionally, direct force feedback can prevent the exertion of inadequate forces which could damage tissues and soft organs.

Commercial force sensors, such as the Nano-17 (ATI, Industrial Automation), a sterilisable commercial 6 DOF force/torque sensor with a diameter of 17 mm, are frequently utilized to estimate force feedback in indentation and MIS-related research studies [35, 75] as they provide a good accuracy and sensitivity. Indentation is the most used technique for developing sensing devices in medical applications. Indentation sensors have been

manufactured using different transduction principles, such as strain gauges, Fibre Bragg Grating (FBG), fibre optics or induction.

Piezoelectric and strain gauge sensors

Piezoelectric transducers have been used to create many force and tactile sensors for medical applications [76–78]. For instance, Yegingil et al. [76] developed cantilever piezoelectric fingers (PEF) to compute both tissue elastic modulus and tissue shear modulus in breast tumour characterization. A dual piezoelectric layer design is used to apply force and detect the indentation depth electrically. The ratio between the shear modulus and the elastic modulus, G/E, is used to model tumour inter-facial roughness the measure of which is employed to differentiate between invasive malignant and non-invasive breast cancers. Experimental results show that the PEF can determine the invasiveness, malignancy, and size of the tumour with high accuracy. The investigation of 1D anisotropic corrugated inclusions and 3D isotropic spiky-ball inclusions showed that for smooth inclusions G/E is the same in both tissue models regardless of the shear direction; for rough inclusions the G/E increases following the increase of the angle between the shear direction and the corrugation in the 1D model, while it depends on the degree of roughness in the 3D model.

For *in vivo* estimation Arokoski et al. [79] developed a hand-held computerised soft tissue stiffness meter (STSM) which uses two force transducers. The device is composed of a measurement rod joined to a handle. The rod embeds a cylindrical indenter that is pressed against the soft tissue with a certain amount of force. Thus, a constant deformation is applied on the material . The force applied to the indenter by the tissues is used to evaluate the tissues stiffness. The STSM has an adjustable diameter (between $0-20mm$) and a length of $100mm$. The exploded and assembled views of the sensor are shown in Figure 2.4(c). Two force transducers, fixed in the handle-hand device, evaluate the compressing and the indenter force signals which feedback to a computer in real-time. The STSM has been used to evaluate the stiffness of different parts of the human body (neck, shoulder and forearm areas) in *in vivo* tests. The experimental results show that the device is capable of distinguishing between muscles and soft tissue tones with a high rate of reproducibility in the measurements. However, further investigations will be required to determine the reliability of STSM in different patients and its usefulness in monitoring of different soft tissue treatment schedules and medication [32].

Significant advances towards incorporating force feedback into laparoscopic tools have been made in the last decade [68, 80–82]. Commercially available force sensors, such as strain gauges, have been used to record the forces at the tool tip through indirect methods. Researchers have also designed new laparoscopic tools or systems which incorporate

sensing technologies in the design. For instance, [83] developed an automated laparoscopic grasper that can compute grasping as well as lateral and longitudinal forces. The mechanism has low friction and its modular design allows interchangeability between various effectors (cutter, grasper, dissector). Experimental results show the capability of this novel device to measure probing forces and characterize artificial tissue samples. Tool force-feedback has also been incorporated in the MiroSurge, a robotic master-slave teleoperated system developed by DLR [84]. The haptic master interface can reflect forces in all directions. The MiroSurge scenario includes a master console with a 3D-display and two haptic devices as well as a teleoperator consisting of three MIRO robot arms. Usually two MIROs carry surgical instruments (MICA) equipped with miniaturised force/torque sensors to capture reaction forces on the manipulated tissue, as shown in Figure 2.4(b), while the third MIRO is used for carrying the camera. The incorporation of force feedback in the system allows the surgeon to feel the contact with the anatomical areas under examination.

Force feedback can be achieved by using strain gauges and piezoelectric transducers that are relatively cheap, thus disposable. However, these force sensors cannot be integrated in the medical setup as they are not MRI compatible and are very sensitive to temperature.

Optical Sensors

Noh et al. [85, 86] proposed a 3-axis force/torque force sensor for a flexible manipulator made of acrylonitrile butadiene styrene (ABS) and based on light intensity modulation. The multi-axis sensor uses fibre optics to compute the tissue interaction forces. Force and Moments arranged at a specific angle to each other are computed using a pair of optical fibres, one emitting the light and the other receiving it. Additionally, the proposed force sensor employs mirrors as reflective surfaces and a flexible ring-like structure. When a force acts on the upper plate of the sensor, three cantilever beams bend changing the reflected light as shown in Figure 2.4(a). A multiple linear regression method is used to compute the force along the z-axis, F_z and the moments M_x and M_y. The sensor can compute forces up to 6 N along the z axis with 2.1% of error, and moments in a range of +/- 3.5 Ncm and +/- 2.5 Ncm with errors of 14.2% and 3.0 % along the x and y axis respectively. Although the sensor is MRI compatible and presents high sensitivity, problems in the calibration, hysteresis, error, crosstalk, influence of the temperature, non linearity and repeatability should be solved. Moreover, the sensor's diameter of 30 mm doesn't fit in a standard trocar port, thus problems arising from miniaturization should be explored.

In [87], elastomer elements were used to develop an MRI compatible uniaxial force sensor for mitral valve annuloplasty utilised within a beating heart. The sensor uses a pair of optical fibres to sense forces in a range of $0 - 4\,\mathrm{N}$ with less than 3 % of error. The

sensor's size is 5.5 mm in diameter and 12 mm in length, it is waterproof and electrically passive. However, it can only compute the force along one axis, thus bending of the fibres may degrade the sensor's sensitivity. In addition, it is affected by temperature and it is subject to hysteresis.

In order to have multi-axial capabilities, researchers have been exploring rolling indentation mechanisms which enable the scanning and computation of forces on a surface rather than at a single point. For instance Liu et al. [33, 88] proposed a rolling indentation device that can slide on the soft tissues and compute the reaction force as well as identify tissue stiffness distribution. Optical fibres are employed to sense both axial force and indentation depth and are used to estimate the stiffness distribution of the soft surface. Light modulation is also the principle used in the distal force sensor realized

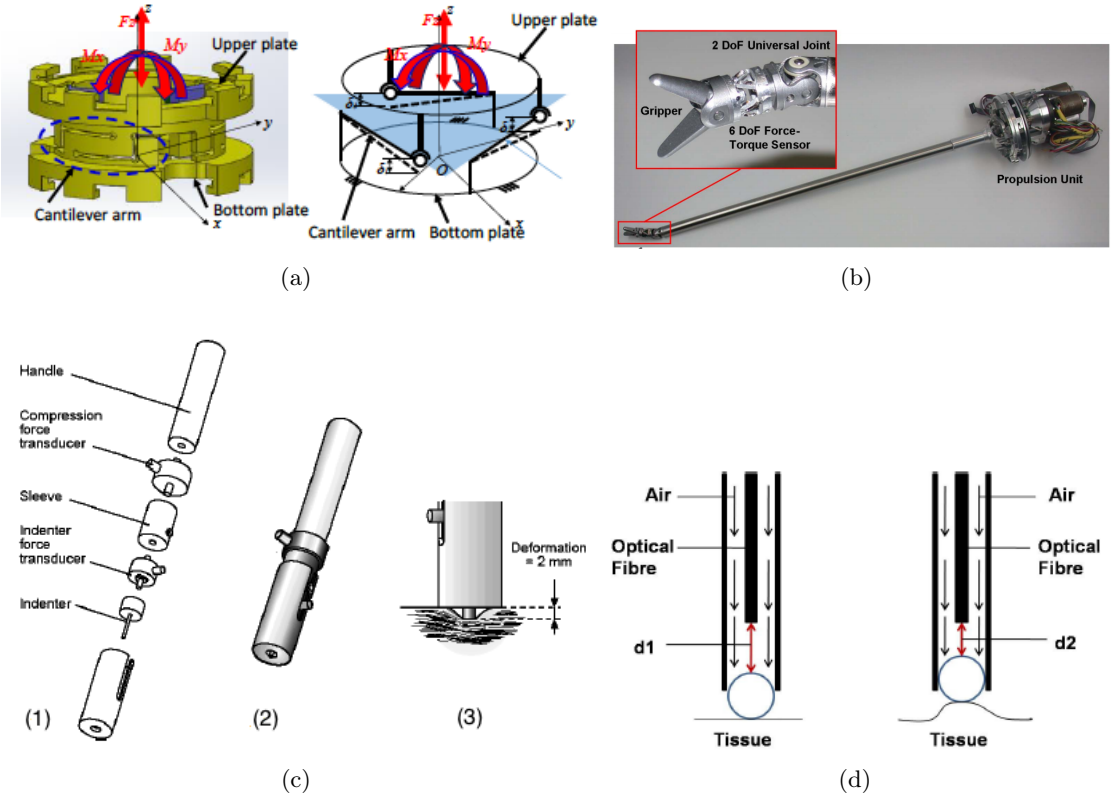

FIGURE 2.4: Palpation devices based on force feedback: (a) The design of the 3-axis force/torque sensor developed in [86]. (b) The MICA instrument for minimally invasive surgery; it is composed of an intra corporal universal joint with 2 DOF, a functional tip and one force/torque sensor connected to the input device which is remotely manipulated by the surgeon in the master console. (c) Stiffness meters by Aroskoski et al. [79]: (1) The sensing principle (2) Exploded view (3) Assembled view (d) Optical-based air-cushion sensor for MIS by Zbyszewski et al. [89].

in [90]. The sensor can measure forces in a range of 3 N in axial and 1.5 N in radial direction with less than 5 % of error. Given a constant indentation depth, the tissue stiffness can be calculated.

A rolling mechanism and a pair of fibre optics are the components of the sensing principle used in the air-cushion mechanism developed in [89]. This sensor allows the mechanical characterization of soft tissues without any constraints on the sensor's movements. The optical fibres are positioned in the sensor's structure to a predefined distance from the roller which slides over the tissue and indents it by air flow. The variation in stiffness of the examined surface causes the sliding of the roller towards and away from the fibres, as shown in Figure 2.4(d). Knowing the initial sphere-fibre distance, the stiffness of the tissues can be estimated by means of light variation. However, a mathematical formulation between the air and the behaviour of the sensor is needed to improve the sensor's performance.

Optical sensors are sensitive to the light changing and bending of the fibres. Besides, their use requires a laborious calibration process and in some cases pre-registration of the soft surface. Thus, these technologies are noisy and cannot be used in real medical applications.

2.5.2 Palpation Instruments based on Tactile Feedback

Tactile sensing technologies are fundamental in robotics, biomedical instruments and industrial applications. A tactile sensor can be defined as a device that can measure a given property of an object or a contact event between sensor and object [91]. In MIS, tactile feedback can be used to evaluate tissue properties in a whole region rather than at a specific point as is the case with force feedback. Figure 2.5 shows a haptic user interface for medical training. The haptic information is computed using the Geomagic Touch Haptic Device (formerly Phantom Omni), one of the most used haptic devices, that provides 3-DOF navigating parameters and force feedback in case of collision detection. A standard simulator is used to visualize augmented images in the screen [92]. The adaptive control for the master robot can be implemented to support manipulation tasks during the operation. A tactile sensing system to be used in MIS should be composed

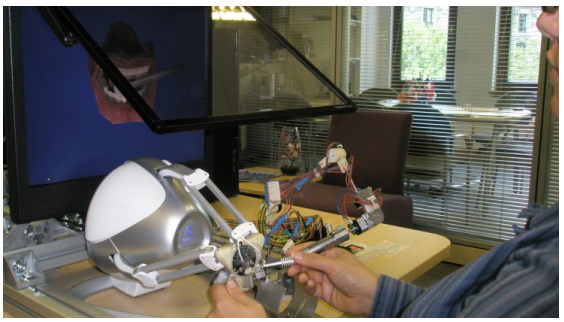

FIGURE 2.5: Haptic user interface: Geomagic Touch Haptic Device and Virtual Reality Simulator.

by a tactile sensor which extracts the tactile data acquired through contact, a tactile data processing which filters data keeping only relevant information,and a tactile display that presents the information to the surgeon. The tactile sensor comprises of sensing, electronics, protective and support layers [93, 94]. The sensing layer can be a single element or an array of elements. In MIS two types of tactile sensors are used, namely elastomer-based tactile sensors and silicone tactile sensors. They differ in that in the former the sensing layer is made of carbon or silver-impregnated rubber while the latter is made out of silicone. Determining the pressure spatial distribution enables surgeons to retrieve information of the internal structure [95].

Trejos et al. [29] reviewed the current state of the art in sensing technologies for surgical applications in order to underline the current limitations and evaluate the benefits of haptic information. Starting from the early 1990s, several devices have been developed and explored in order to enhance the outcome of physical examinations and objectively quantify soft tissue properties. Many haptic systems have been used either in medical training or to improve the functionality of medical tools in minimally invasive surgery.

Frei et al. in [96] realized a device able to measure viscoelastic properties of human tissue, particularly, when applied to breast examination. Small piezoelectric elements in the form of spaced fingers are arranged in a suitable array and can be fixed in a glove. Thus, the user can press the finger into the soft tissue applying about the same pressure to each element which will develop an output related to the consistency of the tissue beneath the individual transducer element. A difference in the output produced by any one of the transducers can identify a border or a thickened tissue region, thus a potential tumour. Although this instrument can compute the thickness of a very small tissue region by evaluating differences in the output of the adjacent transducers, the measured soft tissue's proprieties are influenced by temperature.

A Tactile Tumour Detector (TTD) for breast examination is presented in [9]. Numerical analysis is used to derive and simulate a simplified model of physician examination behaviour. A tactile probe has been used to evaluate the accuracy of the derived mode experimentally. The tactile sensing instrument is composed by a tactile probe employing a force sensor resistor (FSR), an electrical circuit, a data processor and a tactile display. This device is able to detect abnormal objects embedded in soft tissue and presents high sensitivity when compared with clinical manual breast examination and self examination. However, the derived model assumes that the thickness of the tissue, the distance between the sensor's centre and the tissue's centre, and the depth and shape of the mass are known. Thus, this mechanism works only with specific simulated models and cannot be used in real applications. A schematic representation of the device is shown in 2.6(b).

A combination of piezoelectric transducer (PZT) and a pressure sensor element was used to develop the tactile sensor in [97]. Upon contact with a test object, this system responds to its physical properties by changing its resonance frequency in accordance with the object's acoustic impedance. This device is able to sense the difference in degrees of hardness and/or softness of different objects but the PZT transducer used is 5 mm in diameter and 1 mm in thickness and thus is not suitable for MIS.

A micro version of this probe was presented by [98]. The Micro-Tactile-Sensor (MTS) is able to measure elasticity with high sensitivity and detect the instant of the contact using the contact compliance and phase shift methods. The probe is shown in Figure 2.6(c). Basically, the shift of the piezoelectric sensor between loaded and non-loaded condition was used to retrieve information about the loaded object. A Finite Element Analysis (FEA) was performed to determine the vibration modes. A tactile mapping method was employed to obtain a contour image and Young's modulus map of the sample surface. Although tactile-resonance-frequency-based sensors can measure both elastic and viscous properties of soft tissue, issues in repeatability and reliability make them impractical.

An endoscopic grasper with miniaturized PVDF-sensing elements, as shown in Figure 2.6(a), was developed in [99]. The system comes with a graphical interface but its functionality is limited by the dimension of the grasper, which can cover only a small area. Thus, this sensor can not be used to recover stiffness information of big organs. The design of a passive tactile sensor, capable of tissue elasticity measurements and able to detect contact force and pressure distribution, was developed in [100]. The sensor has a compliant structure which is the result of the combination of sensing elements with different stiffness values. This sensor can compute elasticity with a resolution of 0.1 MPA for elasticity measurement and 5 mN for the force. The microstrain gauges used present high force sensitivity, high dynamic range, good linearity, and high signal-to-noise ratio. However, they require precise handling in the positioning process and the measurement should be performed under a microscope and with great care.

Despite the increasing research interest in tactile sensing technologies for MIS, the use of these sensors in evolved systems has been minimal. Although most of the proposed solutions can characterize soft tissue properties with high accuracy, they have been confronted with many issues, e.g. biocompatibility, miniaturization, robustness, acceptance from the medical community and surgeons, cost, ergonomics and integration. Furthermore, the associated regulation and standard make their commercialization challenging.

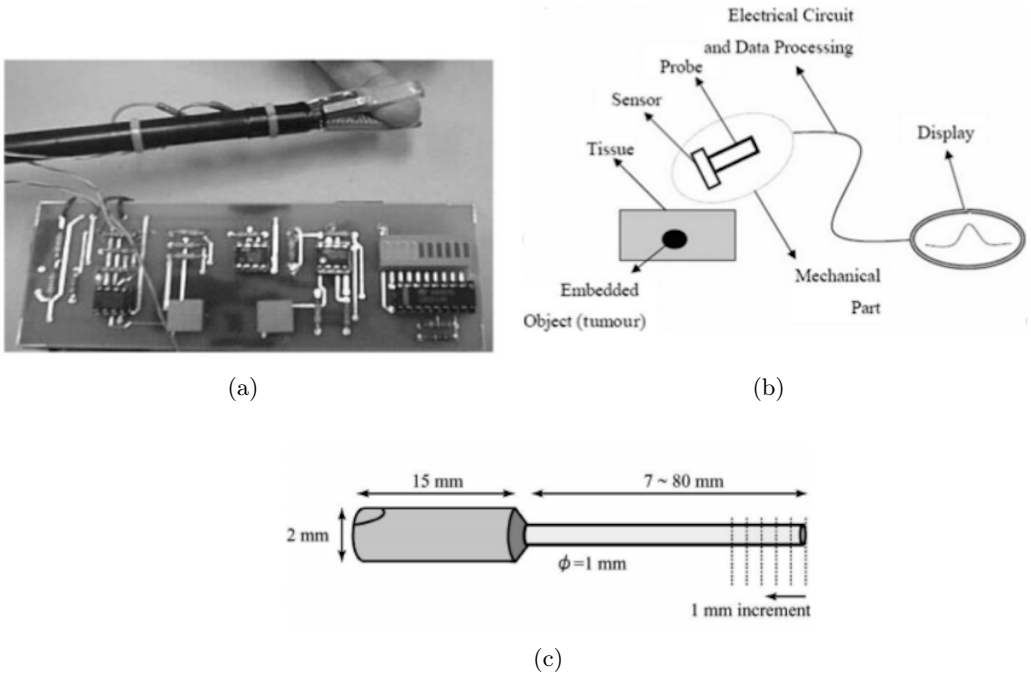

(a) (b)

(c)

FIGURE 2.6: Palpation devices based on Tactile feedback: (a) The endoscopic grasper developed in [99] (b) Schematic representation of the tactile tumour detector [9] (c) The Micro-Tactile-Sensor (MTS) by Murayama et al. [98].

2.5.3 Diagnostic Imaging Techniques

Mechanical Imaging (MI), also known as diagnostic imaging, is a new modality of medical diagnostics based on visualizing the internal soft tissue structures in terms of their elasticity modulus. During the last decade, MI technology has been used in various medical applications, such as the visualization and evaluation of prostate conditions, breast cancer screening, the differentiation of benign and malignant lesions, and the characterization of vaginal wall elasticity. MI is simple, fast, inexpensive and safe. Different approaches have been proposed to estimate and image *in vivo* the elastic properties of the tissues. Most of these techniques try to evaluate the tissues' response to stimuli [47] [101]. Heat, water jets, vibration share waves and compression are the stimuli evaluated so far. They produce different types of information and images, but their response falls into a common spectrum of elastic behaviour [102]. In addition, MI methods are influenced by boundary conditions between different tissues and tissues' elasticity distribution [60]. Nowadays, there are six imaging techniques available to medical experts for diagnosis, staging and treatment of human cancers [74]:

1. Computer Tomography (CT), which uses X-rays to make cross-sectional pictures of the body.

2. Magnetic Resonance Imaging (MRI), which involves radio waves and strong magnetic fields to picture organs and tissues.

3. Position Emission Tomography (PET), an expensive nuclear imaging technique, which uses radioactive tracer material and detection of gamma rays. This technique allows the creation of computerized images of chemical changes, e.g. sugar metabolism.

4. Single-Photon Emission Computed Tomography SPECT, is similar to PET but presents lower resolutions and is less expensive.

5. Optical Imaging, which uses reflection and absorption of photon, thus not-ionizing radiation, to retrieve molecular and cellular information of the living body.

6. Ultrasound (US) in which high frequency sounds waves are used to create images of the inside the body.

Among these, only the first four can produce three-dimensional representations. These imaging techniques are used in pre-operative registration; intra-operative use is challenging and troublesome because it is prone to registration errors due the movement of organs and deformation of soft tissues that occur during surgery.

Recently, with the advances in image processing and graphical systems, analysis of intra-operative images has been improved and used to compute tissue properties. Elastography, or Elasticity Imaging (EI), is an emerging medical imaging technique which maps the soft tissue strain induced by applying stress [103]. Elasticity measurements involve the application of a force or stress which can be performed using compression devices, external vibrators or acoustic and radiation force, and the measurement of the mechanical response through magnetic resonance, ultrasound, optical or acoustic signals [104]. Elastography allows clinicians to visualize mechanical properties of the soft tissues, i.e. stiffness, and detect even small and deep seated lumps [105]. Elastography is often used for tumour localization in medical palpation, as stiffer and thus potentially abnormal tissue experiences low strains. Real-time ultrasound elastography has been used to evaluate tissue properties and identify tumours in many diagnostic procedures [103]. However, the interpretation of the output images is a limiting factor as shown in Figure 2.7.

Although elastography imaging techniques, such as magnetic resonance elastography (MRE) and ultrasound elastography (USE), provide accurate multidimensional images, they cannot always be used intra-operatively. In relation to the spatial resolution used, the reconstructed image can be effected by a significant level of noise. Techniques used to filter and smooth the images are complex and computationally expensive. The combination of haptic and imaging seems to be promising, but it comes with severe limitations.

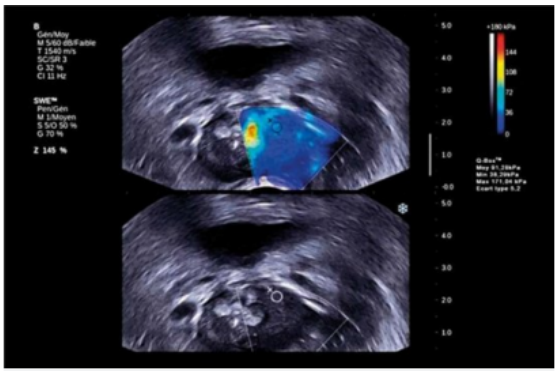

FIGURE 2.7: Ultrasound vs Elastography of papillary thyroid carcinoma: The supersonic shear imaging (top) maps the malignant cancer, which is much stiffer than the healthy tissue, in red. The results of the conventional ultrasonography (bottom). The image obtained with the Shear Wave Elastography provides a more reliable distinction between benign and malignant nodules [106].

Issues related to in situ 3D reconstruction, biomechanical modeling under large scale tissue deformation, recreation of tactile sensing and feedback, and instrument dexterity are some of the major obstacles to be tackled [104, 107].

2.6 Stiffness Sensing Palpation Instruments based on Relative Force

The stiffness of a pure elastic material can be computed by applying on its surface two different forces, F_1 and F_2, which will produce two different deformations, x_h and x_s. The material's stiffness is the ratio between the relative force $(F_1 - F_2)$ and the relative deformation of the material$(\Delta x_h - \Delta x_s)$ [100]. Figure 2.8 gives a schematic representation of this concept. Following this principle, researchers have been developing medical sensors which employ elastic elements that present different degrees of stiffness. When interacting with external surfaces the elastic elements generate different forces which are used to estimate the material's properties.

In [99] authors developed a sensor that can determine the stiffness of a relatively large object during palpation procedures. The sensing mechanism consists of two coaxial cylinders of polyvinylidene films (PVDF) presenting various moduli of elasticity. Exploded and assembled view of the sensor are shown in Figure 2.9(a). During contact it is not required to know any information about the displacement of the sensor's components. However, the functionality of this system is limited by the dimension of the grasper that can cover only a small area. In addition, the proposed sensory system needs the application of a load driven by a vibrating unit. Furthermore, the miniaturization of PDVF and the embedded rubber cylinder is extremely challenging. The major limitation of the

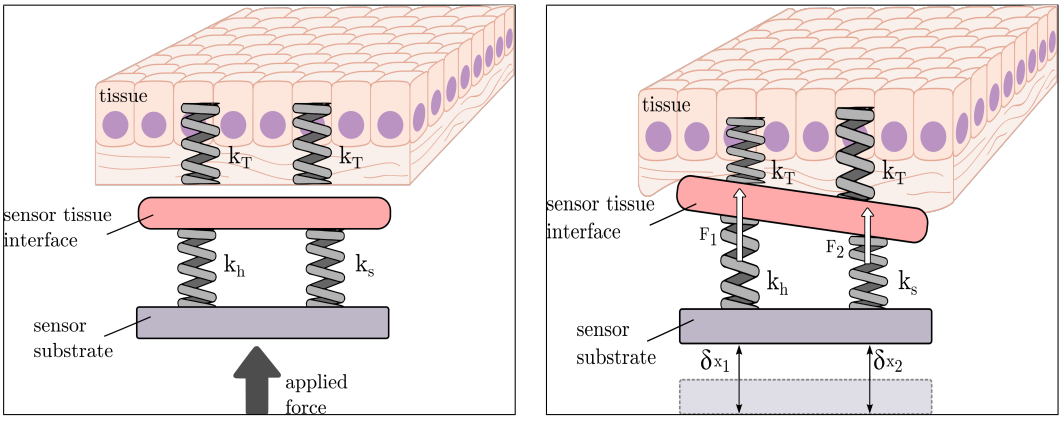

FIGURE 2.8: Principle of Stiffness Sensing based on Relative Force: (a) Two elastic elements presenting different and known elastic constant, k_h and k_s, are embedded in the sensor. (b) The contact with a tissue will generate two different forces, i.e. the still elastic element, k_h, will move less than the softer k_s. The relative displacement of the sensing elements can be used to compute the stiffness [100].

sensor is its perception of the small elasticity range of the rubber cylinder which influences the range of the Young's moduli. The same sensing principle has been used in [100] by employing an array of Microelectromechanical (MEMS) capacitive sensor membranes presenting different elasticity in order to estimate the stiffness of a probed soft tissue, as shown in Figure 2.9(b). Preliminary tests on polymers with different compliances confirm the ability of the proposed sensor to evaluate forces and stiffness, but only in a very small range.

A micro-machined piezoresistive tactile sensor for compliance detection has been presented in [93]. The sensor has a zigzag structure which acts as a spring, with MESAs (Miniature Electrostatic Accelerometers) at the tip, as shown in Figure 2.9(c). The elasticity of the piezoelectric elements is considerably different and the choose depends on the mechanical properties of the soft tissue to be analysed. A finite element model is developed to investigate the sensor performance with the designed parameters using two types of element ends with a cubic and spherical shape. The derived mathematical model considers the cross-talk effect, i.e. the effect the tissue between the two points the springs are in contact with has on the force generated on each spring. Although the preliminary results obtained in simulations are promising, the range of forces that the sensor can evaluate is extremely small. Additionally, the integration and miniaturization of the electrical circuit is very challenging.

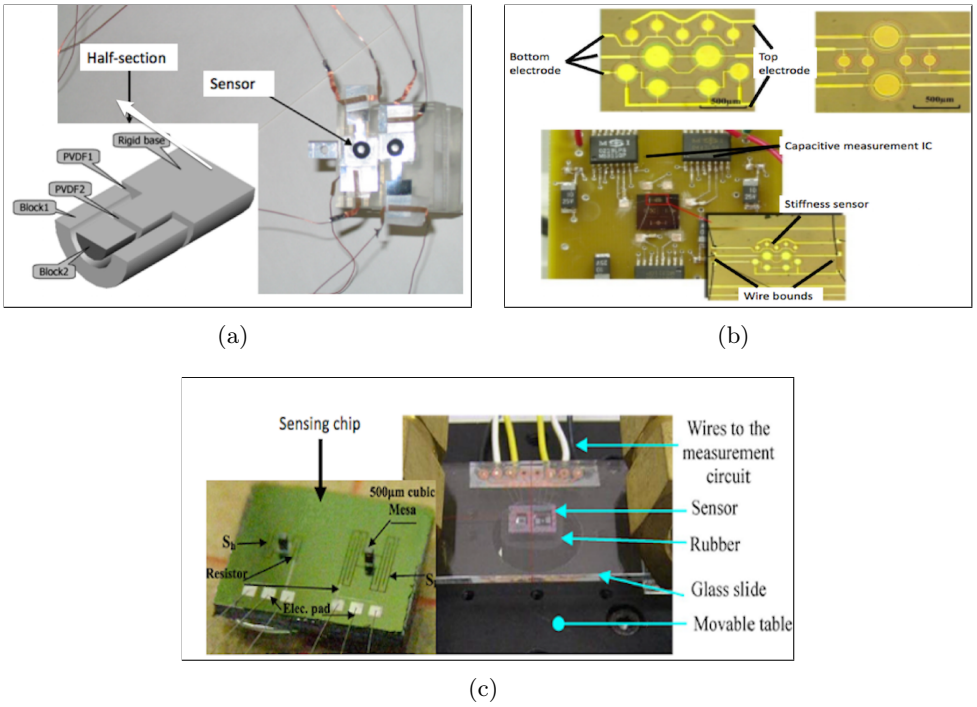

(a) (b)

(c)

FIGURE 2.9: Sensors using Relative Force principle: (a) The sensor proposed in [99] is composed by two coaxial cylinders made of polyvinylidene film which have different moduli of elasticity. (b) The MEMS sensor developed in [100]. (d) The micro-machined piezoresistive tactile sensor proposed in [93].

2.7 Vision-based Palpation Instruments for Medical Diagnosis

Up to now most of the research efforts in tactile sensing technologies for soft tissue characterization have used electrical components and/or technologies that are expensive and not ergonomic. Thus, problems related to sterilization and integration with the medical setting prevent them from being used in real applications. Regarding these limitations, some researchers exploited indirect methods for measuring deformation of the soft tissue subject to a force by means of image processing algorithms. Usually, vision-based methods employ a camera sensor to capture the deformations of the soft tissues, and a contact or non-contact approach for generating the force. It has been proven that endoscopy could become more useful when combining visual and tactile information [108]. The vision-based sensing mechanism could be adapted in an MIS scenario by embedding sensing technologies to the endoscopic camera, a widely used medical instrument that visualizes and examines the interior of a hollow organ or cavity of the body. Hence, the endoscope could be used as a dual-sensor for visualization and examination of anatomical areas.

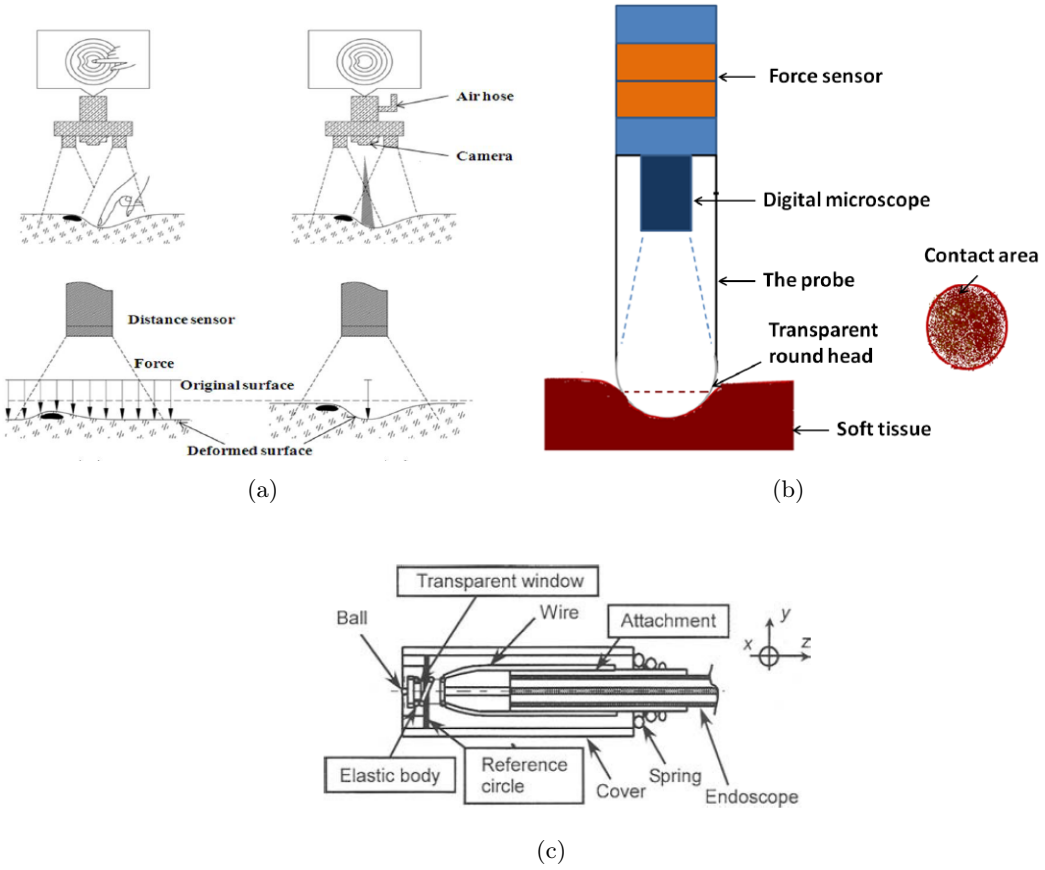

FIGURE 2.10: Vision-based Diagnostic Instruments: (a) The stiffness imager presented in [109] can avoid image occlusions by generating through air jet. (b) Design of the stiffness probe by Li et al. [110]: the microscope visualises the variation of the circular contact area that is used to evaluate the indentation depth. (d) The structure of the tactile sensing system for endoscopic camera proposed in [111]: the movements of the reference circle and the elastic body are related to different elasticity, thus the relative displacement is used to estimate the stiffness.

Along these lines, Kawahara et al. [109] proposed a non-contact stiffness imager for endoscopic camera, as shown in Figure 2.10(a). An air puff applies a force in a particular point and the displacement pattern in the surrounding area is captured by a CCD camera. However, experiments conducted in a human stomach environment showed that the sensor is very sensitive to light changing. Hence, light changing can be erroneously interpreted as variation of the distance due to pushing force. Moreover, the head of the endoscope moves dynamically by a reaction force during the air jet. Consequently, the movements of the camera's head make the estimation of the given force problematic. A tissue diagnosis probe, which is based on stiffness measurements using force combined with vision, has been presented in [110]. The sensing mechanism comprises a digital microscope, a transparent tip mounted on a shaft and a commercially available force/torque sensor. The probe can simultaneously measure the indentation depth and the reaction force generated during contact with soft objects. The indentation of the soft tissues is

mapped on the circular area captured by the digital microscope. The indentation depth increases as the circular area increases. The correlation between the contact area, captured by the microscope, and the indentation depth is combined with the indentation force to estimate the soft tissue stiffness. The design and work principle of the sensor is shown in Figure 2.10(b). Experimental results showed that the proposed sensor can successfully detect abnormalities embedded in silicon phantoms. However, the system can not be used in real time since it is time consuming and cannot identify deep tumours embedded in the surface.

Takashima et al. [111] presented a tactile sensor system for endoscopic camera based on infrared cut pattern and image processing algorithm. The sensor can detect three-axis force and stiffness by employing an image processing algorithm. The computation of the force between the endoscope and the calibre wall can be used to improve the manipulation of the endoscope, while the estimation stiffness can help clinicians in the detection of abnormalities. The tactile sensor is composed by a transparent window, the infrared cut pattern, a reference circle, an elastic body and an attachment between the sensor and the endoscope, as shown in Figure 2.10(c). At rest position, the z-axis of the transparent window is aligned with the axis of the endoscope. Thus, the force along the z-axis is expressed by means of the area occupied by the IR cut pattern, while the forces along x-axis and y-axis are expressed in function of the displacement of the transparent window. During indentation, both the elastic body and the circle will deform as they are subject to different forces; measurement of the deformation will allow the estimation of the compressive modulus modulus as function of the indentation depth, the thickness of the tissue and the radius of the circle. Hence, the proposed sensing system cannot be used in real applications as it requires prior modelling of the tissue to be examined. Furthermore, it can only estimate forces in a small range and cannot be used in real-time. Additionally, noises due to light reflection and complexity of the overall system make this solution impractical.

Nowadays, researchers embed sensing mechanisms in instruments already present in the medical setup, for example in a fibrescope or an endoscope [78]. In this fashion, Iwai et al. [113] developed force sensing technologies for endoscopic/fibrescopic cameras. A flexible pin, which is in the field of view of the endoscopic camera, is used to indent the tissue. The movements of the pin are related to a highly elastic hosiery fabric which can deform even if the applied force is extremely small. Thus, the interaction force is estimated by tracking the area of the visual pin in the image, as presented in Figure 2.11(a). The lateral forces can be derived in function of the movement of the visual pin along image axes [113, 114]. Although the sensing system does not use any electronics and is extremely inexpensive, authors did not consider the movement of the endoscope that

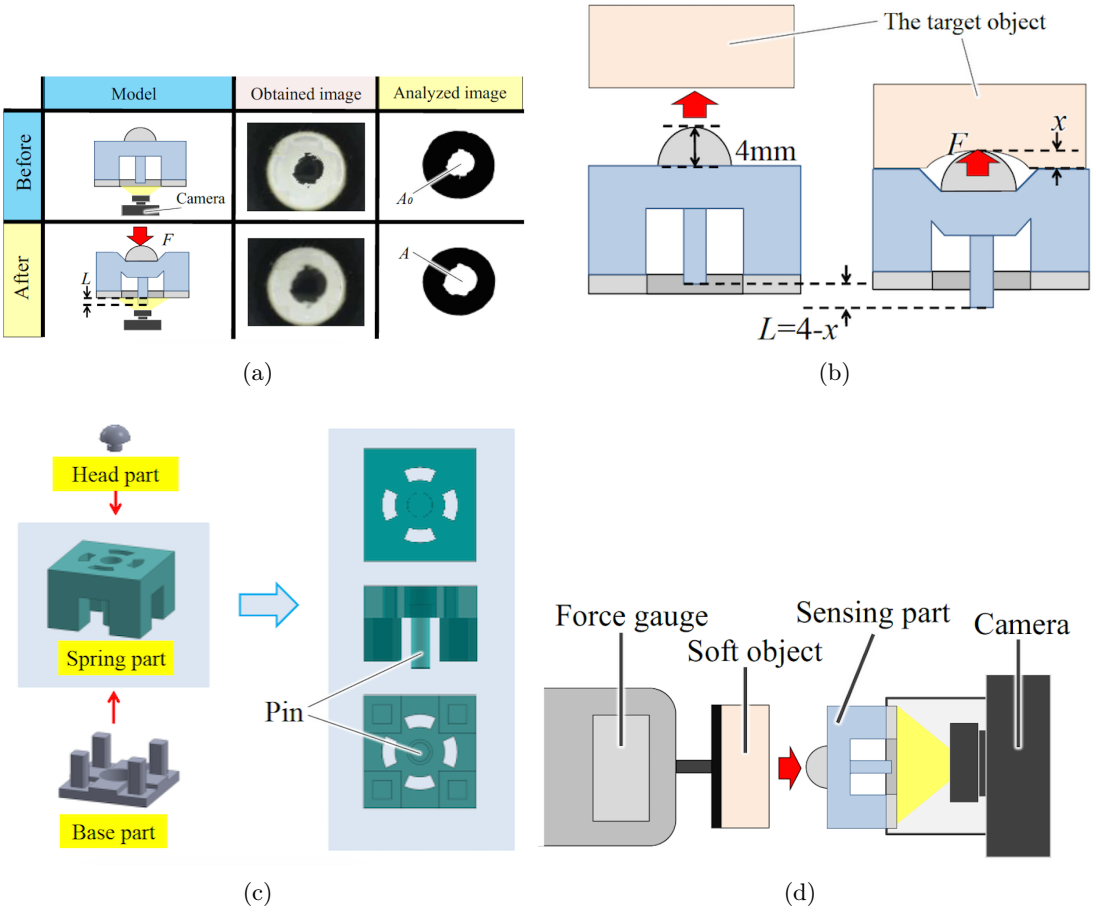

FIGURE 2.11: Visual-based sensing system for endoscopes proposed in [112]: (a) The interaction force is related to the area in the image occupied by the visual pin along the longitudinal axis. (b) The stiffness of the indented object can be derived by considering the force/displacement rate. (c) The design of the sensor (d) The experimental setup of the stress test

may effect the computation of the forces. In addition, authors have validated the sensor only through stress tests. A more thorough investigation needs to be conducted to prove the reliability and accuracy of the proposed sensor. The same principle has been used to develop a stiffness sensor to be attached at the tip of the endoscopic camera [112]. The sensor is composed by a flexible part made of silicone that is placed between the 3D printed base and the head, as shown in Figure 2.11(c). When a force acts on the head of the sensor, the area occupied by the visual pin in the image increases. The stiffness of the indented soft object is derived from the relation between the applied load and the amount of changing of the feature in the image, which reflects the indentation depth (Figure 2.11(b)). Although this work promotes an innovative research area, the stiffness sensor works only if the endoscope is pressed perpendicularly to an ideal flat surface. In addition, experimental results showed that the accuracy of the proposed sensing system decreases with the softness of the indented surfaces. This is not desirable in medical

applications.

2.8 Summary

Robotics solutions have been applied to medical applications to facilitate complex interventions, including surgeries. The advances in sensing technologies have led to a growing number of diagnostic systems which have the potential to provide effective and low-cost solutions. The general purpose of diagnostic devices for medical applications is to replace manual palpation and provide qualitative characterization of soft tissue. Indentation is one of the most exploited diagnostic techniques used to measure reaction forces as well as stiffness of a probed tissue. Generally, indentation systems employ an indenter, which is used to compress the soft tissue, and sensing technologies that are used to compute the reaction force and the indentation depth. Combining the indentation depth and the reaction force the soft tissue stiffness can be estimated. Various approaches have been used to retrieve tactile information during indentation and novel imaging techniques are employed in order to improve the outcome of the diagnosis. The existing indentation devices can not be miniaturized and cannot be easily integrated in the medical environment. Additionally, they are complex and expensive. Novel imaging techniques are promising but, in general, they cannot be used in real-time and are computationally heavy. Thus, errors due to registration make these solutions not reliable. Overall, most of the existing engineering methods for medical examination are still at an experimental stage. Further research in this field is needed in order to mimic the sense of touch and acquire accurate information about soft tissues.

This chapter classified and compared the current techniques used to develop systems for medical diagnosis. It provided a broad overview of the current literature with particular focus on the stiffness sensing technologies based on relative force and diagnostic technologies employing image processing algorithms. Table 2.3 presents a general overview of the current technologies for tumour localization in medical diagnosis, such as manual palpation, medical imaging and instrumented palpation. Although medical experts prefer manual palpation of skin and inner body parts to other diagnostic techniques, this method cannot be used either in remote applications or in minimally invasive interventions. Besides, it is limited in the area accessible to the human hands and strictly dependent on the clinician's skills and experience. Imaging techniques, such as ultrasound, computer tomography and magnetic resonance, are pre-operative methods able to visualize multidimensional representations of internal structures and identify abnormalities. However, the position of the tumours during the surgical procedure is challenging, as movement

Table 2.3: Diagnostic Techniques for Tumour Localization

Technique	**Methods**	**Limitations**	**Advantages**
Manual Palpation	Single or two hands On the skin or inner body part Light or deep	Restricted accessibility Qualitative Difficult to master	Immediate results No electronics Low-cost Preferred by surgeons
Medical Imaging	Radiography Nuclear imaging Tomography Ultrasound	Registration error Noisy intra-operatively Computationally heavy	Representation of the inner body parts Multidimensional images
Elastography	Ultrasound Magnetic resonance	Computationally expensive Limited acquirable characteristics Limited indentation depth Lack of quantitative measurements User-dependent Artefacts	Mapping of the elastic properties Non-invasive Low-cost
Instrumented Palpation	Tactile feedback Force feedback	Sensing array size Sterilisability Integration MIS tools Complexity and hysteresis Miniaturization problem	No-ionizing radiations High sensitivity Precision

of the organs and deformation of the soft tissues causes registration errors. Moreover, imaging techniques are computationally heavy and noisy if used intra-operatively.

Elastography is a new medical diagnostic technique which investigates variation in soft tissue stiffness in order to identify tumours. Elastography maps soft tissue strain by applying stress and visualizing the tissue's response by using different imaging modalities, such as ultrasound or magnetic resonance. Although elastography methods are promising imaging modalities, the algorithms used to process and display the elastographic images are computationally expensive and may affect the medical findings. Furthermore, the determination of the correct pressure to be applied, the lack of quantitative measurements, the limited reproducibility and artefacts are some of the limitations to be resolved if elastogaphy techniques are to be useful in real applications.

Instrumented palpation techniques involve mechanical or electrical devices which are used to induce pressure on the tissue and determine the deformations. Most of the developed instruments are based on tactile and/or force feedback. Despite all the research

efforts, problems related to miniaturization, ergonomics, integration in the medical setup, complexity and reproducibility have to be solved if these instruments are to be used in medical diagnosis.

Instrumented palpation tools are analysed in more detail in Table 2.4 which proposes a classification of the developed devices in accordance to the sensing technology used to characterize the physical contact. Force and tactile feedback can help clinicians to retrieve palpation sensations and localize tumours with high accuracy. However, the limitation of these mechanisms prevent their application in real scenarios.

The diagnostic instruments present in literature can only evaluate the interaction force generated by a contact. In the last decade, researchers have been exploring sensing instruments able to map the stiffness of the anatomical surface.

The soft tissue stiffness can be evaluated by means of the relative force generated during a contact. Table 2.5 shows the sensing technologies employing this principle. In general, these instruments are accurate and reliable. However, fabrication costs and complexity, are only some of the limitations that make their use in the medical setting challenging. Camera sensors can be used to evaluate the tissue deformation during palpation procedures. Thus, image processing algorithms are used to track the tissue deformation generated by the contact. This sensing solution can be embedded in an endoscopic camera and applied in an MIS scenario. An overview of the reviewed vision-based palpation systems is shown in Table 2.6. At present, the proposed technologies cannot be used in real time and present numerous limitations.

This review has shown that no unified sensing system exists in which mechanical properties of the soft tissue are evaluated by using the relative force and image processing algorithm.

TABLE 2.4: Summary of Palpation Instruments for tumour Identification in Medical Diagnosis

Approach	Sensing Technology	Relevant Publication and Year	Advantages	Disadvantages	Diagnostic Application
Force Feedback	Piezoelectric Cantilever	Yegingil et al.“ Probing model tumor interfacial properties using piezoelectric cantilevers ", *Review of Scientific Instruments* (2010) [76].	Shear and Young modulus measurements	Model-based, Offline, Depth sensitivity and Complexity	Breast Examination
	Piezoresistive	Tholey et al.“ On site three dimensional force sensing capability in a laparoscopic grasper ", *Industrial Robot: An International Journal* (2004) [83].	Tip interchangeability and Low friction	Fabrication Cost, Low Accuracy and Hysteresis	Laparoscopy
	Strain Gauge	Arokoski et al.“ Feasibility of the use of a novel soft tissue stiffness meter ", *Physiological Measurement* (2005) [79].	Precision and Reproducibility	User based, Offline and Fabrication Cost	Dermatologic Disorder
		Konietschke et al.“ The DLR MiroSurge - A robotic system for surgery ", *ICRA*(2009) [84].	Sensitivity and Precision	Friction and Fabrication Cost	RMSI
	Optical	Nohn et al.“ Three-Axis Fiber-optic Body Force Sensor for Flexible Manipulators ", *Sensors Journal, IEEE* (2015) [86]	Real-time, Low-cost and Force Range	Light and Temperature Sensitivity, Crosstalk, Hysteresis and Friction	MIS
		Yip et al.“ A robust uniaxial force sensor for minimally invasive surgery ", *EEE transactions on bio-medical engineering* (2010) [87].	Beating heart Compensation and Robustness	Inaccuracy in multi-directional contact, Nonlinearity	Annuloplasty
		Liu et al.“ Rolling Indentation Probe for Tissue Abnormality Identification During MIS ", *Robotics, IEEE Transactions on* (2011) [33].	Surface Sliding	Constant Indentation,Light Sensitivity and Hysteresis	MIS
		Puangmali et al.“ Miniature 3-axis distal force sensor for minimally invasive surgical palpation ", *Mechatronics, IEEE/ASME Transactions on* (2012) [90].	Surface Sliding	Constant Indentation, Light and Temperature Sensitivity and Friction	MIS
	Optical and air flow	Zbyszewski et al.“ A novel MRI compatible air-cushion tactile sensor for Minimally Invasive Surgery ", *IROS*(2009) [89].	Surface Sliding	Constant Indentation and Offline	MIS
Tactile Feedback	Piezoelectric	Frei et al. “Instrument for viscoelastic measurement ", *Google Patents* (1981) [96].	High Sensitivity and Resolution	Model and user based, Robustness and	Breast Examination
	Piezoelectric	Murayama et al.“ Considerations in the design and sensitivity optimization of the micro tactile sensor ", *Ultrasonics, Ferroelectric, and Frequency Control, IEEE Transactions on* (2005) [98].	HIgh Sensitivity and Measurement of elastic and viscose properties	Repeatability and Reliability Issue	Endoscopy
		Hosseini et al. “A medical tactile sensing instrument for detecting embedded objects, with specific application for breast examination ", *The International Journal of Medical Robotics* (2010) [9].	High Sensitivity	Model-based and Offline	Breast Examination
	MEMS	Peng et al.“ Novel MEMS stiffness sensor for in-vivo tissue characterization measurement ", *EMBC* (2009) [100].	High Dynamic Range, Linearity and Sensitivity	Challenging Positioning Complex and Small Force Range and Indentation	MIS

TABLE 2.5: Summary of Stiffness Sensing Palpation Instruments based on Force Difference

Sensing Technology	**Relevant Publication and Year**	**Advantages**	**Disadvantages**	**Specification**	**Diagnostic Application**
PVDF films	Dargahi et al.“ Modelling and testing of a sensor capable of determining the stiffness of biological tissues ", *Electrical and Computer Engineering, Canadian Journal of* (2007) [99].	Low-cost, High Dynamic Range, High Sensitivity and Signal-to-noise ratio	Small Elasticity Range, Charge leakages and Friction	Max Force: 1N Error: 5%	Breast Examination
MEMS	Peng et al.“ Novel MEMS stiffness sensor for in-vivo tissue characterization measurement ", *EMBS* (2009) [100].	High Sensitivity	Small Stiffness Range	Force Range: [0.35N-0.55N] Force Resolution: 0.2mN Stiffness Resolution: 0.2MPa	MIS
Piezoresistive	Bab et al.“ Micromachined Tactile Sensor for Soft-Tissue Compliance Detection ", *Microelectromechanical Systems, Journal of* (2012)[94].	High Stability and Independent of the Indentation Depth	Miniaturization Problems,Low accuracy and Sensitivity to Bending	*E*- Range:[0-1MPa] Sensitivity: 0.014 Error: 7.25%	MIS

TABLE 2.6: Summary of Visual-based Palpation Instruments for Medical Diagnosis

Sensing Technology	**Relevant Publication and Year**	**Advantages**	**Disadvantages**	**Specification**	**Diagnostic Application**
CCD Camera & Air-jet	Kawahara et al.“ Non-contact stiffness imager for medical application ", *Information Acquisition, 2005 IEEE International Conference on* (2005) [109].	No physical contact	Low Accuracy, Light and Motion Sensitivity	Resolution: 0.05 Nmm	Endoscopy
Microscope & Commercial F/T sensor	Li et al. “ A stiffness probe for soft tissue abnormality identification during laparoscopic surgery ", *World Automation Congress (WAC)* (2012) [110]	Stiffness measurement Surface siding	Small Indentation Range, Offline and Time consuming	x-axis Error: [0.28 mm-1.54 mm] STD: [1.64 mm-2.52 mm] y-axis Error: [0.32 mm-1.98 mm] STD: [1.12 mm-1.96 mm]	Laparoscopy
Infrared Cut Pattern	Takashima et al. “ Vision-based Tactile Sensor for Endoscopy ", *Complex Medical Engineering* (2007) [111].	Low-Cost and MRI compatible	Small Force Range, Light Sensitivity and Model-based	Resolution: 0.015 Nmm	Endoscopy
Elastic Element & Commercial Camera	Iwai et al. “ Visualization method based stiffness sensing system for endoscopes ", *Engineering in Medicine and Biology Society (EMBC), 2015 37th Annual International Conference of the IEEE* (2015) [112].	Stiffness Measurement	Small Force Range, Complex and Low accuracy for soft material	Force Range: [0-0.5] Nmm Error:25 %	Endoscopy

CHAPTER 3

Vision-based Stiffness Sensing Principle

This chapter analyses the principle of a vision-based stiffness sensing mechanism. The proposed sensory system employs the development of a mechanical structure in which multiple elastic components are embedded as well as a camera sensor used to capture their movements. Each elastic element is jointly linked to a small body, a representative feature of a specific geometric shape, which is always enclosed in the camera's field of view. Hence, when the interaction with an external surface triggers the movement of the elastic element, the geometric feature changes its position and size in the camera's field of view. The interaction force exerted by each elastic element is computed by tracking the correlated geometric feature in the image. To validate the sensing principle a vision-based force sensor has been developed and tested. Experimental results with a benchmarking sensor showed that the derived model can compute the interaction force with high accuracy. Therefore, if contact force can be derived by employing only one elastic element, two elastic elements of different springiness can be used to generate two different forces. Thus, the contact stiffness can be estimated by means of the relative force.

3.1 Introduction

Changes in tissue stiffness may be an indication that cancer is present and thus one of the points of interest within the robotics and haptics research community has been the development of methods of tissue elasticity measurement. Researchers have explored several instruments and methodologies to describe organ response to an applied load and estimate the indentation forces. These forces can be used to evaluate the mechanical properties of the soft tissue. Linear elastic modelling of soft tissues is the most widely used approach. This model assumes that the tissue obeys the generalized Hooke's law; thus, similarly to springs, it is able to resume its configuration after the application of a force. Fung et al. [115] demonstrate that if the displacement induced in the soft tissue is small, the physical response can be modelled using the linear approximation but as the displacement increases, the linear elastic model becomes inaccurate.

In this thesis, the stiffness of the soft tissue is computed by means of the relative force generated during indentation. The developed sensory system comprises an indentation device in which several elastic elements are embedded; these elements are related to small bodies (spheres in this case), and a camera sensor. During palpation procedures, the movements of the elastic elements trigger the sliding of the spherical features towards the camera; thus, the deformations induced in the tissues are computed by relying on an image processing algorithm. A mathematical model estimates the contact forces by tracking the visual appearance of the geometric features in the camera images. Chapter 2.6 presents the current state of the art in palpation instruments based on the relative force principle. Despite the research efforts, the limitations showed in Table 2.5 make their use impractical. The vision-based stiffness sensory system proposed here overcomes these limitations, as it works in real-time and does not make use of any electronic components. In addition, it has a customisable range and resolution and can be easily miniaturised. Therefore, it is suitable for medical applications. Moreover, the sensing principle can be applied in situations where it is required to estimate forces and stiffness of soft objects, e.g. robot navigation [27], manipulation and grasping of deformable objects [116, 117].

The computation of the force is the basis of the sensing principle. This chapter proves the validity of the proposed model by presenting a vision-based force sensor.

3.2 Vision-based Stiffness Sensing: Working Principle

The customised sensor makes use of small spheres, which are always in the camera's field of view and connected to elastic elements, e.g. linear springs of known elasticity. The

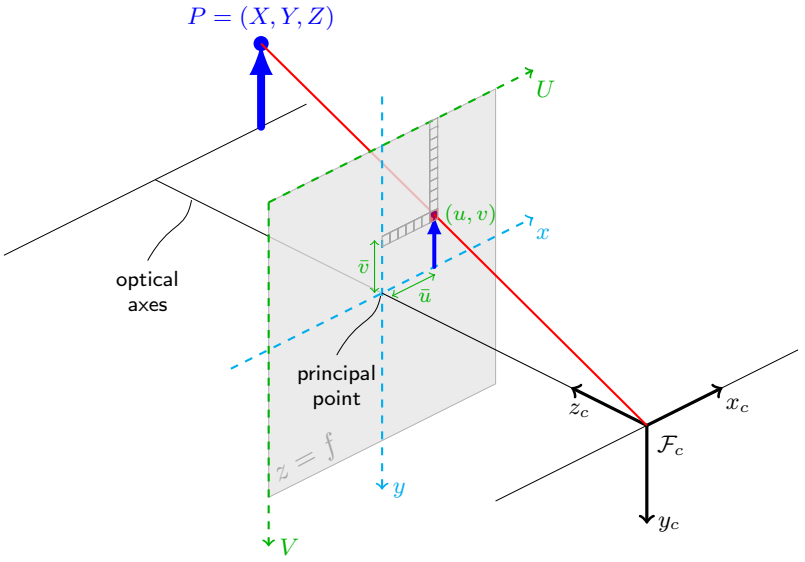

FIGURE 3.1: Camera Projection Model: A 3D world point $\mathbf{P}=(X, Y, Z)$ is projected into 2D pixel coordinates $\mathbf{Q}=(u, v)$ in the camera image.

movements of the springs trigger the movements of the spheres generating a variation of their visual appearance in the camera images.

During the interaction with external soft surfaces, the force applied by each elastic element is retrieved by tracking the movements of the visual features in the images. The elastic elements present intrinsic Young's modulus, thus, when indenting soft tissues they generate specific reaction forces. A mathematical model computes the interaction forces in real-time relying only on a visual processing algorithm.

The pinhole camera model, described in Appendix A, has been used here as a first order approximation of the mapping from a 3D scene to a 2D image.

Considering a point $\mathbf{P}$ in the global coordinate system at $\mathbf{P} =(X, Y, Z)$ and its projection $\mathbf{Q} = (u, v)$ in the camera frame, it is possible to define the relation between the 3D coordinate of $\mathbf{P}$ and the coordinate of $\mathbf{Q}$ in (u,v) as shown in Figure 3.1. From the properties of similar triangles, using homogeneous transformation, it follows that:

$$\begin{pmatrix} u \\ v \end{pmatrix} = -\frac{f}{Z} \begin{pmatrix} X \\ Y \end{pmatrix} \tag{3.1}$$

Assuming that the 3D spheres in the camera's visibility cone are visible in the camera image and their dimensions are known, it is possible to relate the dimensions of the spheres' representation in the 2D camera image to the actual distance between the camera and the spheres, as the dimension of the imaged object is inversely proportional to the camera-object distance, as shown in Figure 3.2.

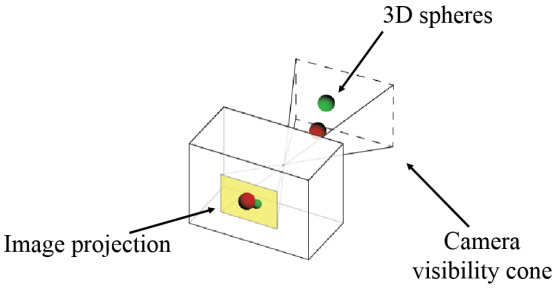

FIGURE 3.2: Object-Camera Distance Relation: The projection of a 3D object on the camera image depends on its distance to the camera. Objects that are close to the camera (red sphere) will appear bigger on the projected image than objects that are further away (green sphere).

In the proposed sensing mechanism, the visual appearance of the features in the images is related to the movements of elastic elements presenting different and known degrees of stiffness. The analogy between the distance of an object from the camera's centre and its projection onto the image is used for evaluating the reaction force generated through indentation.

3.2.1 Uni-axial Force Sensing Principle

The uni-axial indentation of a single degree of freedom (DOF) elastic body, for example a spring with spring constant k, onto a soft surface, generates a reaction force $\mathbf{F}$, as shown in Figure 3.3. Modelling the soft surface as a linear-elastic material, if the indentation Δx is small, the reaction force follows Hooke's law as :

$$F = k\Delta x. \tag{3.2}$$

In uni-axial indentation, the force applied by the elastic element acts only on the axis

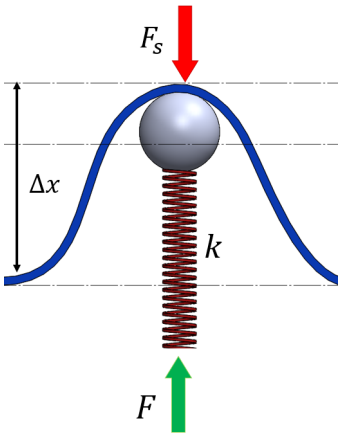

FIGURE 3.3: Force sensing principle: Contact between the soft surface and an elastic element showing the interaction force(F, F_s) and the displacement of the tissue Δx.

perpendicular to the surface, thus the reaction force is in the opposite direction and it follows Equation 3.2. Therefore, the reaction force is dependent on the indentation depth and the stiffness of the elastic element.
The deformation of the soft tissue, thus the value of Δx in Figure 3.3, can be estimated by using various sensing systems. Here, visual information is used to estimate Δx, thus to derive the reaction force.

3.2.2 Uni-axial Stiffness Sensing Principle

The contact between a soft surface and two elastic bodies, for example two springs with different elasticity, k_1 and k_2, with $k_1 > k_2$, will generate two different reaction forces. If the elastic elements are pushed by the same force against a soft surface, they exhibit different displacements (i.e. the elastic element with a lower elastic constant is displaced more than the element with a higher elastic constant as shown in Figure 3.4). Since the

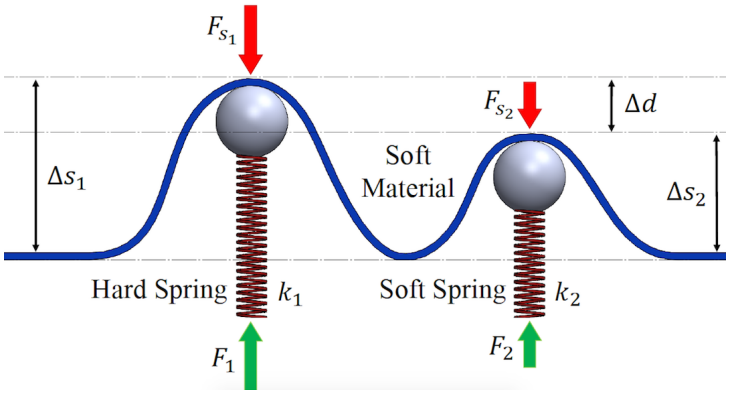

FIGURE 3.4: Stiffness sensing principle: Contact between the soft surface and two elastic elements of different elasticity showing the applied and reaction forces $(F_1, F_2, F_{s1}, F_{s1})$ and the differential displacement (Δd).

two indenters are very close to each other, the deformation sensed by one indenter may be caused by the contact of the other indenter. Modelling the soft surface as a homogeneous, linear elastic material, Hooke's law can be used to describe the interaction:

$$F_1 = k_1 \Delta x_1 = ks \Delta s_1 = F_{s1}; \tag{3.3}$$

$$F_2 = k_2 \Delta x_2 = ks \Delta s_2 = F_{s2}. \tag{3.4}$$

From Equations 3.3 and 3.4, the stiffness of the surface k_s is derived as:

$$k_s = \frac{F_1 - F_2}{\Delta s_1 - \Delta s_2} = \frac{(k_1 \Delta x_1 - k_2 \Delta x_2)}{\Delta d}. \tag{3.5}$$

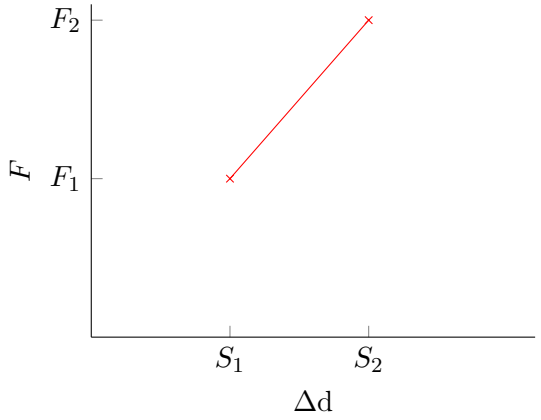

FIGURE 3.5: Computation of the stiffness: Applying forces F_1 and F_2, the soft surface will be deformed by S_1 and S_2 respectively. These two values will define a line in the F - Δd space. The slope of this line represents k_s.

Applying forces F_1 and F_2, the soft surface is deformed by S_1 and S_2 respectively. These two values define a line in the F - Δd space. The slope of this line represents k_s as shown in Figure 3.5.

3.3 Real-time Feature Tracking

The image processing algorithm employs open source computer vision (OpenCV), a cross-platform library of programming functions for real time computer vision applications. The OpenCV library is interfaced in Robot Operating System (ROS), a collection of software frameworks for robot software development, through the "vision_opencv" package. The image processing algorithm detects and tracks coloured geometric features in an image. The ROS camera calibration toolbox was used to estimate the intrinsics parameter of the camera and the distortion coefficients used to rectify the images . After the rectification, each image is filtered in the HSV colour space in order to select the feature's colour. The HSV colour space is a cylindrical representation of points in an RGB colour model. In each cylinder, the angle around the central vertical axis correspond to "hue", the distance from the axis correspond to the "saturation" and the distance along the axis correspond to the "value", as shown in Figure 3.6. A script enables the specification of the colour associated to the feature on-line, thus the HSV interval can be adapted to the illumination of the environment or the change of colour of the visual features.

During the interaction with external surfaces, visual features of a predefined shape, in this case spherical, appear and move in the images. The tracking of the spherical features is performed in the filtered grayscale image which is the output of the HSV colour filter. Morphological image operators are applied in the black and white image to select the pixels corresponding to the spherical features and remove the noise. On the filtered image,

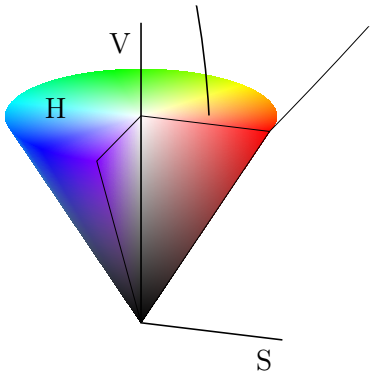

FIGURE 3.6: Cut-way 3D model of the HSV Colour Space: A color **H**ue is described in terms of its **S**aturation and **V**alue or luminance.

Gaussian blur is employed to eliminate false positives, while maintaining the minimum time-bandwidth product. Sequence applications of two morphological primitives, such as dilatation and erosion, are performed to fill inner fragmentary regions and eliminate the bays along the corners. Hence, the implemented algorithm successfully detects the geometric properties of the visual features in the image, as shown in the block diagram in Figure 3.7.

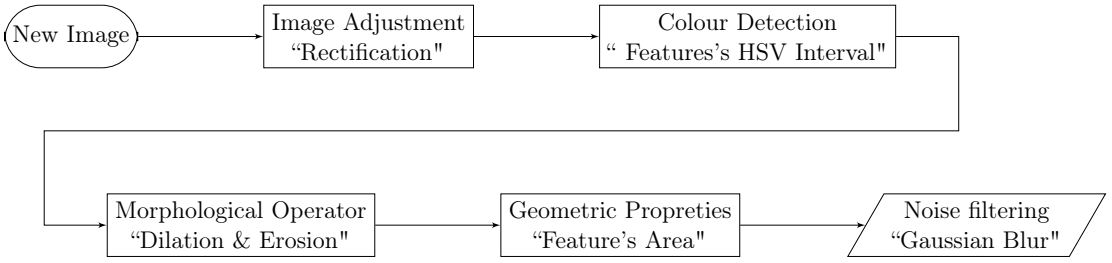

FIGURE 3.7: Schematic Representation of the overall Image Processing algorithm.

3.4 Vision-based Force Sensor

The sensing system uses visual feedback to determine physical interaction forces with soft tissues. The correct estimation of the force is crucial for modelling the stiffness which is dependent on the relative force, i.e. the differential force between the elastic elements. To prove the feasibility and test the accuracy of the model, an uni-axial vision-based force sensing device has been manufactured and tested. The next sections present the design of the prototype, the visual processing algorithm, the mathematical model and the results of the experimental tests.

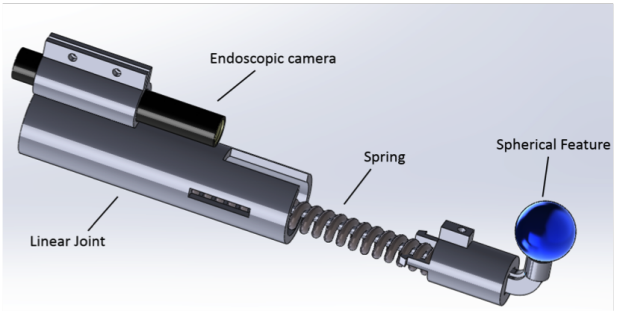

FIGURE 3.8: Vision-based Single Axial Force Sensor: CAD drawing showing the spring embedded inside a linear joint.

3.4.1 Vision-based Force Sensor Design and Image Processing Algorithm

A CAD drawing of the developed sensory device is shown in Figure 3.8. The disassembled parts and the manufactured sensor are shown in Figure 3.9. The vision-based force sensor consists of a spring-driven linear shaft which is inserted into a cylindrical housing in order to prevent lateral movement of the embedded spring. A spherical feature is used to "visualize" interaction forces. This assembled mechanism is attached to a camera as presented in Figure 3.9(b). The spherical visual feature is always in the visibility cone of the camera. As the sphere interacts with soft tissues, the spring embedded in the structure is compressed and the distance between the camera and end-effector is modulated. The sensor is small in size as shown in Figure 3.9(a) where it is compared to a 50 pence sterling coin. The spherical feature has a diameter of 5 mm, the spring length is 35 mm and the linear shaft is 15 mm long. The commercial USB camera has an outer diameter of 7 mm, a resolution of 640x480 and a frame rate of 30 frames/s. The approach to sensor design was guided by the following points: the final system was expected to

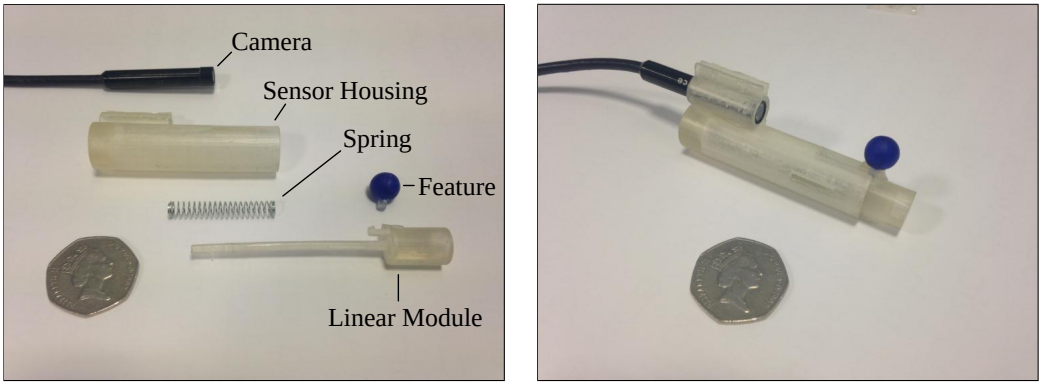

(a) (b)

FIGURE 3.9: Vision-based Force Sensor: (a) Disassembled and (b) Assembled Force Sensor Prototype.

be compatible with minimally invasive scenarios and the geometric feature to be easily miniaturised and integrated with a generic endoscopic camera. Satisfying these design considerations, the geometric feature has been placed on the optical axis. The sphere can be mounted directly on the linear sliding shaft or on the end-effector and is in direct contact with the surrounding objects. The mechanical structure of the sensor has been designed in SolidWorks and manufactured with a rapid prototyping machine (Project HD-3000 Plus, 3D Systems). The Project rapid prototyping machine employs a large number of printing jets to print objects in 3D. Using this machine to manufacture the novel sensing mechanism allows miniaturisation. The range of force that the sensor can measure is relative to the elastic constant of the spring embedded in the mechanism and the camera-sphere distance, thus it can be easily customised. The minimum observable change in force that defines the sensor's resolution corresponds to the force needed to change the area of the visual feature by 1 pixel. This value depends on the resolution of the camera and the camera-sphere distance and it increases when the object comes closer.

The visual processing algorithm, presented in Section 3.3 has been used here to track the spherical visual feature in real-time. The OpenCV's function "HoughCircles" that implements the Circle Hough Transform (CHT) using the Gradient Method has been used to track the spherical visual features. This method finds the parameters of a circle when a number of points that fall on the perimeter are known. The HCT function firstly performs the edge detection using the OpenCV function "cvCanny()", and then evaluates the local gradient for every non-zero pixel in the edge image.

The Hough Circle Transform is proved to be sensitive to light disturbance in the environment, a fact that affects the threshold of the edge detector and results in noisy and inaccurate detection of the circle, as shown in Figure. 3.10(a). Instead of using the HCT, after filtering the image in HSV colour space, this problem is overcome by using the morphological operators in the black and white image to select the equivalent pixels in the HSV interval.

Two morphological operators, dilation and erosion, are then applied in sequence in order to fill inner fragmentary regions and remove bays along the corners. Gaussian blur is employed to eliminate false positives and reduce the noise. Finally, important properties of the images, such as area, can be determined.

A comparison between the proposed algorithm and the the OpenCV's implementation of the Circle Hough Transform is shown in Figure 3.10(a). The improvement in the detection and robustness to occlusions can be observed in Figure 3.10(b). The image processing algorithm detects and tracks the radius of the spherical visual feature which is used to model the interaction force.

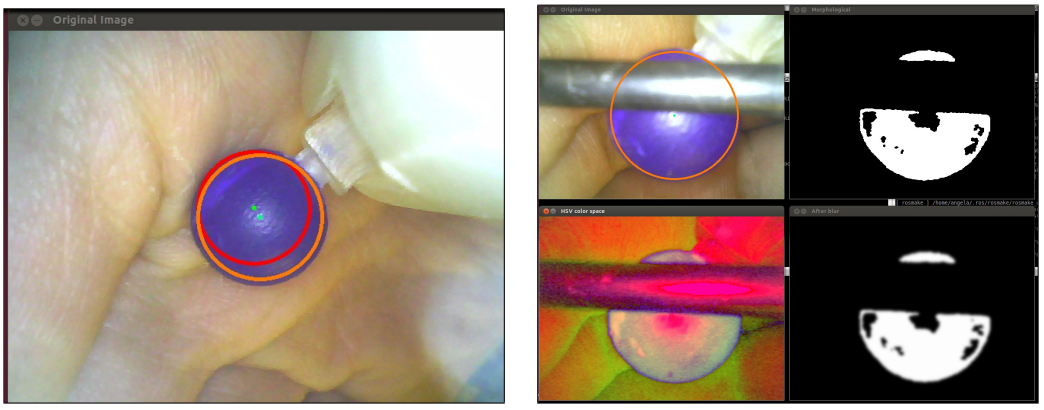

(a) (b)

FIGURE 3.10: Visual processing algorithm: (a) Feature Detection using OpenCV HoughCircle (in red) and the proposed Algorithm (in orange) (b) Vision Performance during Occlusions. The image at the bottom left illustrates the transformation of the input image into HSV colour space. The output of the morphological operation is shown on the image at the top right. The bottom right image shows the blurred image.

3.4.2 Computation of the Spring Parameter

The validation of the proposed method and a system stability analysis have both been performed through stress tests with a benchmarking sensor, namely the force/torque sensor NANO 17 by ATI (SI-12-0.12, resolution 0.003 N employing a 16-bit data acquisition card).

In the experimental setup the ATI Nano17 is fixed on a motorised linear track and pushed against the vision-based force sensor. This generates a force that compresses the spring embedded in the sensor's structure.

The force exerted by the force/torque sensor is recorded using LabView software in order to compute the spring constant, while the image processing algorithm tracks the spherical feature in the image, as shown in Figure 3.11. The results of the experimental tests are shown in Figure 3.12. The relation between the force and the displacement is defined by the constant of the spring embedded in the sensor's structure and was computed using Matlab linear fitting. The estimated value is 177.9 N/m; this results match the weight displacement trend which was evaluated by applying a weight and measuring the displacement of the spring.

3.5 Tracking of the Feature's Radius to Estimate Force

The pinhole camera model described in Appendix 3.2 has been used here to model the relation between the sphere's dimension in the 2D image and the distance computed by

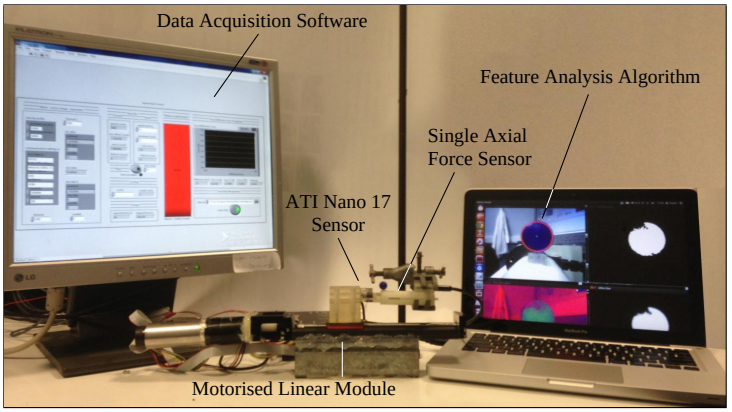

FIGURE 3.11: Vision-based force sensor stress test: The benchmarking sensor is fixed on a motorised linear module and pushed against the proposed force sensor. The image processing algorithm computes the visual feature's radius in real-time and simultaneously the force from the ATI Nano17 sensor is recorded.

the sensor during the contact. The visual feature has a spherical shape and due to the structure of the sensor it can only move along the axis perpendicular to the camera. The changing dimension of the visual feature, thus the variation of the sphere's radius in the image, is related to the sphere-camera distance. If r is the sphere's radius, x the sphere-camera distance and h the projection of the radius in the image plane, from Equation 3.1 follows:

$$\frac{h}{x} = \frac{r}{f}. \tag{3.6}$$

Equation 3.6 can be used to express every new position of the feature in function of initial camera-sphere distance x_0 and the initial value of the radius in the projected image r_0. The value of x_0 and r_0 are known and chosen during the design process. Figure 3.13 shows the relation between these parameters and the current value of the

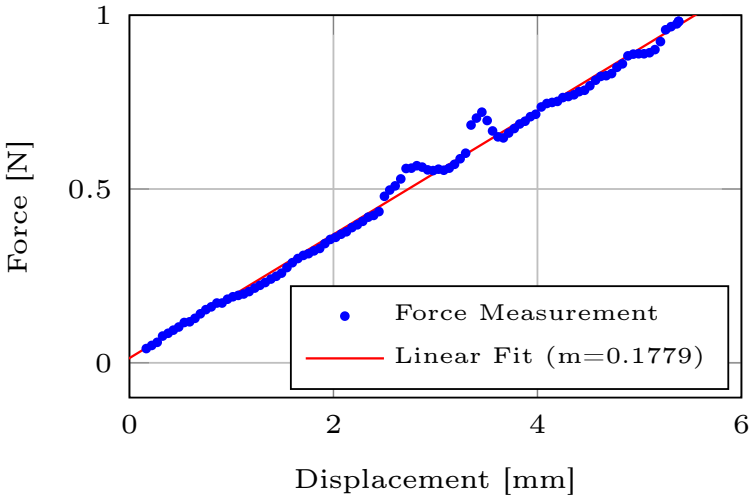

FIGURE 3.12: Experimental Result of the Stress Test: The elastic constant of the spring is the slope of the line obtained through linear fitting of the experimental data.

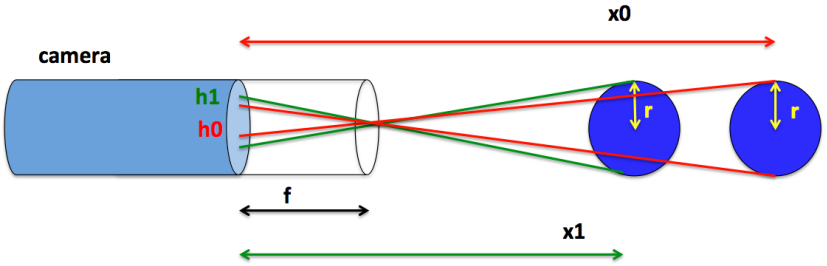

FIGURE 3.13: Sphere's Projection in the Image Plane: The dimension of the projected sphere in the image is inverse proportional to the sphere-camera distance.

spherical feature's radius "x". From geometrical consideration follows:

$$x = \frac{hf}{r} = \frac{x_0 r_0}{r}; \tag{3.7}$$

from which follows the expression of Δx:

$$\Delta x = x_0 - \frac{r_0}{r} x_0. \tag{3.8}$$

Replacing the expression of Δx, derived in Equation 3.8 in the Hooke's law for the force response of springs, it follows the expression of the force value in function of the circle radius:

$$F(r) = k x_0 \left(1 - \frac{r_0}{r}\right). \tag{3.9}$$

In Equation 3.9, k represents the constant of the compression spring embedded in the sensor's structure. For the designed sensor, the camera-sphere distance in rest conditions (i.e. when no force is applied to the sensor), x_0 is equal to 42 mm and the corresponding value of the visual feature's radius in the image r_0, is 94 pixels. The mathematical model computes the force in function of the initial radius r_0 and initial feature-camera distance x_0, thus a changing in the sensor design requires their redefinition. The analysis of the performance considers the Root Mean Squared Error (RMSE) that represents the square root of the mean/average of the square of all of the error. Thus, RMSE amplifies and severely punishes large errors. The RMSE is expressed as :

$$\text{RMSE} = \sqrt{\frac{\sum_{t=1}^{n} (y - F(r))^2}{n}} \tag{3.10}$$

The relationship between the force computed by the ATI Nano17 and the radius in the image is reported in Figure 3.14. The mathematical model derived has a RMSE of 0.0404 and does not fit exactly with the experimental data.

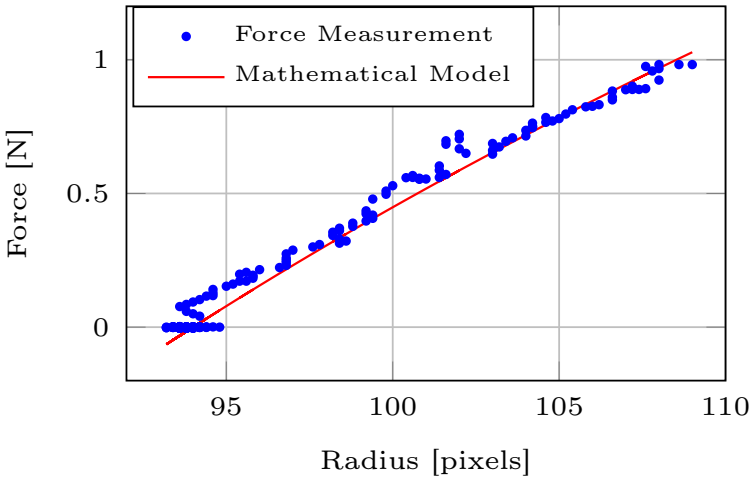

FIGURE 3.14: Mathematical Model: Linear Regression between the visual feature's radius and the force computed by the benchmarking.

3.6 Experimental Results

A mathematical function that computes the value of the force in terms of the feature's radius was derived using Matlab's Curve Fitting Tool. Figure 3.15 shows the fitted curve which is obtained using the rational function in Equation 3.11. As the mathematical model was derived in the previous chapter, there is no risk of overfitting.

$$F(r) = a_1(1 - \frac{a_2}{r}). \tag{3.11}$$

In Equation 3.11 the values of a_1 and a_2 are 7.143 and 91.94, respectively. The RMSE for this fitting is 0.03 and has a prediction interval of 95 %.

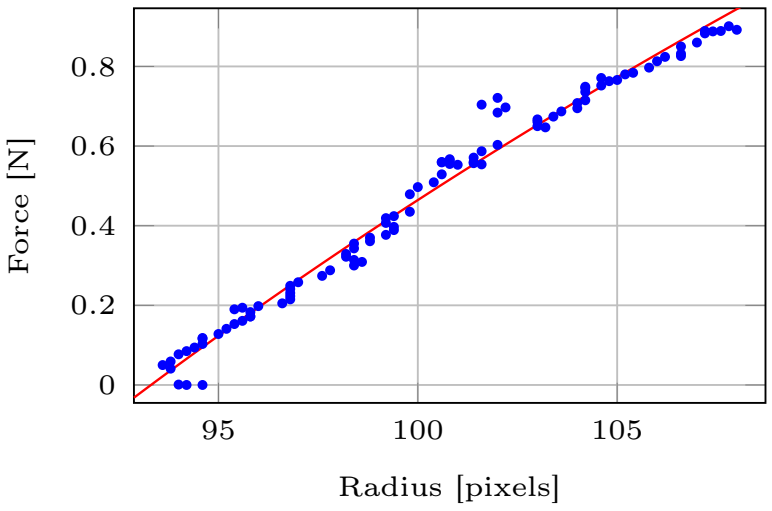

FIGURE 3.15: Experimental Model: The Rational Function in Equation 3.11 represents the best fitting of the experimental data.

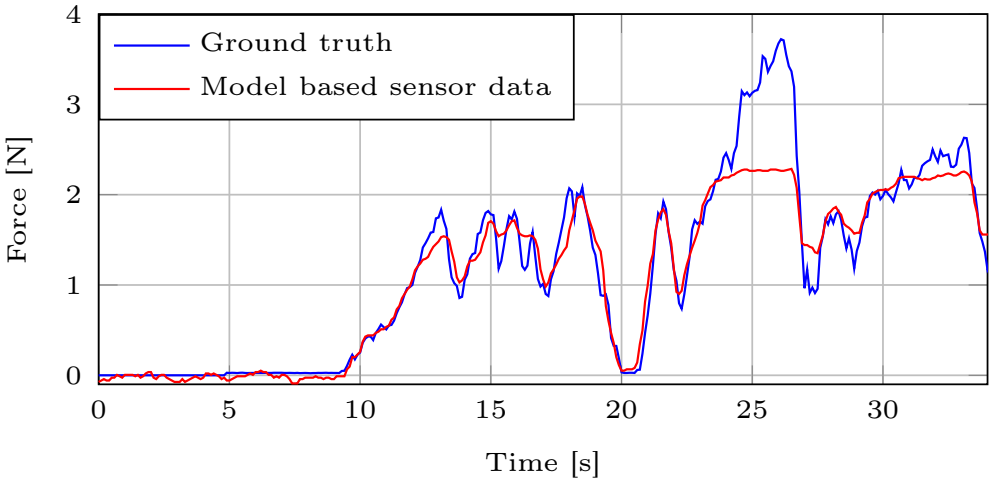

FIGURE 3.16: Experimental Results: During the test, the vision-based force sensor was manually pushed against the benchmarking sensor. The plot shows the force exerted on the ATI Nano17 F/T sensor (in blue) and the forces computed using the derived model based sensor data (in red).

The validation of the models was obtained performing experimental tests in which the vision-based force sensor was manually pushed against the benchmarking sensor ATI Nano 17. Both models perform well, failing only when the force goes above the sensors' range, which is lower than the benchmarking sensor, saturating it as shown in Figure 3.16. This value can be customised as it depends on the camera-sphere distance and the value of the spring constant. The sensor is also affected by friction, thus its response in speed is low (Figure 3.16). However, in medical examinations, high speed responses are not an essential requirement. When the vision-based force sensor was not saturated, the RMSE was 0.15 for the mathematical model and 0.14 for the experimental model. The spring allowed a range of $0 - 1.96$ N and a variable resolution between 0.0439 N and 0.0787 N.

3.7 Summary

In this chapter, a vision-based force sensing principle was presented. The sensing mechanism computes the indentation force, which is exerted on the tissue by an elastic element, by tracking the correlated visual appearance of a spherical feature in the images. Experimental results have shown that the mathematical model derived presents a good approximation of the experimental data obtained through benchmarking with a very accurate commercial force sensor, such as the ATI Nano17.

The vision-based force principle is the mathematical foundation of the proposed stiffness sensing mechanism, as the contact between a soft surface and two elastic mechanism of different elasticity will produces two different forces. The stiffness of the soft surface is

related to the relative force between the elastic elements which is computed by an image processing algorithm.

CHAPTER 4

Vision-based Stiffness Sensor for Endoscopic Examination

Endoscopic cameras are inspection instruments widely used in non-invasive medical procedures to visualise and examine organs and inner body parts. The endoscope can be inserted into the patient's body through a natural opening or by using a trocar port (a small incision in the patient's skin). In minimally invasive procedures, several trocar ports are made to serve as insertion points for surgical instruments. One of those trocar ports is reserved for the endoscopic camera through which the surgeon can visualise the procedure in a magnified image on a video monitor. This chapter presents a novel stiffness sensor which is fashioned for a surgical endoscopic camera. A clip-on sensing mechanism is used to enhance the functionalities of the endoscopic camera that can be converted from a traditional visualization sensor to a stiffness sensor. The computation of soft tissue stiffness will help clinicians to diagnose abnormalities and recover the "sense of touch" that is completely absent in minimally invasive and remote applications.
The developed vision-based sensing mechanism has been used to estimate the stiffness of silicon phantoms. The experimental results have shown that the accuracy and sensitivity of the system increases with the softness of the examined tissue, hence, the system is potentially suitable for medical examination. This chapter presents the design, the image process algorithm, the modelling and the experimental results of the sensory system.

4.1 Introduction

Minimally invasive procedures use state of the art technology to reduce damage to human tissues that can occur during medical interventions. In the diagnosis and treatment of diseases, it is crucial to localise malignant tissues and identify abnormalities while preserving blood vessels and nerves. In traditional open surgeries, soft tissue characterisation is performed directly by surgeons through manual palpation. This simple process becomes challenging in minimally invasive procedures where electronic instrumentations and sophisticated signal processing techniques have to replace and mimic the clinician's hands to recover tactile sensations. Currently, minimally invasive and remotely performed medical procedures are limited by the lack of tactile feedback. In addition, all palpation instruments developed to date require a dedicated port. Hence, clinicians can only rely on their vision in order to estimate the interaction forces between a surgical device and a soft tissue, that is, they depend on their visual observations of the tissue's deformations as these appear on the images fed back by the endoscopic camera in real-time.

In the last decade, computer vision techniques, which are directly implemented on the endoscopic camera images, have been largely investigated [118]. The use of these images does not require the sensor to be integrated and tested in a clinical setting, as is the case with other sensing systems, because the endoscopic camera is already part of the medical equipment [119]. However, visual approaches estimate the 3D shape of the anatomical surfaces by employing costly image processing algorithms which can not be used in real-time. Alongside surgical vision solutions, endoscopic camera images have also been explored in order to retrieve tactile information by combining mechanical devices, which interact with the soft tissue, and image processing algorithms, which estimate the tissue properties [109–112].

In this chapter, the sensing principle introduced in Chapter 3 is used to develop a stiffness sensor tailored for a surgical endoscopic camera. The estimation of the stiffness is associated to the forces generated by two springs presenting different elasticity; these springs are embedded in the mechanism and jointly-related to small spheres. Image processing is employed to track the spherical features and measure the interaction forces. The soft tissue stiffness depends on the relative force between the two springs which is generated during contact. The proposed sensory mechanism enhances the utility of the endoscopic camera by adding tactile capability to the traditional visualization functionality. Tactile capability is used to characterize the soft tissue and in particular to estimate its stiffness.

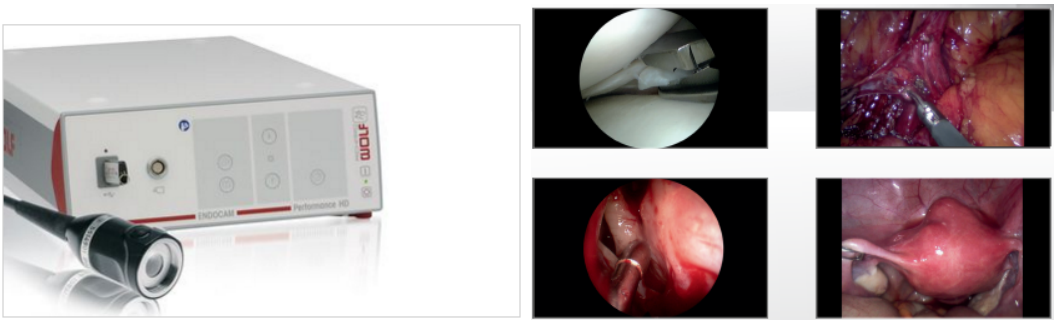

(a) (b)

FIGURE 4.1: The ENDOCAM® Performance HD: (a) A picture of the camera system. (b) The images obtained by using different zoom lens.

4.2 Endoscopic Examination

Endoscopy is a medical procedure in which a thin tube with a camera (endoscope) is inserted into the body to diagnose or to treat a health condition. Endoscopes are part of a family of optical devices used by clinicians to see inside the human body. The optical instrument is inserted into the patient via body orifices or trocars. The endoscope moves through body cavities, hollow organs or passageways and captures images that clinicians can show on a screen and use for the examination. In general, endoscopes have a diameter between 10mm and 12mm, and contain a light delivery system, which is usually fibre optic with the light source outside the body, an image system for the visualization, and an optional channel used for the insertion of other instruments or manipulators [120]. Doctors use endoscopy to investigate a specific part of the body to either diagnose disease or find the cause of a patient's symptoms. The length and flexibility of the endoscope depends on which part of the body needs to be viewed. In addition to being a diagnostic tool, an endoscope can be used to treat or prevent a disease from occurring. For example, during colonoscopy, an endoscope can be used to remove a colon polyps, which could potentially develop into cancer if left in place. An endoscope may also be used to perform laparoscopic surgeries through small incision in the skin. There are three imaging systems used with endoscopes: fibre optic endoscope, rod lens, and the charge-coupled device (CCD). The fibre optic endoscope is the oldest type of endoscope in continuous use despite it being limited by the resolution of image it can provide. The rod lens system provides a much more detailed image than fibre optics. It is also capable of a much wider viewing angle than older conventional lens endoscopes and laparoscopes. The charge-coupled device (CCD) uses the same integrated circuit chip as the one found in digital cameras. In this type of imaging system an CCD chip is placed at the end of the laparoscope, where it can directly capture the video image without having to transmit it through other optical elements. The image is then projected on to

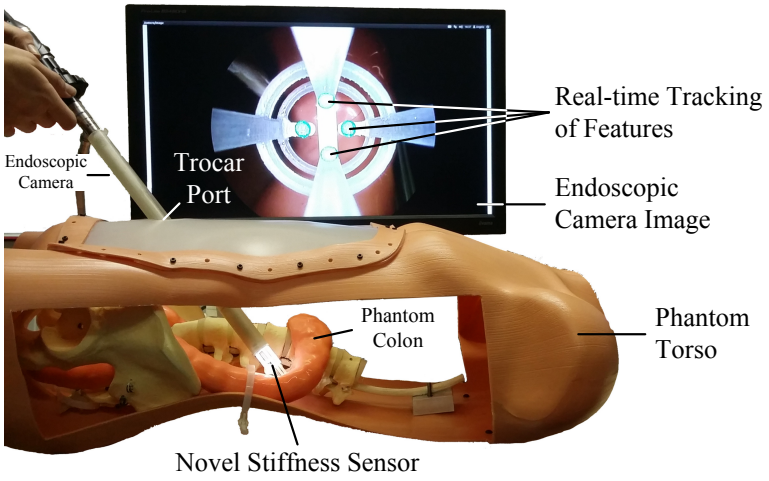

FIGURE 4.2: Vision-based stiffness sensor mounted on a surgical endoscopic camera inside a phantom torso

a monitor for the doctor to view it. The rod lens systems are often referred to as digital endoscopes laparoscopes. Endoscopes can be rigid or flexible depending on the intended usage. Generally speaking, a rigid endoscope is easier to control and less expensive to manufacture. Therefore, rigid endoscopes are much more common. The stiffness sensor presented in this chapter has been designed for rigid surgical endoscopic camera ENDOCAM® Performance HD by Richard Wolf GmbH (30 fps at 60 Hz), currently used in the surgical theatre, but the sensor can be adapted to any surgical camera. The ENDOCAM® Performance HD shown in Fig. 4.1(a) has been designed for universal endoscopic application. If combined with a zoom lens, ENDOCAM can cover the entire spectrum of endoscopy as shown in figure 4.1(b).

4.3 Vision-based Stiffness Sensor: Design

The assembled prototype of the designed probe mounted on the surgical ENDOCAM® by Richard Wolf and inserted into a human phantom torso is shown in Figure 4.2. An exploded view of the probe's drawing is shown in Figure 4.3(a). The prototype has been manufactured with a rapid prototyping machine (Project HD-3000 Plus, 3D Systems). The stiffness sensor consists of a support structure, two linear modules connected to two spheres, a cap and two steel springs of different dimensions and elasticity (see Figure 4.3(a)). The smallest spring has an outer diameter of 12.19 mm, a wire diameter of 0.51 mm and an elastic constant of 40 $\frac{\text{N}}{\text{m}}$; the other spring has an outer diameter of 16.76 mm, a wire diameter of 0.74 mm and an elastic constant of 190 $\frac{\text{N}}{\text{m}}$. Both springs are made of SS316 steel which is MR-compatible. These springs are commercially available from Lee Spring Company and are enclosed in a hollow cylindrical support structure

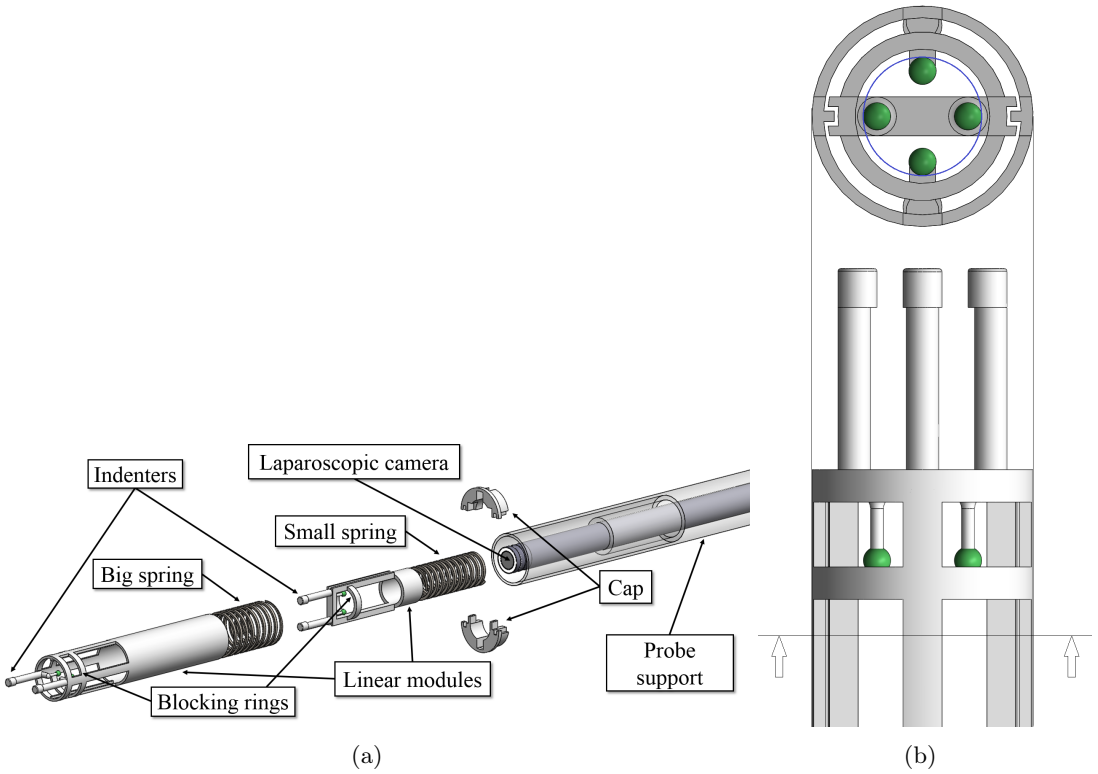

FIGURE 4.3: CAD Drawing of the Vision-based Stiffness sensor: (a) Exploded view and (b) Section view showing the camera Field of View (FOV).

which is mounted on the endoscopic camera. Two linear modules with diameters equivalent to the size of each spring are attached at the end of the springs. The tip of each linear module incorporates a pair of indenters containing two spheres with a diameter of 2 mm. Hence, each pair of indenters is related to one of the springs and able to move independently. A cap fixes the linear guide and the springs inside the support structure. In rest position, the four spheres will be at the same distance from the camera lens. The spheres are symmetrically arranged and have the same offset to the centre of the image plane as shown in Figure 4.3(b). The maximum indentation depth is 18 mm for this prototype. Nevertheless, the sensing range and resolution can be customised by changing the embedded springs or the distance between the camera and the spheres. The diameter of the camera embedded with the sensory system is 19.5 mm. The size of the sensor can easily be reduced to 15 mm or less by using either a different material, for example medical steel, or customised springs or by using an endoscopic camera of a small diameter. Hence, this device is compatible with minimally invasive interventions.

4.4 Vision-based Stiffness Sensor: Image Processing Algorithm

The image processing algorithm presented in Chapter 3.3 has been modified and used here to track the spherical features in the endoscopic camera image. In order to minimise errors in the computation of the radii of the spheres, here the image has been subdivided into four Regions of Interest (ROIs). In each of the ROIs, tracking of the spheres is performed as shown in Figure 4.4. The tracking algorithm is robust to occlusions and small reflections due to disturbing lighting (specularity). This is demonstrated in ROI 4 where the orange circle shows the successful detection of the sphere. The spherical feature in ROI 1 is detected even if specularity occurs. This algorithm allows accurate computing of the radius of the spherical features. The variation of the spherical feature's radius, thus their changing dimensions, will be used to characterise the stiffness properties of phantom tissue. The interaction force applied by each linear model is computed using the method presented in Chapter 3.2.2. Hence, the stiffness of the probed soft tissue is estimated as function of the relative force between the two springs, thus as function of the relative distance between the two linear modules. The sensor's structure allows the sliding of the module only along the axis which is perpendicular to the camera, thus the variation of the spherical feature's radius in the image can be related to the its distance to the camera lens. The model derived in Chapter 3.4 assumes that the sphere lies and moves only along the optical axis. In the new prototype presented here, there is an offset between the position of the spheres and the camera's centre, thus the spheres need to be projected onto the optical axis. If x identifies the distance between the camera's centre and the projection of the sphere's position on the optical axis, h the distance between the sphere and the optical axis, and p the line between the sphere's centre and its projection

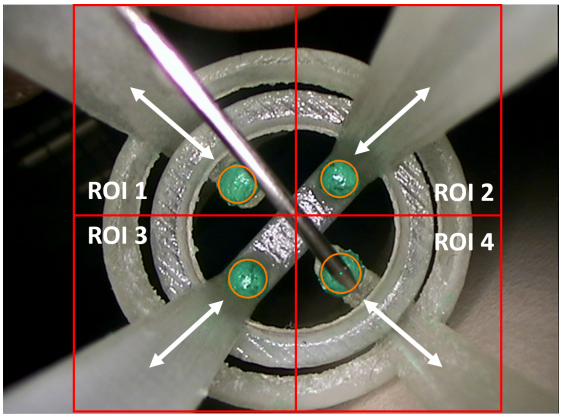

FIGURE 4.4: 4 Regions of Interest (ROIs). The white arrows represent the possible direction of movement of each detected sphere (orange). In ROI 1, light reflection occurred and the sphere is partially occluded. ROI 4 shows that the algorithm can detect the sphere even in the case of 50% of occlusion.

on the image plane that passes through the camera centre, it is possible to express Δx in function of h and p which yields:

$$\Delta x = x_0 - x_1 = x_0 - \sqrt{p_1^2 - h^2}. \tag{4.1}$$

In Equation 4.1, x_0 and h represent the projection of the spheres onto the optical axis at rest condition. These two parameters are known and chosen at the design. The sensor's structure creates geometrical constraints, thus p_1 can be expressed as function of the sphere's radius:

$$p_1 = \frac{r_0}{r} p_0. \tag{4.2}$$

If the response is linear, Equation 4.1 can be used in Hooke's law to model the contact force generated by each indenter, so that:

$$F(r) = K\Delta x(r) = K\left(x_0 - \sqrt{\frac{r_0^2}{r^2}p_0^2 - h^2}\right). \tag{4.3}$$

Here, K represents the spring constant. The returned force value depends on the design of the sensor and the size of the visual feature, i.e. the initial radius r_0 and projection of the feature-camera distance x_0 on the optical axis. In addition, the sphere's radius can be substituted with other geometrical parameters making its validation independent of the visual features shape. Knowing the elastic constant of the two springs embedded in the sensor, K_1 and K_2 respectively, the soft tissue stiffness can be computed as the

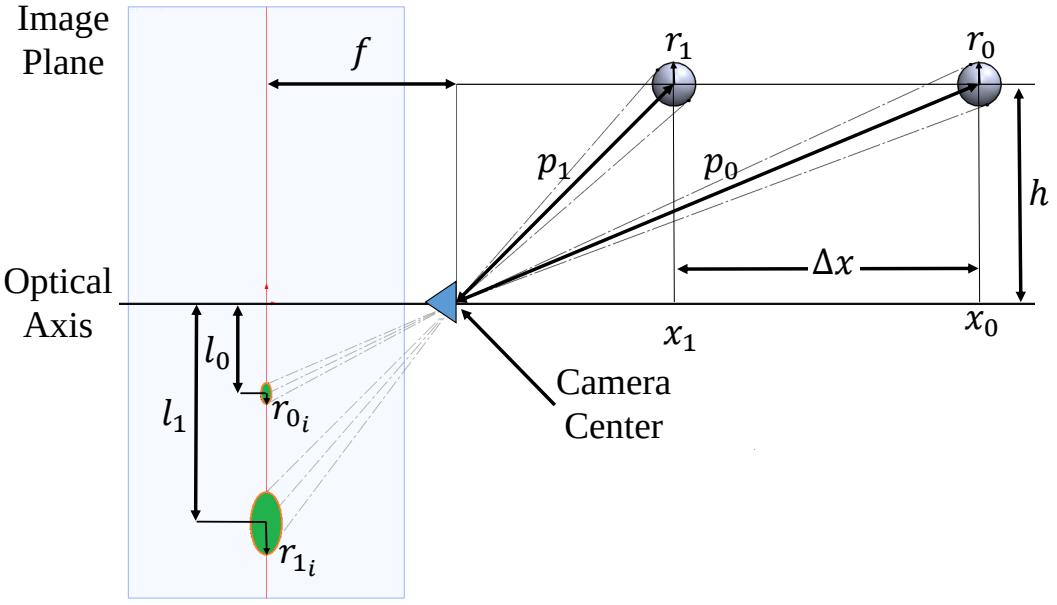

FIGURE 4.5: Operating optical principle. The projection of the sphere at distance p_0 from the camera centre is smaller than the projection of the sphere at distance p_1. The focal length f is the distance between the camera centre and the image plane.

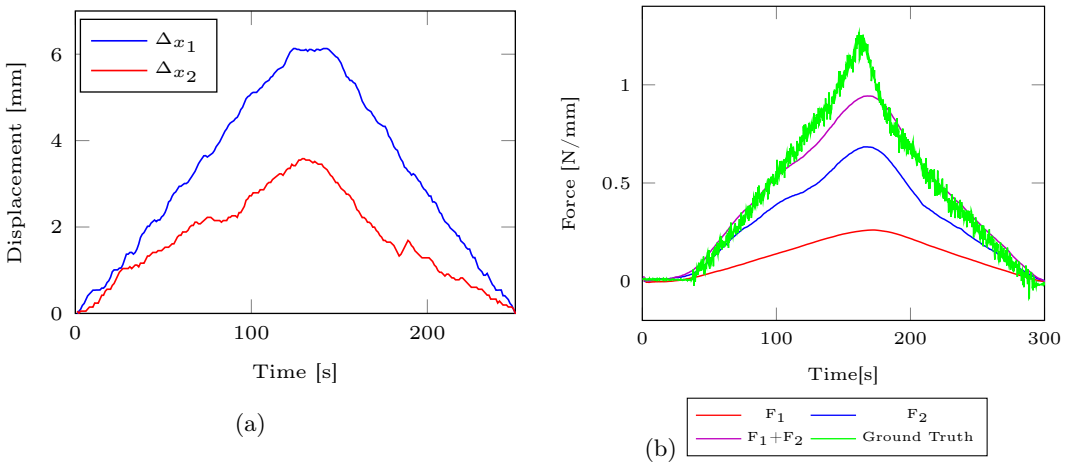

FIGURE 4.6: Experimental Results. (a) and (b) The pattern of (Δx_1) and (Δx_2) displacements for forward and backward motion and the recorded forces, (F_1) and (F_2), are represented in blue and red respectively. In (b) the sum of the forces, F_1 and F_2, is compared with a benchmarking, illustrated in green.

relative difference of the forces generated by each spring, thus:

$$K_s = \frac{K_1(x_{01} - \sqrt{p_{11}^2 - h^2}) - K_2(x_{02} - \sqrt{p_{12}^2 - h^2})}{\Delta s_1 - \Delta s_2} = \frac{(K_1 \Delta x_1 - K_2 \Delta x_2)}{\Delta d}. \quad (4.4)$$

In Equation 4.4 the variable x_{01}, p_{11}, x_{02}, p_{12} represent the mean values of x_0 and p_1 associated to the pairs of spheres embedded in each linear module.

4.5 Experimental Results

The vision-based stiffness sensor was used to palpate silicon phantoms of different elasticities and to evaluate their stiffness. During the experimental tests, the silicon was placed on top of an ATI Nano 17 F/T sensor (used as ground truth) and moved towards the sensing device using a linear guide. Endoscopic images were processed in real time and used to estimate the forces applied by each spring. The force obtained from the benchmarking sensor is the sum of the two forces computed with our model. Hence, the stiffness of the tissue can be measured by considering the ratio between the relative forces and the relative displacement as expressed in equation 4.4. The relative displacement, Δd, is the difference between the projection of the spheres' radius onto the optical axis. The value of Δd increases with the softness of the palpated tissues as a result of considerable displacement between the coupled features. The stiffness of four silicon phantoms was estimated though stress tests with a benchmarking force sensor. The values obtained were compared to the real-time stiffness values computed by using Equation 4.4. Figure 4.6(a) shows the linear trends Δx for the soft spring (Δx_1) and

Stiffness material (N/m)	Computed Stiffness (N/m)	Accuracy
0.08	0.08	99%
0.64	0.61	96%
1.89	1.83	96%
2.23	2.14	95%
∞	(division by 0) $\rightarrow$ undefined	100%

TABLE 4.1: Experimental Results: The stiffness of the silicon phantom measured by a benchmarking sensor and with Equation 4.4 are compared to prove the accuracy of the proposed model.

the stiffer (Δx_2) during a forward (indentation) and backward movement of the linear guide. The displacement Δx increases with time in the forward motion because of the elasticity difference of the springs and decreases with the backward motion. The relative forces are compared with a benchmarking in Figure 4.6 (b).
The experimental results evidence the high accuracy of the vision-based stiffness sensor. However, the accuracy decreases with the increasing of the tissue stiffness, as shown in Table 4.1, as a rigid body exhibits infinite stiffness which results in $\Delta d = 0$ in our model due to a null displacement between the coupled features. In this case, the stiffness is undefined as reported in the last column of Table 4.1 .

4.6 Summary

In this chapter, the design and the testing of a novel stiffness sensor mechanism have been presented. The sensor utilizes visual information to compute the stiffness of soft tissue by tracking linear elastic movements of visual features. The advantages of our system are as follows:

1. The evaluation of soft tissue stiffness is based on vision data provided by a surgical endoscopic camera. Since endoscopic cameras are often used in minimally invasive procedures, their visual functionality is enhanced by using the data they acquire for stiffness measurements.

2. The device has a simple mechanical structure that can be miniaturised. Hence, the prototype for endoscopic cameras described here is expected to meet the size limitations of minimally invasive procedures.

3. The sensing range and resolution can be easily modified by adjusting the two springs embedded inside the mechanism. Springs with a lower spring constant enable high force resolution by sacrificing range and vice versa.

4. The sensor's accuracy increases with the softness of the tissue. This feature makes the system most suitable for medical applications.

The limitations and inaccuracies of the sensor are mostly due to friction and the parallel mechanism of the springs. These issues will be addressed in the next chapters.

CHAPTER 5

Multi-directional Stiffness Probe for Medical Diagnosis

During the last decades, researchers have been trying to reproduce the clinician's sense of touch by developing sophisticated sensing devices. However, most of the proposed solutions work only if the orientation of the sensor does not change during the procedure. This limitation prevents the use of these devices in real applications. To overcome the shortcomings of current devices, the stiffness sensing principle derived in this thesis has been used to realise a multi-directional stiffness sensing probe for medical palpation. This chapter presents the design of the device, the modelling and the experimental results.

5.1 Introduction

Nowadays, there is a growing demand for kinaesthetic displays in medicine, robotics and other fields of engineering and scientific research, as well as in medical training and rehabilitation, sport, games and entertainment [121]. During the last two decades, researchers have developed several instruments able to mimic the traditional manual palpation techniques; many experimental and theoretical papers have been published and a number of patents have been filed reflecting these advances [122]. Kinaesthetic devices usually provide information about contact with end-effectors, but they should not exclude other components of the haptic sense, such as the reflected forces and displacements.

Many medical applications focus on assessing tissue elasticity because of the diagnostic information it provides. Nowadays, the mechanical properties of soft tissue can be evaluated by combining imaging, elastography and computational modelling [123]. Computer Tomography (CT), Ultrasound Imaging (US) and Magnetic Resonance Imaging (MRI) are advanced and sophisticated technologies used for soft tissue characterisation [124] [125].

In Chapter 3.4, a uni-axial vision-based force sensor device has been presented. The sensing principle is based on the tracking of the movements of a feature in an image which are correlated to the compression of a spring. In Chapter 4 the same principle has been used in order to estimate soft tissue stiffness in minimally invasive procedures. In this chapter, multi-directional capabilities are added to the sensing mechanism. The new sensor is shown in Figure 5.1. Four springs, three of which have the same spring constant, are embedded in the sensor's structure and related to four indenters. The

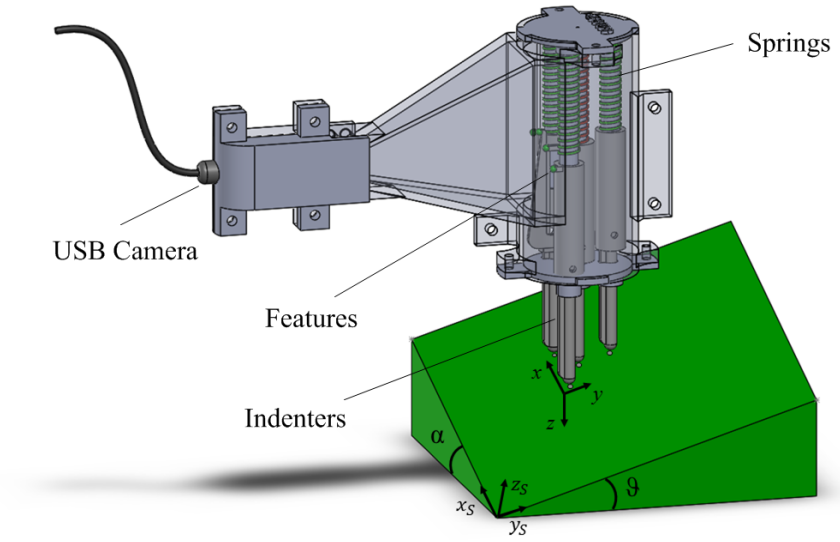

FIGURE 5.1: Multi-directional stiffness probe in contact with a soft surface. The pan and tilt angles between the sensor and the soft object are α and θ respectively.

indentation of the soft tissues results in the sliding of the indenters which will compress the related springs. The compression of the springs is captured by the camera and used to evaluate the stiffness. The physical relation between the three equal springs allows the definition of the contact plane between the stiffness probe and the soft surface, hence, the measurement of the approaching pan and tilt angles.

5.2 Multi-directional Stiffness Sensing Principle

In Chapter 2 the literature on diagnostic devices for medical applications has been reviewed. Most of the proposed solutions can measure soft tissue properties only if the device is indented perpendicularly to the soft surface. Hence, errors and inaccuracies arise if the orientation of the sensor changes during the procedure. In Chapter 4, an innovative vision-based stiffness sensor was developed and tested. Experimental results showed that the sensor can evaluate the stiffness of soft tissues with high accuracy. However, it works only if its orientation does not change while indenting the surface. This limitation has been solved by enclosing in the sensor's structure a triple of elastic elements with the same elasticity. The palpation probe contains four elastic elements, i.e. four springs, three with the same elastic constant and one stiffer. A drawing of the

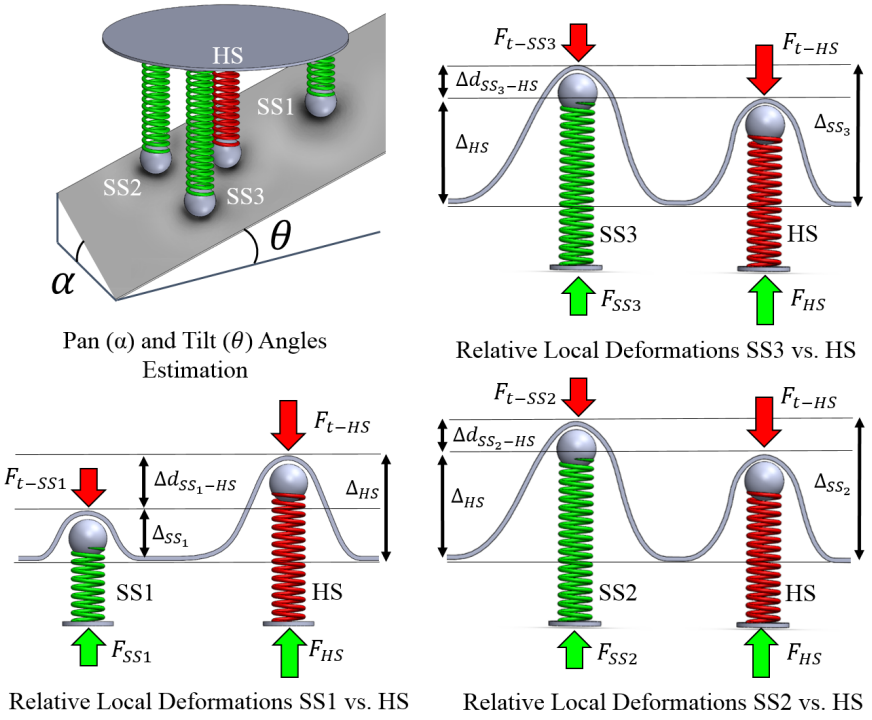

FIGURE 5.2: Multi-directional stiffness sensing principle. Contact between the soft surface and the elastic elements showing the interacting forces and the differential force between the elastic element with higher stiffness (HS) and the three elements with softer stiffness(SS1, SS2, SS3).

sensor interacting with a soft object is shown in 5.1. If the sensor is pushed perpendicularly on a soft object, the elastic elements presenting the same elasticity will exhibit the same compression. However, if the approaching direction is not perpendicular to the soft surface, the springs will exhibit different compressions. Consequently, the sliding length of each indenter will be different. The position of the three elastic elements in the 3D space identify a plane which is used to evaluate the orientation of the probe during the indentation procedure. Moreover, the three elastic elements with a lower elastic constant are displaced more than the stiffer one. This difference in movements is used to measure the soft tissues' stiffness. A mathematical model evaluates the value of the stiffness by considering the orientation of the probe during the interaction. A schematic representation of the sensing principle is shown in Figure 5.2.

5.3 Multi-directional Stiffness Probe Design

The hand-held stiffness probe is composed of four indenters, each connected to a spring, a spherical feature, and a standard USB camera, and tightly assembled in a 3D printed shell. Exploded and assembled views of the stiffness sensor are shown in Figure 5.3. The USB camera has an outer diameter of 7 mm, a resolution of 640x480 and a frame rate of 30 $frames/s$. The stiffness probe has been manufactured with a high resolution 3D printer (HD-3000 Plus from 3D System) which has an accuracy of 16 μm along the z-axis

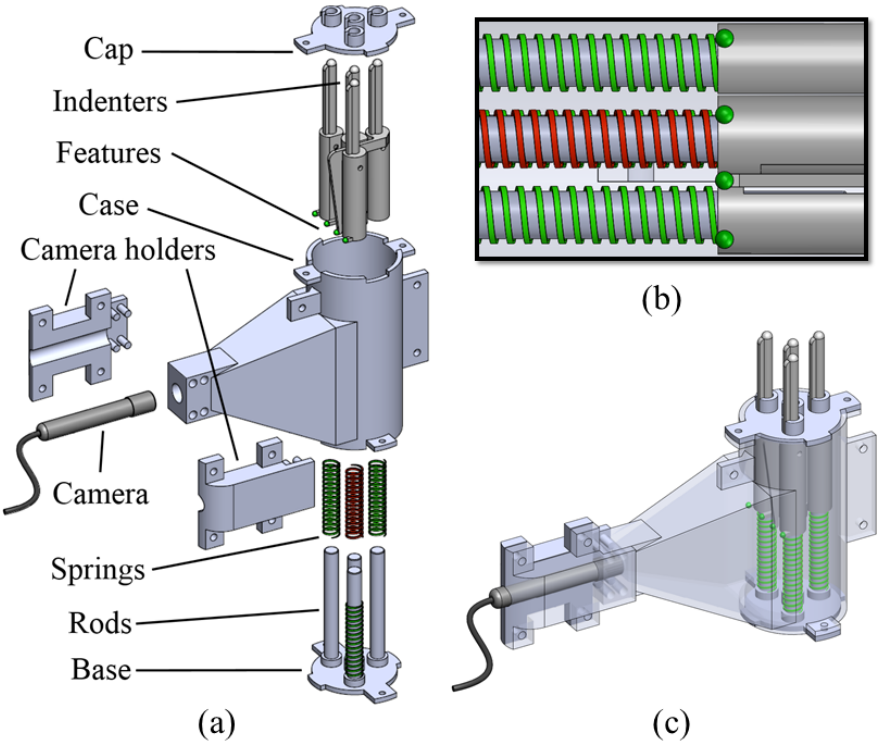

FIGURE 5.3: CAD Drawing of the stiffness probe showing in green the softer springs and in red the stiffer : (a) Exploited View, (b) Camera View and (c) Assembled.

and 42 μm along the x- and y-axes) using acrylonitrile butadiene styrene (ABS) high density material. The springs are made of SS316 steel, a material that is suitable for medical applications. Hence, the fabrication costs are relatively low. Three of the springs have the same spring constant of 0.05 N/mm; the fourth has been chosen to be stiffer and has a spring constant of 0.25 N/mm. The softer springs are placed on the vertices of a triangle and the stiffer one on its barycentre, as in Figure 5.3(a). The movements of each indenter and its associated rods depend on the related spring, hence the three indenters related to the same spring present a softer behaviour when compared to the one related to the fourth indenter. During interaction with a soft object, the indenters slide over their rods leading to a compression or decompression of the corresponding spring that in turn generates movement in the related spherical features. The analogy between the movements of the spring, the related indenter and the spherical feature is regulated by the elasticity of the springs: i.e. contact with external soft surfaces will produce a bigger compression of the three softer springs in respect to the stiffer one. Consequently, the indenters associated to the softer spring will slide more than the indenter associated to the stiffer spring. This will generate different displacements of the spherical features along the horizontal axis.

5.4 Refinement of the Image Processing

The image processing algorithm presented in Chapter 3.3 has been modified and adapted for the new sensor. The design of the palpation device, shown in Figure 5.3(a), allows the four indenters to move only along one direction. Hence, the sliding of the indenters causes the compression or decompression of the relative spring, which is reflected in horizontal movements of the spherical features in the images. The image has been subdivided into four Regions of Interest (ROIs). Each ROI is associated to one of the spherical features and captures its full range of motion. The image processing algorithm uses the HSV colour channel to detect the spherical features. Image moments and Kalman filtering are employed to robustly track the spherical feature's centroids in the associated ROI. In order to create a generic image processing solution and for that solution to be easily adapted to different sensor designs, the algorithm is individually executed on each feature in the corresponding ROI. In the next sections, each stage of the image processing algorithm will be explained in detail. The overall method is presented in Algorithm 1.

5.4.1 Computation of the Feature's Centroids using the Image Moment

Image moment is used to describe the image's properties, i.e. area, thickness, orientation, skewness, etc. These properties can be used to identify shapes in the image. The general form for calculating the moment of a 2D continuous function $f(x, y)$ of order $(r+s)$ with $r, s \in \mathbb{N}$ can be expressed as:

$$\int_{-\infty}^{+\infty} \int_{-\infty}^{+\infty} x^r y^s f(x, y) \mathrm{d}x \mathrm{d}y. \tag{5.1}$$

The discrete form of Equation 5.1 can be used for the image processing algorithm. Given a grayscale image of width W, height H and pixels intensities I(x,y), the raw image moments can be defined as:

$$M_{i,j} = \sum_{x=1}^{W} \sum_{y=1}^{H} x^i y^j \;\; I(x, y). \tag{5.2}$$

For $i = j = 0$ Equation 5.2 can be simplified down to:

$$M_{0,0} = \sum I(x, y). \tag{5.3}$$

A grayscale image is always going to be either one or zero, thus Equation 5.3 simply counts all the pixels in the image that have value one; therefore, it calculates the area of a binary image. From Equation 5.3 the position of the centroid, (C_x, C_y) can be expressed as:

$$C_x = \frac{M_{10}}{M_{00}} \quad C_y = \frac{M_{01}}{M_{00}}. \tag{5.4}$$

5.4.2 Robust Tracking: Kalman Filter on the Image Centroids

The Kalman filter is used to track the horizontal position of each centroid in the related ROI. The filter is applied to each new centroid and computed using Equation 5.4. For more details on the implementation of the filter, please refer to Appendix B. Based on empirical evaluation, the filter parameters have been initialised with the following values: process noise $q_0 = 0.09$, sensor noise $r_0 = 4$ and initial estimated error $p_0 = 6$. The initial horizontal position of the centroids, C_{xj_0} in the correspondent RoI_j is computed in the

Algorithm 1 Image Processing

Input: current Image I_i, camera resolution cr
Output: current z coordinate of the indenters

procedure INITIALIZATION
  if I_i is the first image ($I_i = I_0$) **then**
    set $p = p_0$, $r = r_0$ and $q = q_0$
    compute the centroid in every j^{th} RoI:
    $C_{xj_0} = \frac{M_{10}}{M_{00}}$, $C_{yj_0} = \frac{M_{01}}{M_{00}}$
    return $\frac{C_{xj_0}}{cr}$ $(j = 1...4)$
  else
    while there is an image in input I_i **do**
      colour detection of I_i in HSV
      convert I_i in grayscale
      for j=1:4 **do** compute RoI_j
        Kalman filter prediction:
        $\hat{C}^-_{xj_i} = \hat{C}^-_{xj_{i-1}}$
        $p^-_{xj_i} = p_{xj_{i-1}} + \mathrm{q}$
        Kalman filter update:
        $k_{xj_i} = p^-_{xj_i}/(p^-_{xj_i} + r)$
        $\hat{C}_{xj_i} = \hat{C}^-_{xj_i} + k_{xj_i} * (M_{10}/M_{00} - \hat{C}^-_{xj_i})$
        $p_{xj_i} = (1 - k_{xj_i}) * p^-_{xj_i}$
        return $\hat{C}_{xj_i}/cr$
      end for
    end while
    goto 4
  end if
end procedure

first image I_0 using the image moments. After the prediction step, the state of the filter

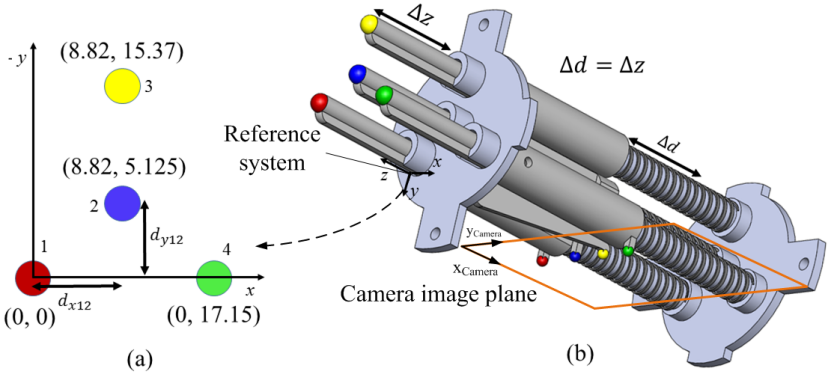

FIGURE 5.4: Hand-held stiffness probe: (a) is the frontal view of the sensor showing the position of the indenters (mm) expressed in the local reference system; the indenters coupled to the corresponding spherical features are shown in (b). Each pair is represented by the same colour. The interaction of an indenter with the surface of a soft object results in a displacement of Δz; the corresponding sphere moves by the same quantity, but appears in the camera images as a movement along the x-axis, hence, Δx.

is defined using p, q, C_{xj_i} as shown in Algorithm 1.

5.4.3 Spring-Indenter-Features Relation

In the designed stiffness probe, the camera is fixed, i.e. its movements are jointly liable with the sensor structure, as shown in Chapter 5.3 . During interaction with an external soft object, the indenter will slide and compress the springs embedded in the sensor's structure. Consequently, the spherical features will move in the camera images. The relation between the 3D movements of the indenters and the movements of the spherical features in the image can be modelled choosing a local reference system on the stiffness probe cap, as shown in Figure 5.4(b). The x-z-plane of this system results in being parallel to the image plane, thus, the sliding of the indenters in the local frame will be reflected on the movements of the spherical features in the image as shown in Figure 5.4(a): when the indenters move towards the origin of the local reference frame decreasing their z-position, the spherical features will move away from the origin of the image plane increasing their x-position. The resolution of the sensor is 12.7 $pixels/mm$, i.e. when the indenter moves by 1 mm, the position of the correspondent centroid changes by 12.7 $pixels$. The relation between the compression of the springs, the movements of the indenters and the movements of the spherical features is used to show the connection between the position of the spherical features' centroids and the indentation depth as shown in Figure 5.4(b).

5.5 Methodology

5.5.1 Modelling Soft Tissue Properties

The mapping between the position of the spherical features in the image and the position of the indenters is used to characterise the interaction between the stiffness probe and the examined soft tissue. The sliding motion of the three indenters placed on the vertices of the triangle makes use of the same type of spring, while the indenter in the centre is connected to a spring with a higher spring constant, thus it moves less during the interaction with the soft tissue. The stiffness of the surface in contact can be computed using the forces applied by the harder indenter placed in the barycentre of the triangle and the three "softer" indenters [126].

Seven parameters are sufficient to fully characterise a palpation procedure with the proposed stiffness probe: the stiffness of the soft tissue, K_t, the four palpation depths of the soft tissue caused by the interaction with the four indenters, the pan angle θ and the tilt angle α as shown in Figure 5.1. A system of non-linear equations, $F(\mathbf{x}) = 0$, can be

used to express the relation between the seven unknown parameters, where:

$$F(\mathbf{x}) = \begin{cases} dx_1 \times K_s - K_t \times dt_1 \\ dx_2 \times K_h - K_t \times dt_2 \\ dx_3 \times K_s - K_t \times dt_3 \\ dx_4 \times K_s - K_t \times dt_4 \\ dx_2 + dt_2 - dx_1 - dt_1 + \tan(\theta) \times d_{12x} + \tan(\alpha) \times d_{12y} \\ dx_3 + dt_3 - dx_1 - dt_1 + \tan(\theta) \times d_{13x} + \tan(\alpha) \times d_{13y} \\ dx_4 + dt_4 - dx_1 - dt_1 + \tan(\theta) \times d_{14x} + \tan(\alpha) \times d_{14y} \end{cases} \tag{5.5}$$

In Equation (5.5), dx_i $(i = 1...4)$ represents the position of the i^{th} sphere, d_{ijx} and d_{ijy} $(i, j = 1...4)$ with $i \neq j$ represents the distance between the i^{th} and j^{th} sphere in the reference system of the sensor. K_s and K_h are the known spring constants of the soft and hard springs, respectively. The seven unknown parameters are: the pan angle θ, the tilt angle α, the displacement of the soft tissue in the points of contact, dt_i with $(i = 1...4)$ and the stiffness of the soft surface K_t, and are collected in the vector of the problem's unknowns, $\mathbf{x} = [K_t, dt_1, dt_2, dt_3, dt_4, \alpha, \theta]^T$. Solving the system of nonlinear equations $F(\mathbf{x})$, in Equations (5.5), involves finding a solution such that every equation in the nonlinear system is equal to zero, i.e. find a vector $\mathbf{x}^\star$ such that $F(\mathbf{x}^\star) = 0$. The major algorithms used for solving nonlinear equations proceed by minimizing a sum of squares of the nonlinear equations, which is equivalent to a unconstrained nonlinear least squares problem.

5.5.2 Soft Tissue Characterisation

The Levenberg-Marquardt algorithm (LMA) is applied here to solve Equation (5.5). This algorithm is an iterative optimisation technique for solving nonlinear systems of equations and least squares problems. To solve the convergence issues of the iterative process, the LMA combines the advantages of the gradient-descent and the Gaussian-Newton methods [127]. The LMA provides the best compromises between complexity, stability and speed. A detailed analysis of the LMA is presented in Appendix C. The optimization method is used to find at each iteration the update rule of the vector $\mathbf{x}$:

$$\mathbf{x}_{k+1} = \mathbf{x}_k - (H(\mathbf{x}_k) + \lambda_k diag(H(\mathbf{x}_k)))^\dagger J(\mathbf{x}_k)^T F(\mathbf{x}_k), \tag{5.6}$$

where $J(\mathbf{x}_k)$ is the Jacobian matrix of $F(\mathbf{x})$ evaluated at $\mathbf{x}_k$, $H(\mathbf{x}_k) \approx J(\mathbf{x}_k)^T J(\mathbf{x}_k)$ is an approximation of the Hessian matrix and λ_k represents the non-negative damping factor that is adjusted at each iteration to interpolate between the gradient descent and the Newton's method. Using high values for λ favours gradient descent, whereas using lower values favours Newton's method. The damping factor λ is increased by a factor of

Algorithm 2 Iterative procedure solving Equations (5.5): LMA

Input:
F, the cost function
$\mathbf{x}_0$, an initial solution
Output:
$\mathbf{x}^\star$, a local minimum of F

Begin
  $k \leftarrow 100$
  $\lambda \leftarrow 20$
  $\varepsilon \leftarrow 0.0001$
  $\mu \leftarrow 10$
  $\mathbf{x}_k \leftarrow \mathbf{x}_0$
  while $g > \varepsilon$ **and** $k < k_{max}$ **do**
    Find λ such that $(H(\mathbf{x}_k) + \lambda_k diag(H(\mathbf{x}_k)))^\dagger = J(\mathbf{x}_k)^T F(\mathbf{x}_k)$
    $\mathbf{x}_{k+1} \leftarrow \mathbf{x}_k + \lambda_k$
    if $F(\mathbf{x}_{k+1}) < F(\mathbf{x}_k)$ **then**
      $\mathbf{x}_k \leftarrow \mathbf{x}_{k+1}$
      $\lambda \leftarrow \frac{\lambda}{\mu}$
    else
      $\lambda \leftarrow \lambda\mu$
    end if
    $k \leftarrow k + 1$
  end while
  return $\mathbf{x}_k$
End

μ, if $\|F(\mathbf{x}_{k+1})\|$ is greater than $\|F(\mathbf{x}_k)\|$ and decreases by a factor of μ otherwise. The proposed method converges when the cost function, $g = \|F(\mathbf{x}_{k+1}) - F(\mathbf{x}_k)\|$, is less than a chosen threshold ε. Then, the current vector $\mathbf{x}_{k+1}$ is returned as the best-fit solution $\mathbf{x}^*$.

In order to be able to find a solution to the unknown parameters and to compute the stiffness in real-time, in the implemented algorithm, the threshold ε and the maximum number of iterations k_{max} are setted to 0.0001 and 100, respectively. The final threshold value was found through a trial-and-error approach. Using this threshold, the algorithm typically needs less than seven iterations to find a solution with high accuracy. The value of μ used to adjust the damping parameter at each iteration is equal to 10. Algorithm 2 illustrates the procedure used to solve the system presented in Equation (5.5) .

5.6 Experimental Results

Two different experimental scenarios were used in order to analyse the performance of the proposed stiffness probe. In the first setup, artificial stiffness samples of known stiffness have been used in order to evaluate the accuracy of the proposed system in computing the stiffness of the springs embedded in the samples. In the second scenario, the hand-held device has been used to manually palpate silicone phantoms presenting different

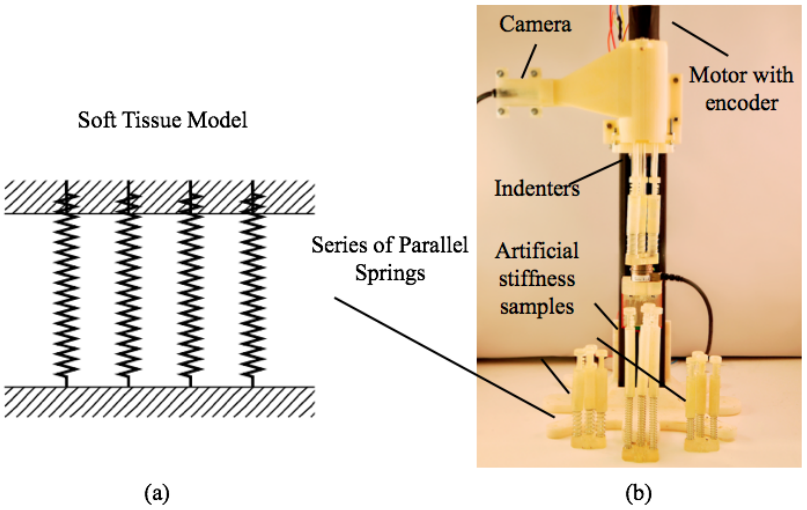

FIGURE 5.5: Evaluation test setup: (a) Soft tissue model. Each artificial stiffness sample behaves as a series of parallel springs. (b) The experimental setup. Four different artificial stiffness samples are used to mimic soft tissue. Four identical springs are mounted on rods in parallel and are fixed on a linear module. The samples are pushed against the device and the stiffness of the samples is computed in real-time.

elasticity and evaluate the ability of the system in distinguishing materials that present different degrees of stiffness.

5.6.1 Evaluation Tests with Stiffness Samples

The linear elastic model was used here to mimic human soft tissue. In this model the tissue is considered as a homogeneous, linear elastic material; the stress/strain relationship is assumed to be linear too. Although biological tissues are much more complex, this behaviour was found coherent for a relative strain under 10 to 15% [115]. Under this assumption the material properties can be described using Hooke's law. The complexity of the model depends on the deformation range: under geometrical linearity, (i.e. small deformations), the Green-Lagrange equation that relates stress and strain tensor is linearised by neglecting the second order term [128]. Therefore, in this model a series of parallel springs [129] can be used to represent the soft tissue.

Artificial stiffness samples, each embedding four parallel springs in series, have been designed. Each sample contains four rods with self-centring shaped heads and their movements are related to four linear springs with identical spring constants. During the experiments, the stiffness probe was fixed on a motorised linear module and the artificial stiffness samples were moved towards the indenters as shown in Figure 5.5 (b). In all the experiments, the motor was moving by $18mm$; forces, displacements and stiffness were computed using the image tracking algorithm and solving Equation 5.5. Table **??** summarises the results obtained for the four artificial stiffness samples. As the stiffness

K	$\bar{K}$	σ	RMSE	Accuracy
0.29	0.29	0.01	0.01	99.23%
0.37	0.38	0.02	0.02	98.87%
0.62	0.65	0.03	0.05	96.54%
0.63	0.66	0.01	0.04	96.26%

TABLE 5.1: Summary of the evaluation tests performed using the test rig shown in Figure 5.5 (b). K represents the real stiffness of the springs used for the test, $\bar{K}$ is the mean of the stiffness computed solving Equation (5.5), σ and RMSE are the standard deviation and the root mean square, respectively. The last column represents the percentage of accuracy of the proposed probe in computing the stiffness of the artificial stiffness samples.

of the springs embedded in the samples increases so does the measurement error. When interacting with "stiff" objects, the difference in displacement between the "softer" and the "stiffer" springs embedded in the hand-held device decreases reducing the accuracy of the estimation. Thus, the computation of the stiffness depends on the resolution of the camera which is used to track the spherical features. The resolution of the stiffness sensor is 12.7 $pixels/mm$, i.e. if the indenter moves by 1mm, the corresponding centroid in the image will move by 12.7 pixels.

The experimental results and the stiffness distribution for the four artificial samples are shown in Figure 5.6. The proposed system is able to compute the stiffness of the springs embedded in the lower stiffness sample w i.e. $0.29\,N/mm$ with an accuracy of over 95%.

To evaluate the multi-directional capability of the system, the stiffness probe was manually pushed against the artificial stiffness samples. The experimental results, shown in the Figures 5.7, 5.8, 5.9 and 5.10, demonstrate that the computation of the stiffness does not depend on the orientation at which the device approaches the samples: there is no correlation between the computation of the stiffness and the pan and tilt angles of the probe.

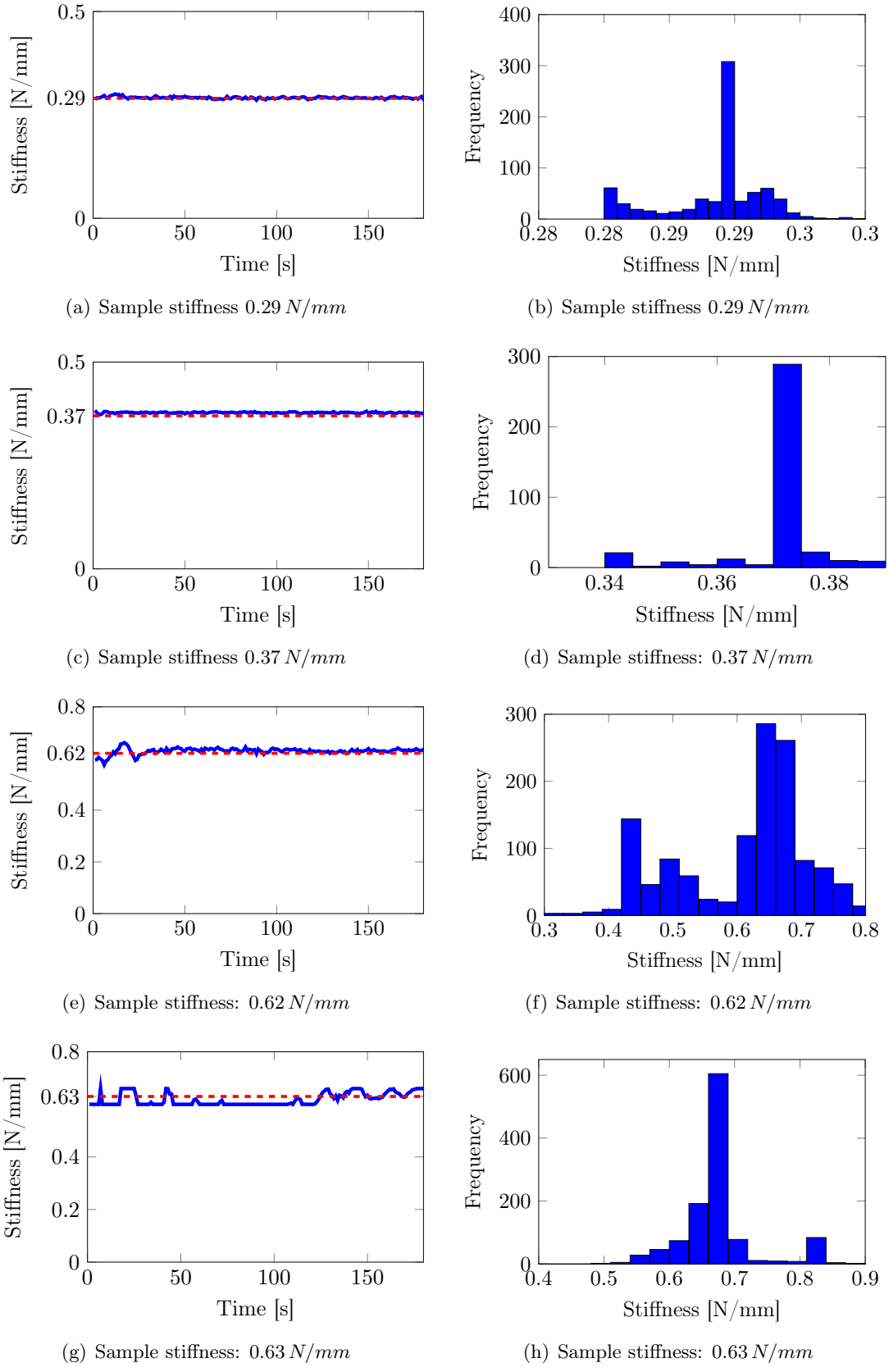

(a) Sample stiffness 0.29 N/mm

(b) Sample stiffness 0.29 N/mm

(c) Sample stiffness 0.37 N/mm

(d) Sample stiffness: 0.37 N/mm

(e) Sample stiffness: 0.62 N/mm

(f) Sample stiffness: 0.62 N/mm

(g) Sample stiffness: 0.63 N/mm

(h) Sample stiffness: 0.63 N/mm

FIGURE 5.6: Evaluation tests results of the artificial stiffness samples. The figures on the left column show the measured stiffness; the distribution of the data for each sample is shown on the right column.

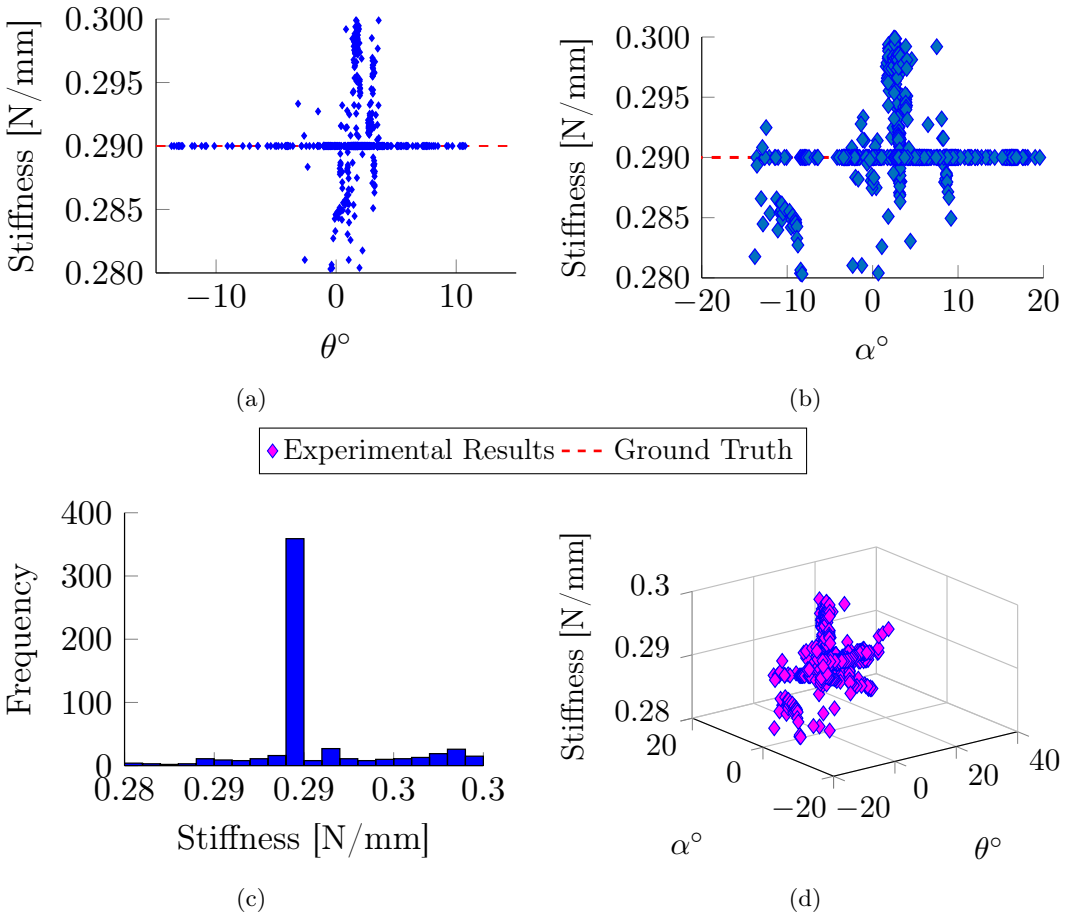

FIGURE 5.7: Manual tests for the artificial stiffness sample with spring constant of $0.29\,N/mm$: Correlation between the measured stiffness and the orientation of the hand-held probe, which is defined by the pan angle θ (a) and the tilt angle α (b). (c) Stiffness distribution of the data during the experiment. (d) The stiffness variation in function of the two angles. The mean of the stiffness and the standard deviation are 0.29 and 0.01, respectively.

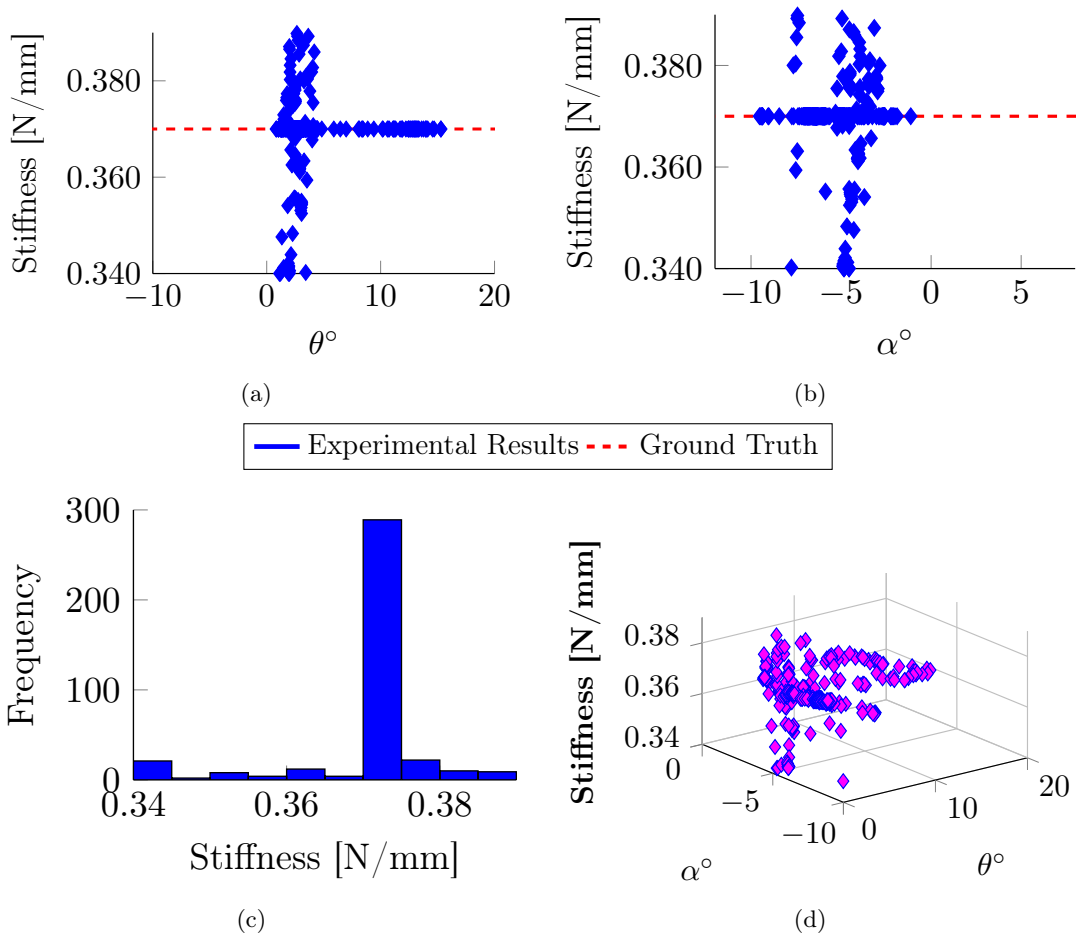

FIGURE 5.8: Manual tests for the artificial stiffness sample with spring constant of $0.37\,N/mm$: Correlation between the measured stiffness and the orientation of the hand-held probe, which is defined by the pan angle θ (a) and the tilt angle α (b). (c) Stiffness distribution of the data during the experiment. (d) The stiffness variation in function of the two angles. The mean of the stiffness and the standard deviation are 0.36 and 0.01, respectively.

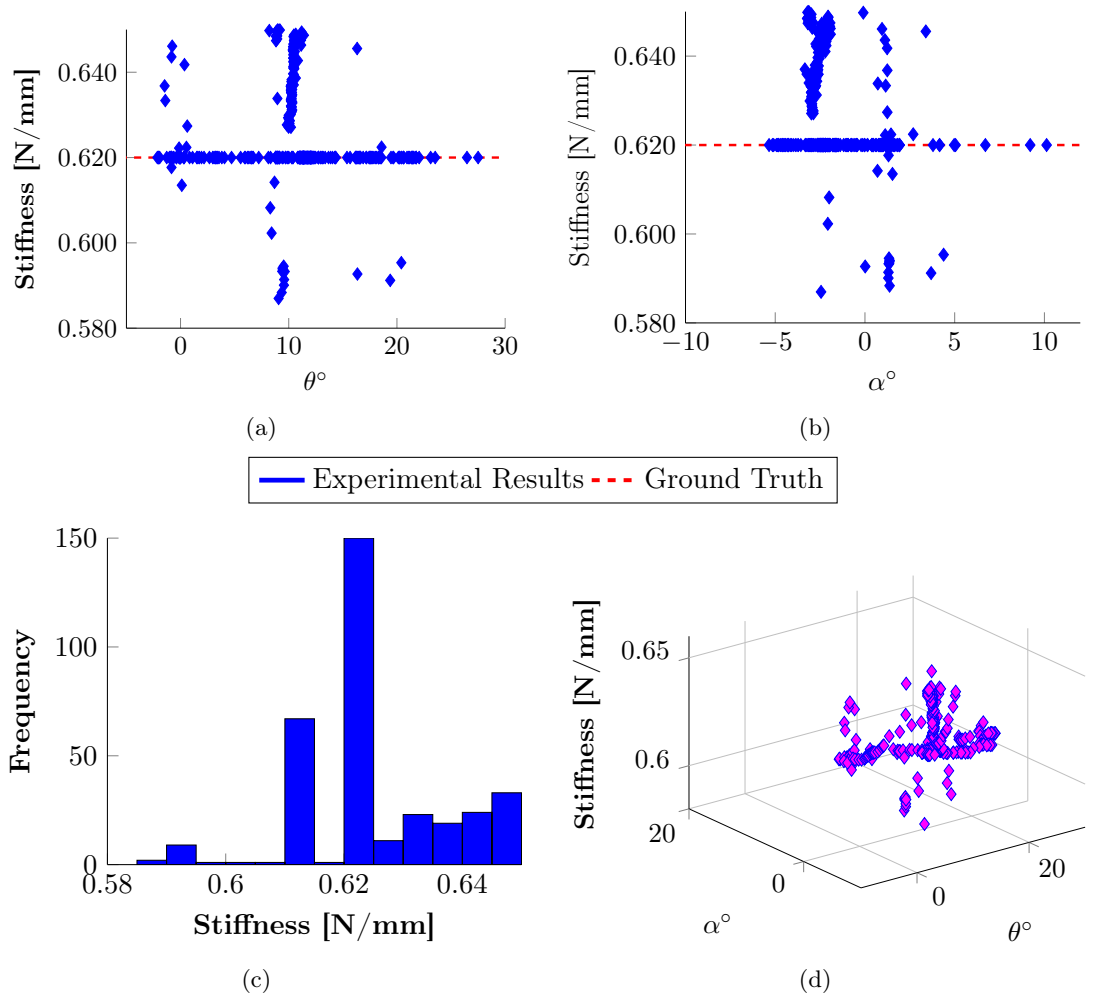

FIGURE 5.9: Manual tests for the artificial stiffness sample with spring constant of $0.62\,N/mm$: Correlation between the measured stiffness and the orientation of the hand-held probe, which is defined by the pan angle θ (a) and the tilt angle α (b). (c) Stiffness distribution of the data during the experiment. (d) The stiffness variation in function of the two angles. The mean of the stiffness and the standard deviation are 0.62 and 0.06, respectively.

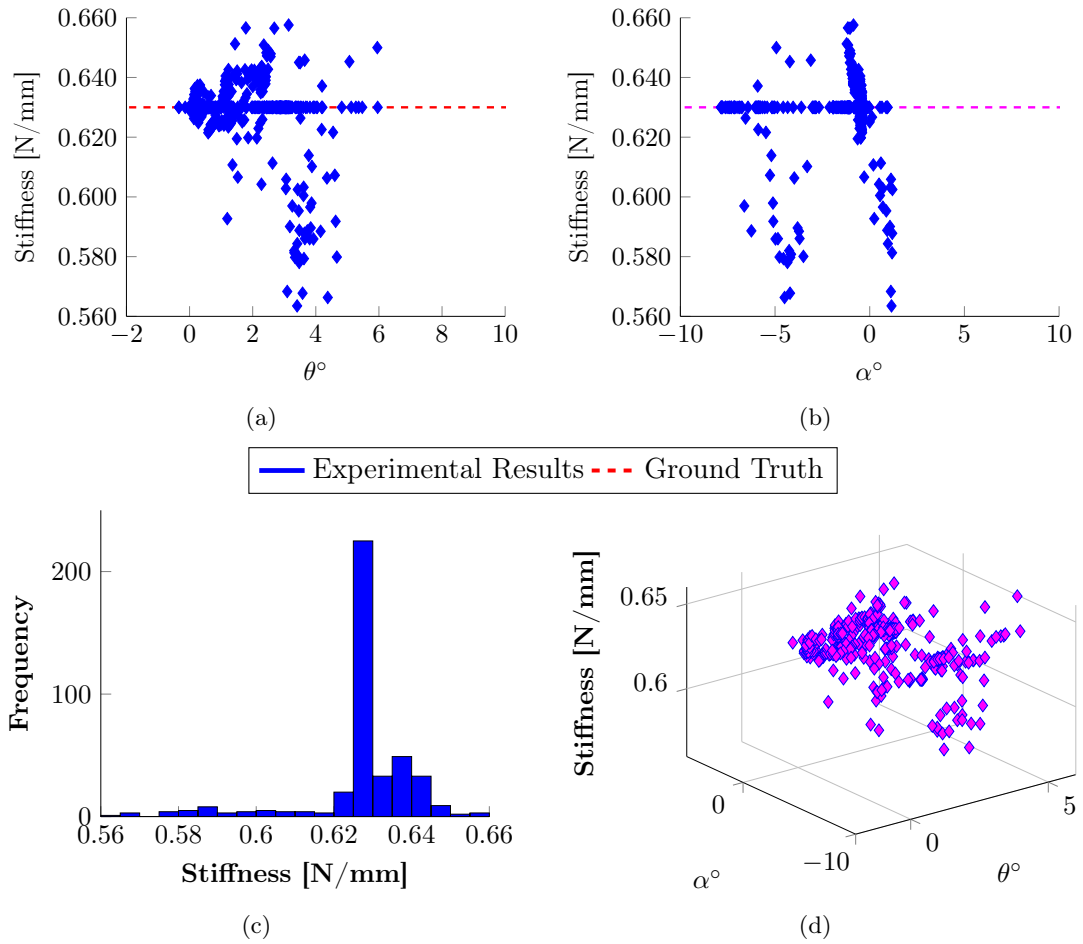

FIGURE 5.10: Manual tests for the artificial stiffness sample with spring constant of $0.63\,N/mm$: Correlation between the measured stiffness and the orientation of the hand-held probe, which is defined by the pan angle θ (a) and the tilt angle α (b). (c) Stiffness distribution of the data during the experiment. (d) The stiffness variation in function of the two angles. The mean of the stiffness and the standard deviation are 0.68 and 0.08, respectively.

5.6.2 Evaluation Test with Silicone Samples

It is shown in section 5.6.1 that the proposed stiffness probe can compute the stiffness of linear elastic materials, i.e. springs, with high accuracy. To further evaluate the ability of the sensor to distinguish materials presenting different degrees of stiffness, the hand-held device was tested using four silicon phantoms with different stiffness values. Silicone is a non-linear elastic material. For small displacements, however, the response is approximately linear [33, 130]. The experimentally tested silicone materials are: Oomoo®30A, Dragon Skin® 20A, Ecoflex®00-50 and Ecoflex®00-10 by Smooth-On. The hardness of plastic is measured by the Shore® test which evaluates the resistance of the materials to indentation. The silicone rubber used belongs to two Shore scales: the A00 scale, which is used for rubbers and gels that is very soft, and the A scale, which measures the hardness of flexible rubbers that ranges from very soft and flexible to hard with almost no flexibility. The Shore hardness is an indirect measure of the stiffness of elastomeric materials, i.e. a low hardness value is correlated to a low stiffness value. Analogously, as the Shore hardness increases so does the stiffness of the materials but this relation is not directly proportional.

The elastic properties of a specimen can be determined by analysing the elastic-plastic contact between the specimen and a spherical indenter. The stiffness of the specimen, which is function of the indentation depth and the elastic modulus of the material, is estimated during the unloading process. If h is the indentation depth generated by the contact between a spherical indenter of radius R and a specimen with elastic modulus E and Poisson ratio v, the load-displacement relation can be expressed as:

$$P = \frac{4}{3}\frac{E}{1-v^2}\sqrt{Rh^3}; \tag{5.7}$$

the unloading stiffness of the specimen is obtained by differentiating this equation with respect to h [131, 132]:

$$S = \frac{dP}{dh} = \frac{2E}{1-v^2}\sqrt{Rh}. \tag{5.8}$$

The value of the stiffness at the maximum depth, h_{max}, is estimated by replacing h with h_{max} in equation 5.8. The tips of the designed stiffness probe can be approximated to spheres with diameter of $0.38mm$. The maximum indentation depth of this prototype is $30mm$. However, this value can be customised by changing the length of the springs and the indenters embedded in the sensor.

During the experimental tests, the hand-held stiffness probe has been used to indent the silicone phantom as shown in Figure 5.11(a). The test results in Figure 5.11(b) show that our sensor is able to successfully distinguish materials with different stiffness levels even if the difference is relatively small as for example when comparing Dragon Skin®20A to

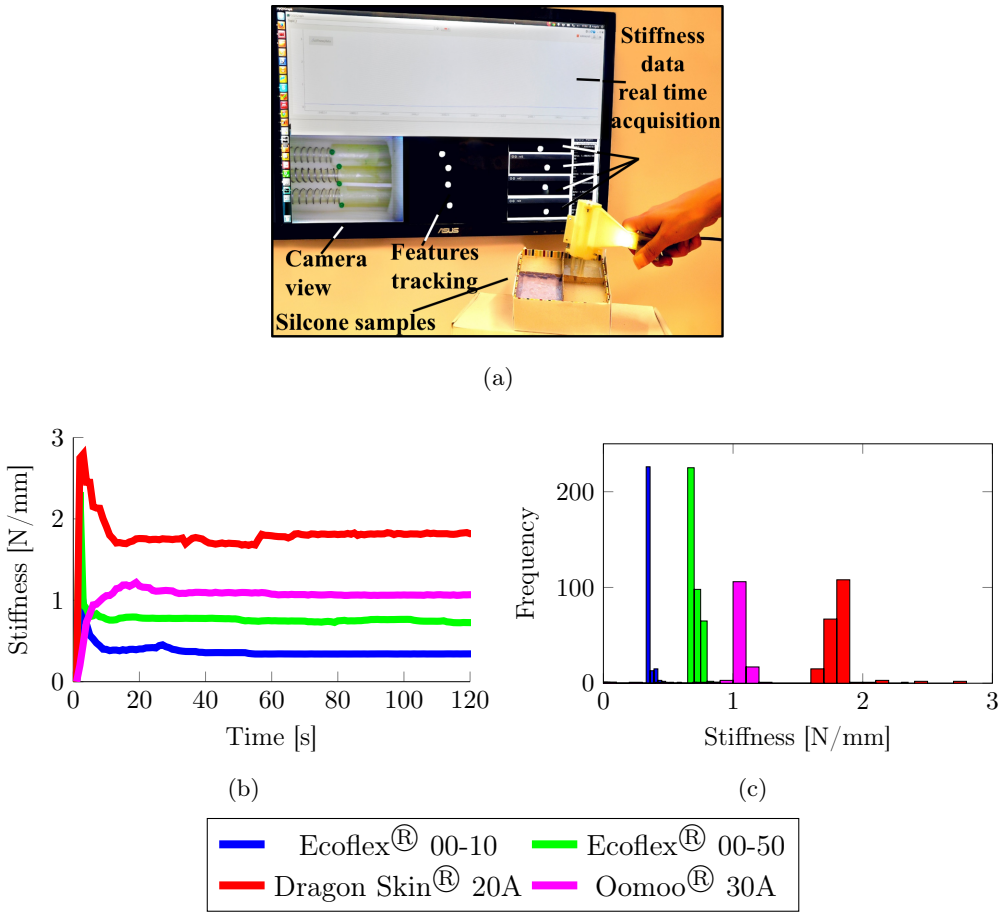

FIGURE 5.11: Evaluation tests with four different types of silicone materials: the real-time image processing and stiffness computation of the probed material are shown in (a); the discrimination between the different stiffness values of the silicone samples is visible in the coloured plot and the histogram presented in (b) and (c), respectively. The four colours in (b) and (c) represent the different stiffness values of the material: the pink colour is associated to the Oomoo®30A, the red to the Dragon Skin® 20A, the green to the Ecoflex®00-50 and the blue to the Ecoflex®00-10.

Oomoo® 30A - a scenario in which manual palpation fails. The values associated to those two materials are represented in red and pink in Figure 5.11(b) and Figure 5.11(c). The stiffness probe fails to distinguish between those two materials in 8% of cases. The elastic properties of the silicone materials used during the tests and the experimental results are shown in Table 5.2. The stiffness value at the maximum indentation depth, $K_{h_{max}}$, which is computed using equation (5.8), represents the benchmarking reference used to evaluate the accuracy of the stiffness values computed by solving Equation (5.5). The error in the measurements increases as the silicone phantom hardness increases. When interacting with hard material, the difference in displacement between the "softer" and the "stiffer" springs embedded in the hand-held device decreases, reducing the accuracy of the estimation. Hence, the computation of the stiffness depends on the resolution of the camera which is used to track the spherical features and the spring embedded in the

Material	$K_{h_{max}}$[N/mm]	$\bar{K}$ [N/mm]	σ	RMSE	%
Ecoflex® 00-10	0.365	0.355	0.063	0.026	96.6
Ecoflex® 00-50	0.657	0.675	0.080	0.029	90
Oomoo® A-30	1.095	1.034	0.197	0.128	76.7
Dragon Skin® A-20	2.190	2.033	0.203	0.202	66.5

TABLE 5.2: Properties of the experimentally tested materials and summary of the evaluation tests performed using the test rig shown in Figure 5.11(a). $K_{h_{max}}$ represents the stiffness computed using Equation (5.8), $\bar{K}$ is the mean of the stiffness computed solving Equation (5.5), σ and RMSE are the standard deviation and the root mean square, respectively. The last column represents the percentage of accuracy of the proposed probe in computing the stiffness of the silicone phantoms.

probe.

5.7 Discussion and Conclusions

In this chapter, the stiffness sensing principle, derived in Chapter 3, has been used to develop a multi-directional stiffness probe for medical palpation. The proposed sensor is able to estimate the stiffness of soft tissues independently of the orientation at which palpation is performed. Experimental results show that the sensory system can successfully distinguish between materials of different stiffness values, thus, it can potentially be used to detect tumours and suspicious masses, which are generally stiffer than the surrounding healthy soft tissues. The working range and resolution of the stiffness probe can be easily customised by replacing the springs embedded in the sensor, changing the distance between the camera and the spherical features or using a camera sensor with different resolution. If used for medical diagnosis, it can help clinicians to obtain valuable information about the presence of a mass inside a soft tissue organ. Simple modification in the design or the use of different fabrication material allow the customisation of the sensor's range and accuracy, which can be tailored according to the desired application. Miniaturised versions of the probe can be integrated in endoscopic cameras [126] and used for diagnosis in minimally invasive scenarios.

CHAPTER 6

Multi-directional Stiffness Sensor for Endoscopic Examination

This chapter presents a preliminary design of a clip-on sensor for endoscopic cameras. The proposed device is used to palpate anatomical areas during medical examination. Multiple cantilever beams are indented into soft tissue. The movements of the cantilevers result in shape variations of the related visual features in the endoscopic camera images. Beams of different elasticity are integrated into the mechanical structure of the sensor enabling the estimation of the stiffness properties of the examined soft tissue by tracking the movements of the features in the image frames. This stiffness sensor is light, cheap, disposable, passive and easy to integrate on the tip of a surgical endoscopic camera. The additional sensing mechanism is very small, increasing only slightly the diameter of the endoscopic camera allowing it to be inserted into the human body through a standard trocar port.

6.1 Introduction

An endoscope is a medical instrument used to examine the interior of a hollow organ or cavity of the body. Endoscopes are like medical telescopes, and unlike other imaging techniques, such as MRI and CT, are inserted directly into the body. Practitioners use endoscopic instruments to inspect a specific part of the body, to diagnose a disease or find the cause of a patient's symptoms. Endoscopes are not only used for diagnostic purposes, but also for treatment or as part of a procedure aiming to prevent future health problems [120, 133]. There are different types of endoscopes of varying lengths and flexibility, each suited to the examination of a specific area of the body; for instance, the abdomen is examined by a laparoscope, the joints by an arthroscope, the stomach by a gastroscope, and so on [134]. Endoscopic instruments have considerably improved minimally invasive procedures and today they play an important role in medicine [135]. However, it has been proven that endoscopy would become more effective if it were possible for endoscopes to relay both visual and tactile information [108].

Endoscopes are a key component of minimally invasive interventions. The benefits of minimally invasive procedures have been well established. These include smaller incisions ($10 - 15\,\text{mm}$ in diameter), fewer complications, shortened postoperative recovery, reduced tissue trauma and postoperative pain. As a result MIS is cost-effective for both hospitals and patients [13, 14]. The improvements in patients' mental and physical quality of life have been analysed and statistically proven in [136]. During minimally invasive procedures, clinicians make several small incisions on the patient's skin, one of which is usually reserved for the endoscopic camera. Images from the endoscopic camera are projected onto monitors in the operating room. Thus, the medical team can see a clear and magnified view of the analysed anatomical area. Other instruments are inserted in the other openings and used to explore, remove or repair internal body parts. Notwithstanding all the advantages that minimally invasive procedures brought into the clinical settings, there is still a lack of haptic (force and tactile) feedback [34, 137] which can enhance the outcome of minimally invasive examination for tumour localization.

Nowadays, the force applied to soft organs during minimally invasive procedures can only be estimated through visual feedback by observing the deformation of the tissue in the displayed camera images. Identification of abnormalities can be cumbersome for an inexperienced practitioner, while the lack of direct palpation during minimally invasive procedures may lead to insufficient feedback and errors. In response to the current state of minimally invasive interventions, many force and tactile sensing technologies for minimally invasive procedures have been developed [29]. However, problems in size,

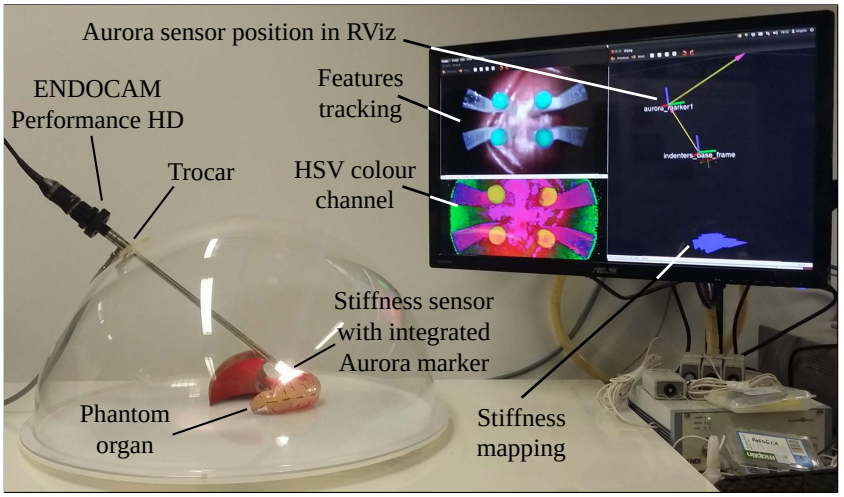

FIGURE 6.1: Beam Stiffness Sensor mounted on the tip of a medical endoscopic camera

compatibility with the medical settings, sterilisability, accuracy and reliability, make these systems unsuitable for real applications.

In this chapter the multi-directional sensing principle presented in chapter 5 has been adopted and embedded to a surgical endoscopic camera. In order to keep the size of the device compatible with the requirements of minimally invasive procedures, the commercial springs that have been used in the development of the previous stiffness sensors have been replaced with elastic beams, reducing the sensor's size significantly. The new design not only makes the sensor lighter but also easier to remove. Additionally, the sensory system is passive and does not require any electronics or an additional trocar port. The addition of the proposed sensor enhances the functionality of the endoscopic camera which can now be used both for visualisation and as a diagnostic instrument. Additionally, by attaching an Aurora magnetic tracker to the sensor, the estimated stiffness can be combined with the pose of the tracker to generate and record a colour-coded stiffness map of the examined soft surface. A schematic representation of the system is shown in Figure 6.1.

6.2 Methodology

The clip-on stiffness sensor has been fashioned for the medical rigid endoscope ENDOCAM Performance HD by Richard Wolf GmbH (30 fps at 60 Hz). The sensor is attached to the tip of the endoscopic camera by a clip so as to be easy to fasten or remove. The overall sensory system, composed by the endoscopic camera and the designed mechanism, can be inserted into the human body through a standard trocar port of $10-15$ mm diameter, thus it fits the size requirements of minimally invasive procedures. The sensor's range depend on the design, i.e. the dimensions of the beams and the mechanical properties of

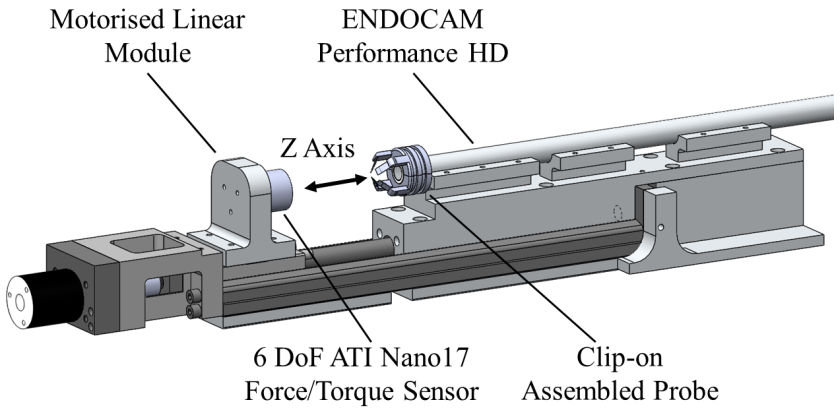

FIGURE 6.2: Calibration device: the motorised linear module pushes the ATI Nano 17 Force/Torque sensor against the stiffness sensor whist recording the interaction forces and the displacement.

the material used to fabricate it. In order to have a system compliant with endoscopic procedures different prototypes have been designed and the response to normal forces has been evaluated.

The finite element analysis (FEA) is a numerical technique that allows the evaluation of the stress, strain and displacement that each point of a solid material exhibits when it is subject to a given force. These techniques has been used to estimate how normal forces will affect the material and design of the prototypes. The FEA simulations have been performed using SolidWorks Simulation toolbox.

The simulation results have been compared with the results obtained using a calibration device which ensures that the endoscopic camera is at a steady state during contact. The system employs a motorised linear module which embeds the ATI Nano 17 Force/Torque sensor, as shown in Figure 6.2. By sliding the linear module, and thus the Force/Torque sensor, against the sensor prototype, the displacements of the beams and the interaction forces generated by the contact are recorded in real-time. When normal forces act on the tip sensor, the beams will move and bent. The movements of each beam in the three dimensional space are related to the movements of the centroid associated to the corresponding visual feature in the camera images. The same sensing principle presented in Chapter 5 is used here to estimate the stiffness of the soft material during endoscopic examination.

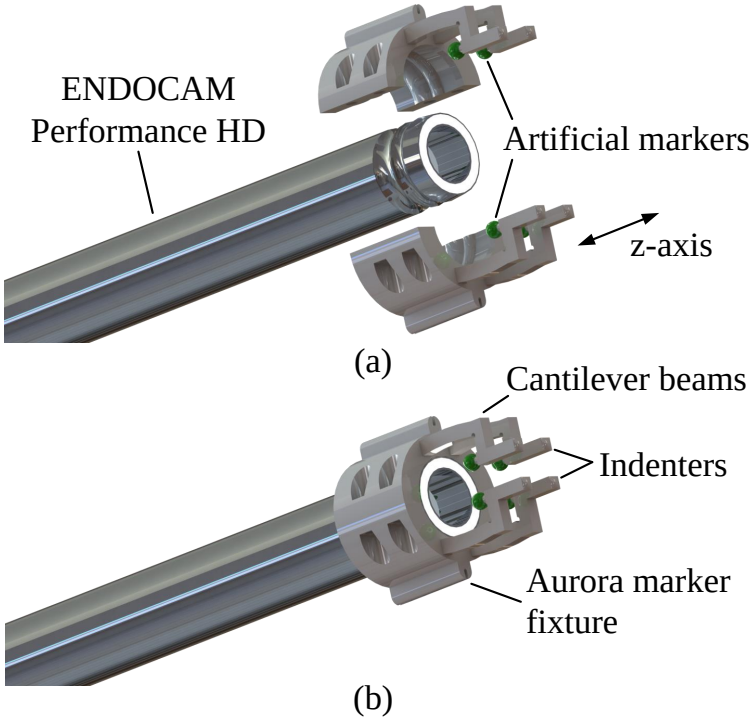

FIGURE 6.3: CAD Drawings of the L-shaped stiffness sensor: (a) Exploded view of the sensor and (b) sensor assembled at the tip of an endoscopic camera.

6.3 Mechanical sensor structure and analysis

Three different sensor prototypes have been designed. The first two are made of ABS material and have been manufactured using a rapid prototyping machine. These sensors suffer from certain limitations, such as the force and beam deflection ranges, To address those a third prototype employing nitilon beams has been developed and tested.

6.3.1 ABS Cantilever Beam

The entire ABS cantilever beam sensor consists of only two parts manufactured of ABS material using a rapid prototyping machine (Project HD-3000 Plus, 3D Systems). The fabrication process is simple; the sensor is low cost and can be easily modified to suit the tip of any camera. The high resolution of the prototyping machine (16 μm of accuracy on the z-axis and 42 μm on the x and y-axis) allows miniaturisation which is essential in order to use the device in MIS.

The sensor consists of two semi-cylindrical symmetrical parts with a cylindrical cavity along the central axis which is used to mount the device onto the camera tip. Each part has two L-shaped cantilever beams with an indenter and a small coloured sphere. The exploded and assembled views of the L-shaped sensor are shown in Figure 6.3. When

the device palpates soft tissue and forces are exerted on the indenters, the beams are bent resulting in a displacement of the related sphere towards the camera. Three beams have identical cross sections, hence identical elasticity. The fourth beam is printed with a bigger cross section and thus has higher elasticity than the others. In the default position, the four beams are within the same plane at an equal distance from the centre of the image plane. Different sizes of indenters and spheres have been tested in order to arrive at a sensor which is as small as possible and robust enough to endure at least a normal force of 1 N. From this analysis the following dimensions for the sensor have been chosen: overall outer diameter of 18 mm, spheres radius of 2 mm, the indenters have a squared tip with area of 2.25 mm^2, perimeters of 6 mm and length of 4.25 mm. The cross section is 2.53 mm for the stiffer beam and 1.96 mm for the soft beams. The overall length of the sensor is 25.28 mm.

At the side of the sensor, a fixture is created which accommodates a 6 degree of freedom (DoF) Aurora magnetic tracker. Using the principle presented in Chapter 5, it is possible to retrieve stiffness data from the sensory device and also map the tissue properties to positional information of the Aurora sensor.

Finite Element Analysis and Calibration

The prototyping material used to fabricate the sensor is acrylonitrile butadiene styrene (ABS) with a yield strength of 44 MPa. The simulated material properties have been extracted from the material data sheet. During the simulation, normal forces have been applied to the tip of the four indenters to evaluate partial and global displacements.

The FEA results are shown in Figure 6.4. When the same force is exerted on each beam, the three beams with higher elasticity are displaced more than the beam with lower elasticity. In Figure 6.5, the simulation results are compared with the results obtained

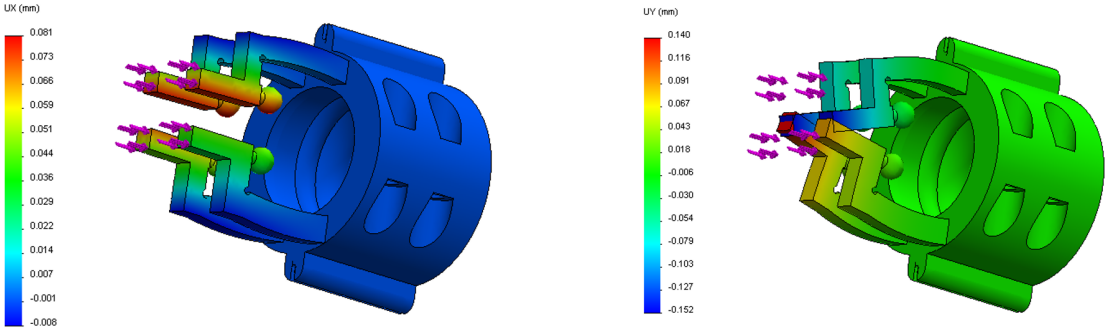

FIGURE 6.4: Finite Element Analysis of the L-shaped stiffness sensor: Forces (pink arrows) are exerted perpendicular to the indenter surfaces. The displacement along the vertical axis (a) is half of the displacement along the horizontal axis (b). In this case the torsion effect causes the beams to touch each other.

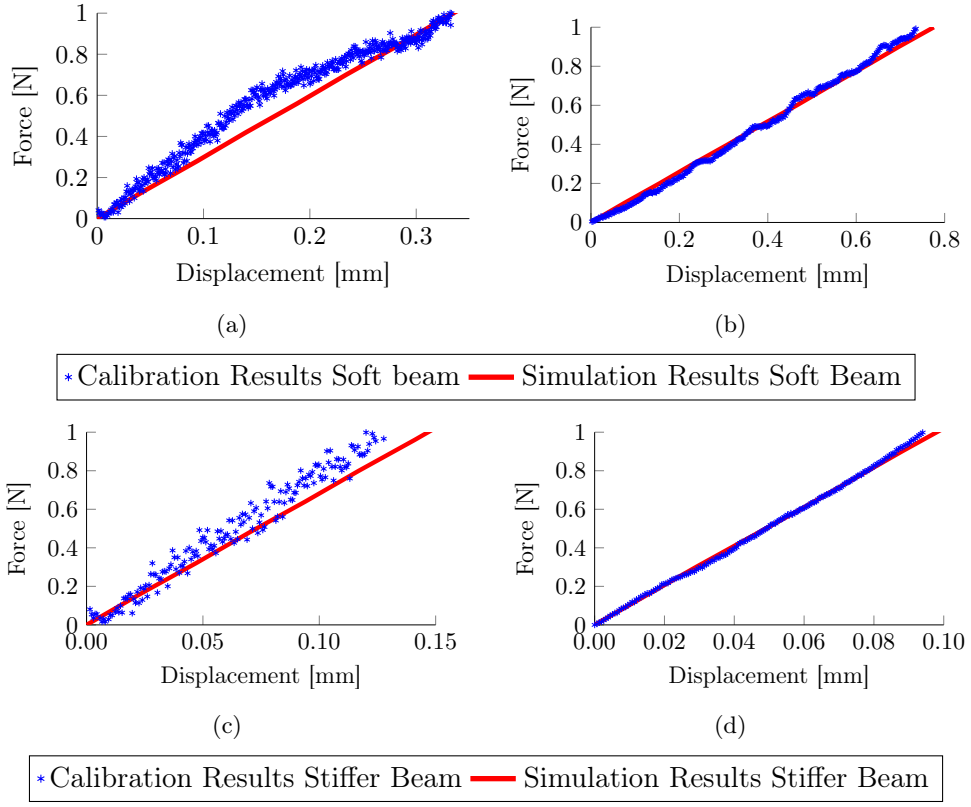

FIGURE 6.5: Simulation and calibration results of the L-Shaped stiffness sensor: the interaction force and the relative displacements along the vertical axis for the soft beam (a) and the stiffer beam (c) and along the horizontal axis for the soft beam (b) and the stiffer beam (d).

using the calibration device. The measured forces for a single soft and stiff beams are plotted against the displacement in z-axis. The results in Figure 6.5 (a) and (c) show that both the stiffer and the softer beams will exhibit only small displacements along the axis in which the force is applied. However, due to torsion, a considerable displacement is observed in the lateral axis, as shown in Figure 6.5 (b) and (d). This unwanted movement which effects the mechanism is due to the sensor structure and the fabrication materials. The FEA results in Figure 6.4 (b) shows the torsion effect which will cause the collision of the beams.

The relationship between measured force and displacement is linear up to 1 N. The yield point is reached at that force value. In this case, the maximum displacement of the beams is only 0.3 mm. The linear fitting for the soft beam has a slope of 1.2 with a Root Mean Squared Error (RMSE) of 0.054; the stiff beam has a slope of 2.66 and a RMSE of 0.119.

If the interaction force is less than 1 N, the sensor will return to its original position after the load is removed. Beyond this displacement, the stress-strain curve is not linear and the beams may fracture.

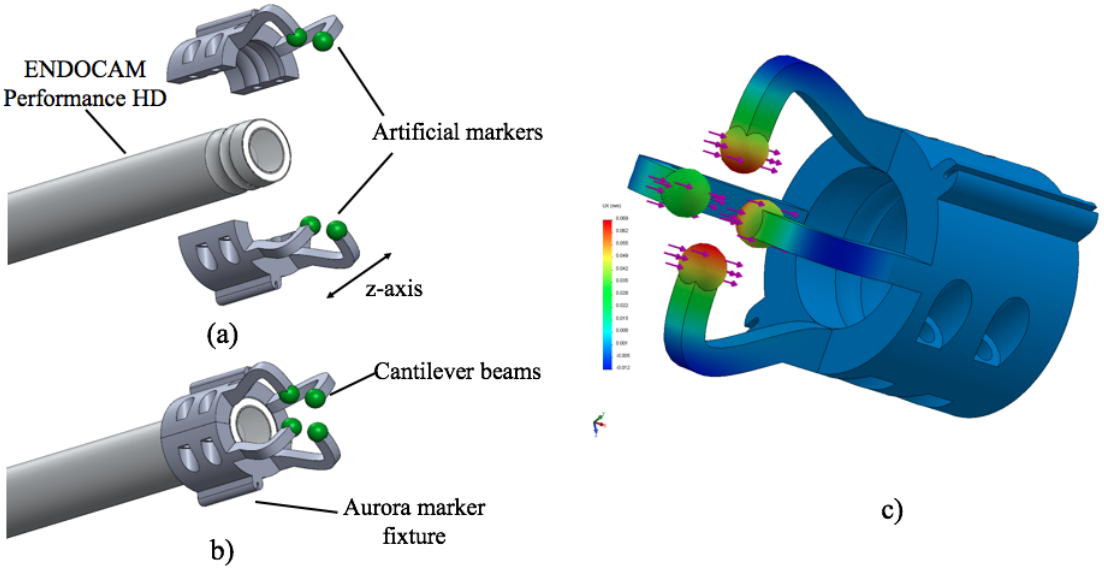

FIGURE 6.6: C-shaped stiffness sensor: CAD drawings showing the exploited view (a) and the assembled view (b). The results of the FEA simulation (c). The pink arrows indicate the direction of the force.

The torsion effect in the first ABS prototype is caused by the squared indenters which are interacting with the soft tissue. To eliminate these unwanted movements a C-shaped prototype has been designed. The new sensor is a modification of the first prototype in which the spheres are used to directly indent the soft tissue. Figure 6.6(a) and (b) illustrate the exploded and assembled views of the C-shaped prototype. The outer diameter of this sensor is 18 mm, the spheres have a radius of 1.45 mm and area of 21.36 mm^2, a perimeter of 1.58 mm, and a length of 9.11 mm; the cross section is 2 mm for the stiff beam and 1.70 mm for the soft beam. The total length of the sensor is 22 mm.

Although this new sensing prototype does not present any lateral movements, it is too

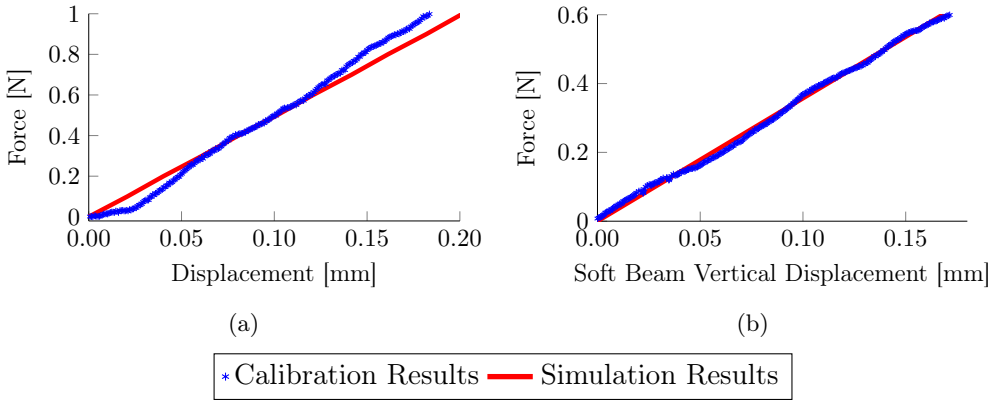

FIGURE 6.7: Calibration and simulation results of the C-shaped stiffness sensor: The displacements of the beams along the vertical axis in simulation and calibration of the soft beam (a) and the stiffer beam (b).

stiff and thus not suitable for medical applications. The results of the FEA simulation are shown in Figure 6.6(c). In Figure 6.7 (a) and (b), the simulation results are compared with the output of the calibration. The stiffer and the softer beams will exhibit only small displacements along the vertical axis on which the force is applied. The relationship between the applied force and displacement of the stiffer beam has a linear trend up to 0.6 N. The yield point is reached at that force value. In this case, the maximum displacement is only 0.16 mm for the soft beam and 0.15 mm for the stiff beam. The linear fitting for the soft beam has a slope of 1.9 with a RMSE of 0.034; the stiff beam has a slope of 3.4 and a RMSE of 0.059.

6.3.2 Nitinol Cantilever Beam

The problems and limitations of the ABS prototypes, e.g. the range of force and displacement, are not only due to the design, but also due to the mechanical properties of the fabrication material. A material with different properties, i.e. steel or aluminium, could be used to fabricate the beams embedded in the sensor and to have the desired force range and resolution. Nitinol is a complex, superelastic material whose properties, such as MRI compatibility and corrosion, make it an attractive developing material for medical devices used in minimally invasive intervention and endoscopic procedures [138]. Thus, a new prototype, which employs cantilever beams made by a metal alloy of nickel and titanium (nitinol) with a Young Modulus of 40 GPa, has been manufactured.

The exploded and assembled views of the sensor are shown in Figure 6.8. The sensor consists of two semi-cylindrical symmetrical parts with a cylindrical cavity along the central axis which is used to mount the device onto the camera tip. Each part has two

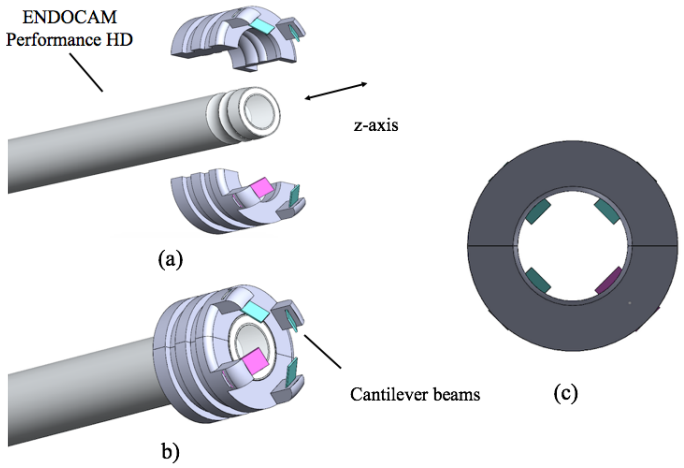

FIGURE 6.8: CAD Drawings: (a) Exploded view of the sensor, (b) sensor assembled at the tip of an endoscopic camera, (c) camera field of view.

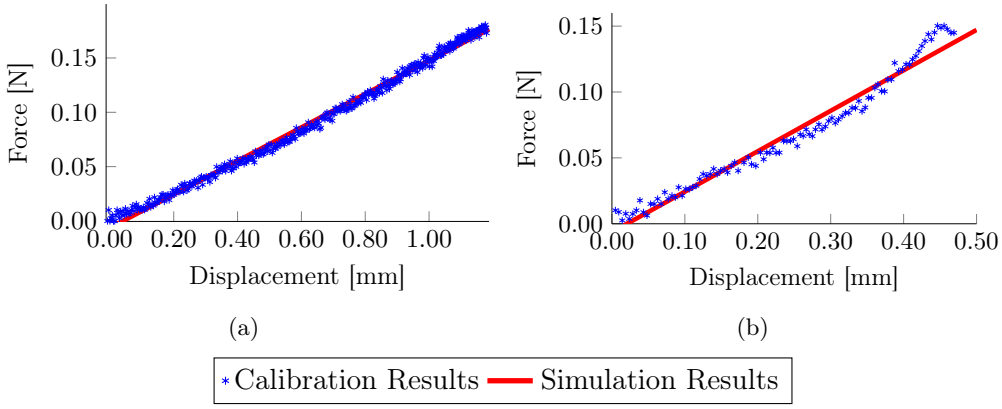

FIGURE 6.9: Nitilon cantilever beam for endoscopic camera : The displacements of the nitinol beams along the vertical axis in simulation and calibration of the soft beam (a) and the stiffer (b).

rectangular cantilever beams tapered with an angle of 40° as shown in Figure 6.8. Three beams have identical cross sections, hence identical elasticity. The fourth beam has a bigger cross section, thus it has a lower elasticity than the others. When the beams palpate soft tissue they bent towards the camera, thus they change their positions in the camera images. An image processing algorithm tracks the movements of the visual beams which are related to the bending in the 3D space. The default positions of the four beams are within the same plane are at equal distance from the centre of the image plane. Therefore, due to the similarity between the beams and springs used in the sensor developed in Chapter 5, the sensing principle can be fashioned and adopted to model the cantilever sensor. The outer diameter of this prototype is 15 mm. The soft beams are 6.29 mm in length, 2.38 mm^2 in width and 0.25 mm in height. The stiffer beam is 6.29 mm long with a width and height of 2.9 mm and 0.40 mm, respectively. The total length of the sensor is 16.59 mm. Exploded and assembled views of the sensor are shown in Figure 6.8. The relationship between the measured force and displacement has a linear trend up to 1.8 N. A normal force of 0.15 N will generates a displacement of 1 mm of the soft beams and 0.5 mm of the stiff beam. The linear fitting for the soft beam has a slope of 0.8 with a RMSE of 0.023; the stiff beam has a slope of 1.3 and a RMSE of 0.035.

The nitilon sensor has higher sensitivity and is smaller in size than the ABS prototypes. The sensor's diameter is only 15 mm, thus it is able fit in a standard trocar port. Additionally, the occlusions of the camera's field of view is minimal, thus it allows a wide visualization of the anatomical area. The comparison between simulation and calibration results are shown in Figure 6.9. Both beams bend consistently even when the applied normal force is small. The elasticity of the soft beam is twice as high as the elasticity of the stiffer beam. The sensor range and resolution can be customised by making the cantilever beams out of a material with different Young Modulus, i.e. different elasticity.

6.3.3 Tracking of the cantilever beams

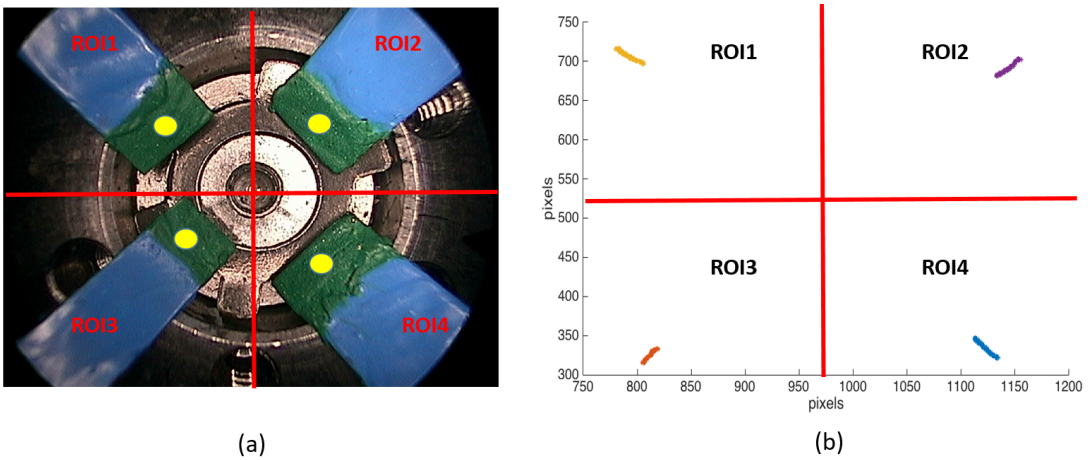

FIGURE 6.10: Image processing algorithm for the nitinol cantilever beam stiffness sensor. (a) Position of the beams in the image at the maximum displacement (indentation of 2.5 mm). (b) Tracking of the centroid in their ROI during indentation.

The analysis of the results from the different sensor prototypes showed that the nitinol cantilever beams have higher sensitivity and better force/displacement ranges than the ABS prototypes. Hence, this sensor was chosen and adapted to the stiffness sensing mechanism developed in Chapter 5. The image processing algorithm evaluates the relationship between the bending of the cantilevers and their visual appearance in the images. The image has been subdivided into four Regions of Interest (ROIs), as shown in Figure 6.10, where the tracking of each beam is performed. The trajectories generated by the centroids of each visual feature during indentation are shown in Figure 6.10 (b) .

The results of the calibration tests performed in Chapter 6.3.2 demonstrate that the relationship between the displacement of the nitinol beams and the applied normal force is linear (Figure 6.9). The results of the image processing algorithm also show that there is a linear relationship between the position of the centroids in the image and the displacements of the beams, Figure 6.11 (a) and (b). The correlation between the positions of the centroids and the displacements of the beams allows to directly link the variation of the centroid to an applied force, Figure 6.11 (c) and (d). For instance, the soft beam responds to a normal force of 0.1 N with a displacement of 0.6 mm, Figure 6.9 (a). This corresponds to a movement of 10 pixels of the centroid of the corresponding visual beam, Figure 6.11(a). The relationship between the movements of the beams and the variation of the centroids in the images allows to directly compute the applied force as a function of the beams' centroids, Figure 6.11(c). Thus, for small indentation, the beams behave as springs. Therefore, the mathematical model derived in Chapter 5 can be adopted to estimate the soft tissue stiffness as function of the relative forces which is derived through the tracking of the centroids of the beams.

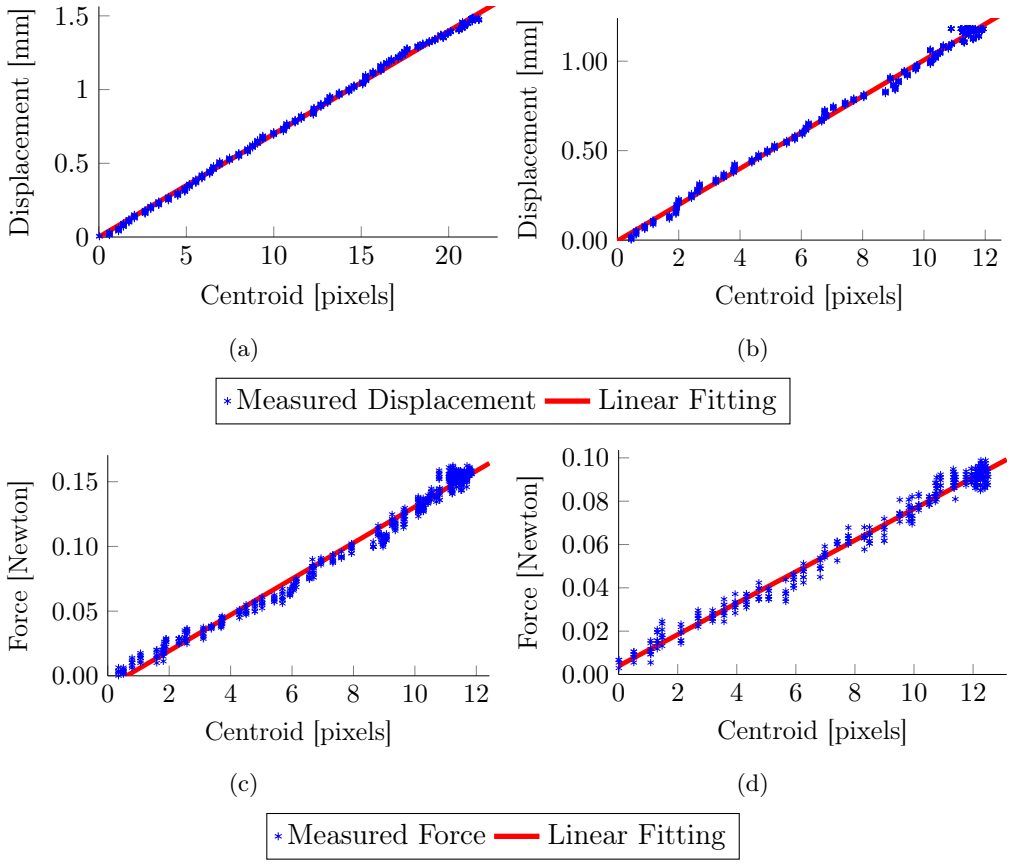

FIGURE 6.11: Nitinol beam stiffness sensor results as a function of the visual appearance in the camera images. Relation between tracked feature centroid and displacement of the soft beam (a) and stiffer beam (b). The variation of feature centroids due to an external force for the soft beam (c) and stiffer beam (d).

6.4 Discussion and Conclusions

In this chapter, the multi-directional vision-based stiffness sensing principle, derived in Chapter 5, has been used to develop a clip-on stiffness sensor for endoscopic examination. The sensor employs cantilever beams which are used to palpate soft tissues. The bending of the beams, generated by the interaction with external soft surfaces, is captured by the endoscopic camera. A vision processing algorithm uses the endoscopic camera's images to compute the interaction forces which are then used to model the stiffness of the soft tissue.

To be compatible with minimally invasive procedures, the endoscopic sensor should be small enough to be attached to the camera tip and still fit in a standard trocar port. Additionally, the sensor should respond to normal forces up to 1 N with a considerable displacement along the vertical axis. Three different prototypes have been designed and their response to normal forces has been evaluated in simulation and by using a customised calibration device. The mechanical drawing of the developed sensors is shown

in Appendix D. The first two prototypes have been manufactured by using ABS material. Due to the limitations of these sensors, a third prototype, which employs beams made of nitilon, has been developed. The results of the investigation demonstrated that the proposed system can be successfully integrated with a medical endoscopic camera and used to estimate the stiffness of anatomical areas during minimally invasive procedures. Furthermore, different materials could be used to manufacture the sensor and customise its range and resolution. Table 6.1 summarises the findings of the analysis carried out: the L-shaped prototype is effected by torsion and respond to a normal force by translating along the horizontal axis. Both ABS sensors prototypes respond to normal force with small displacements. However, the range and resolution of the endoscopic sensor can be customised by using different manufacturing materials. Nitinol alloy has been used to manufacture the cantilever beams embedded in the sensor prototype. The mechanical properties of this material improves the force/displacement range and eliminates the torsion which affected the ABS prototypes. Hence, this sensor has been further explored and used to find the relationship between the movement of the beams and their visual appearance in the camera images. The results of this investigation demonstrate that there is a linear relationship between the movements of the beams in the three dimensional space and the movements of the correlated visual features in the images. This findings demonstrates that‘ the interaction force can be directly estimated as function of the movements of the beams in the images. Furthermore, for a range of force up to 1N the nitinol cantilevers behaves like linear springs, hence the mathematical model derived in chapter 5 can be directly adopted to model this device.

	L-Shaped	C-Shaped	Nitinol
F	1	1	0.15
Δv_{xsoft}	0.3	0.2	1
Δv_{stiff}	0.15	0.15	0.50
Δh_{soft}	0.8	-	-
Δh_{stiff}	0.10	-	-

TABLE 6.1: Properties of clip-on stiffness sensor: Applying a normal F to the cantilever's beam, they will exhibit an horizontal displacement of D_h and a vertical displacement of D_v. The table shows the vertical and horizontal displacements of the soft and stiff beams for each developed prototype.

CHAPTER 7

Real-time Mapping of Soft Tissue Stiffness

The technological advances in medical robotics are continuously revolutionising the medical setting with the introduction of sophisticated equipment and complex signal processing methodologies. However, to be approved by the medical community the new systems should be ergonomic and intuitive. For instance, a medical palpation device should include computerised algorithms able to interpret the information acquired during the examination and to develop an intelligible representation of it which has to be conveyed to the clinicians. An explicit and intuitive representation of the measured soft tissue stiffness is obtained by a real-time colour codification. Hence, the stiffness distribution of anatomical surfaces can be stored during the medical examination in a colour-coded stiffness map. This map will help the clinicians to assess the stiffness distribution of the overall examined area, thus to easily detect abnormalities.

7.1 Introduction

Stiffness mapping techniques aim to measure the stiffness values of a soft object across a wide region and relate individual stiffness measurements to their spatial occurrence along the examined surface. These methodologies are employed in medical diagnosis to visualise and record the mechanical properties of the anatomical areas. Palpation instruments are able to sense mechanical properties of external body parts, i.e. breast, or inner organs, during minimally invasive and robotic inspection procedures by analysing the reaction of the tissue to a contact. These instruments have been widely explored in the last few decades [139]. The aim of these instruments is to convey the information acquired through the sensing mechanism in an intuitive and intelligible way to clinicians. The colour-coded tissue stiffness map is the most used visualization method.

Tracking devices are essential components of medical inspection systems. These devices are used to track the 3D position of the instrument in relation to the patient's anatomy. Optical tracking systems are very accurate and can work in a relatively large workspace. However, the line-of-sight between the tracking device and the instrument has to be maintained during the procedure. Therefore, electromagnetic tracking systems (EMTS) that have no line-of-sight requirements have been quickly adopted in medical examinations [140].

In robot-assisted procedures, the medical instrument is positioned on the end-effector of the robotic arm. In this way, the kinematic of the robot can be used to retrieve the position of the tool-tip and track its movements during the examination. Therefore, the choice of the tracking system is application dependent and requires an evaluation of the desired working volume and accuracy requirements.

To meet these needs, the developed multi-directional stiffness probe has been integrated with an electromagnetic tracking system as well as a robotic arm. Thus, by tracking the 3D position of the probe, stiffness values are recorded and a real-time colour-coded stiffness map of the analysed tissue is generated.

7.2 Methodology

In order to map the stiffness of the soft tissues in real time when performing palpation with a medical instrument, the pose of the device needs to be measured and recorded. Different technologies can be used to assess the 3D position of an object in real time, e.g. magnetic, optical and visual motion tracking systems. Moreover, in medical systems employing robotic platforms, i.e. teleoperation, the device is attached to the end-effector

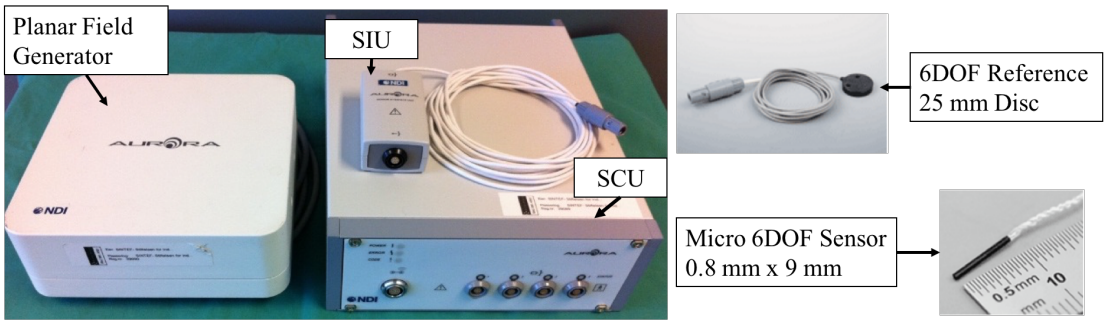

FIGURE 7.1: NDI Aurora Tracking System: (a) The planar field generator which can be mounted in a positioning arm for precise placement; the system control unit (SCU) controls the field generator, collects tracking data, calculates the position and orientation of each sensor and interfaces with the PC; the sensor interface unit (SIU) amplifies and digitalises the electrical signals from the sensor while minimising potential data noise. (b) The 6 DOF micro sensor and reference tool.

of a robot arm. Thus, the kinematic of the robot is used to retrieve the pose of the tool attached to its end-effector.

The multi-directional stiffness probe, presented in Chapter 5 has been integrated with a commercially available tracking system and used to evaluate the stiffness of soft tissues. Hence, the pose of the device is used to record a colour-coded stiffness map in real-time. In addition, to evaluate the performance of the proposed sensory mechanism in robot assisted technologies, the device has also been fixed to the tip of a robotic arm, thus the kinematic of the robot is used to map and record the measured stiffness.

7.2.1 Real time Stiffness Mapping using a magnetic motion tracking system

When compared with the traditional optical tracking systems, electromagnetic tracking systems are not hampered by line-of-sight limitations, so they are able to track objects even through obstacles. Additionally, they allow the tracking of multiple targets at the same time. Even though electromagnetic tracking systems are susceptible to distortion from nearby metal sources and present limited accuracy, they are widely used in medical applications. The multi-directional stiffness sensor is equipped with the Aurora system from Northern Digital Inc. (NDI), a commercially available stand-alone electro-magnetic tracker system for medical applications.

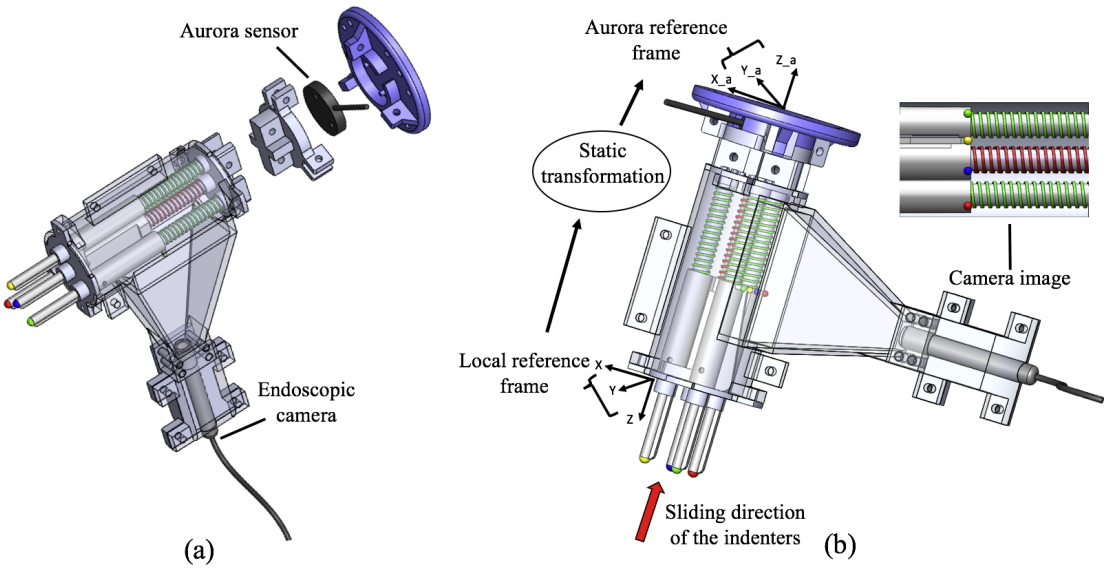

FIGURE 7.2: Hand-held stiffness probe fixed at the tip of the robotic arm: the interaction with external objects generates the sliding of the indenters. Hence, the visual features change their positions in the camera's image. The correlation between the indenters and the features allows for the measurement of the new positions of the indenters in the local reference frame. A static transformation maps the new positions of the indenters from the local frame into the robot kinematic chain.

7.2.1.1 NDI Aurora Electro-magnetic Tracking System

The Aurora system is compliant with medical equipment safety standards, allows sub-millimetric and sub-degree tracking with no line-of-sight restrictions, can be easily integrated, and operates with medical-grade metals. Aurora uses an electromagnetic field generator to track induction coils. The system control unit regulates the field generator and collects data from the sensor interface units to measure the position and orientation of each sensor. An alternating current excites the six differential coils enclosed in the field generator and creates six induction voltages which are transmitted to the system control unit by the sensor interface unit. As a result, the 3D position of the sensor coil is tracked in real-time. The main components of the Aurora tracking system are shown in Figure 7.1.

One Aurora tracker is fixed to an allocated position on the stiffness probe, as shown in Figure 7.2(a). Thus, the position and orientation of the probe can be tracked and recorded whilst examining a tissue area. The developed system does not use any electronic or metal sources, so there is no risk of affecting the performances of the electromagnetic tracking system.

The pose of each indenter at rest condition is expressed in a local reference frame which is fixed on the stiffness probe as shown in Figure 7.2 (b). These positions are jointly mirrored to specific positions of the visual features in the image. A static transformation

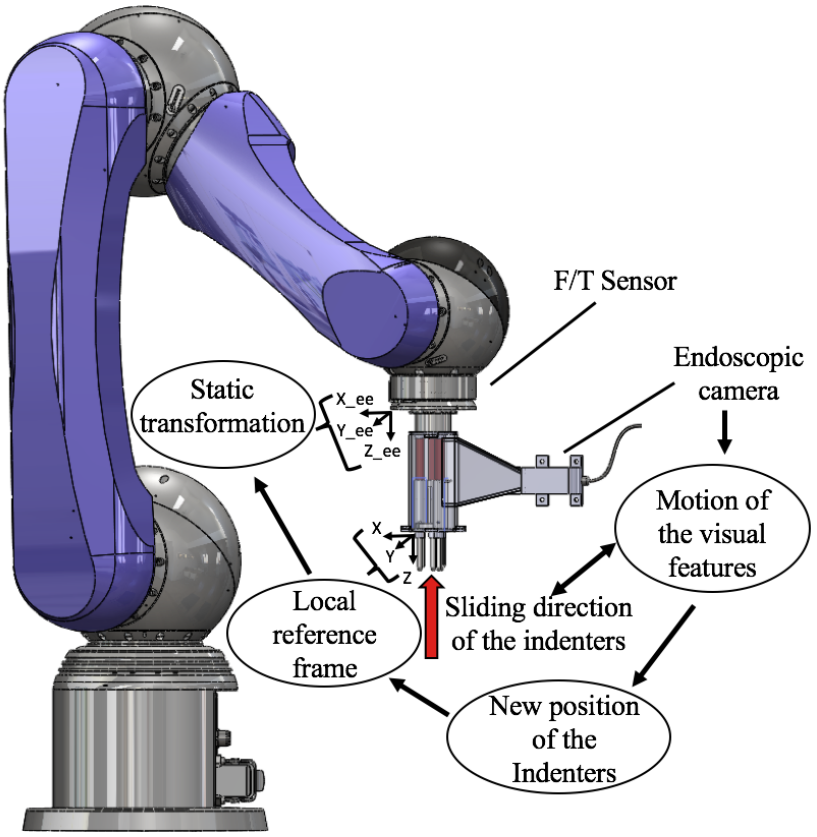

FIGURE 7.3: Hand-held stiffness probe fixed at the tip of the robotic arm: the interaction with external objects generates the sliding of the indenters. Hence, the visual features change their positions in the camera's image. The correlation between the indenters and the features allows to measure the new positions of the indenters in the local reference frame. A static transformation maps the new positions of the indenters from the local frame into the robot kinematic chain.

from the local reference frame into the Aurora tracker frame ${}^{a}T_p$, is used to record the global positions and the orientation of the indenters:

$$ {}^{t}T_p = {}^{t}T_a {}^{a}T_p \tag{7.1} $$

where ${}^{t}T_a$ expresses the position of the tracker and ${}^{a}T_p$ is the translation matrix, along the z axis, between the tracker frame and the frame with origin on the stiffness probe.

7.2.2 Real time Stiffness Mapping using an industrial robot

The objective of using robots in medicine is to provide more accurate diagnoses and improve the experience of patients by performing smaller and more precise interventions.

Nowadays, robots are part of the medical equipment and used in many medical treatments as well as in challenging surgeries, such as coronary artery bypass and removal of cancerous tissue from sensitive parts of the body [141]. Generally, medical robotics systems employ numerous arms, each arm carrying an instrument, such as a camera, a gripper or various other surgical tools, on the tool tip. The physician controls the robotics arms from a console that is equipped with a screen showing the surgical site and the various instruments. Hence, he/she does not need to be in the same room, or even in the same location as the patient. Moreover, the use of robots that are able to perform steady and smooth movements ensure high precision and accuracy even in long operations, as unlike physicians they do not experience fatigue and tremors. Perhaps the downside of these innovative and sophisticated systems is that that surgeons need to invest extensive training time in order to learn to use them. Additionally, the sense of touch which the physician employs in open surgery is completely lost when robotic systems are used. Therefore, in order to enhance or ameliorate the physician's experience during robotic surgery, researchers have been exploring sensing technologies to be attached at the tip of the robot arm. These sensors should be able to measure the mechanical properties of anatomical areas and transmit them back to the physicians in real time.

To evaluate the performance of the vision-based stiffness sensing mechanism in medical robotics applications, the stiffness probe is fixed to the end-effector of the Lightweight Arm LWA 4P by SCHUNK, an industrial 6 DOF robot arm. A multi-axis ATI force/-torque sensor is attached to the end-effector of the robotic arm and the stiffness sensor is fixed to the front plate to palpate silicone phantoms as shown in Figure 7.3. The kinematics of the robotic arm are used to compute the pose of the stiffness probe while recording the reaction forces measured by the force/torque sensor in real-time.

7.2.2.1 Kinematic Modelling of the Schunk Powerball Lightweight Arm

The Lightweight Arm LWA 4P is a reconfigurable modular robot arm composed of interchangeable modules, which are flexible, robust and inexpensive, compared to the fixed structure counterparts. As a result, this robotic manipulator can be used in industry as well as in research. This manipulator is composed of three Powerballs which are connected through two links. It has a high gear ratio for each of its axes, thus it is insensitive to gravitational loading. However, since the gearing is harmonic and the ratio is not too high, it can still be back driven for impedance control and friction identification. The robot arm can be used with any controller that supports multiple CANOpen devices; here, it is used with the Robotic Operating System (ROS). Hence, the robot controller is seamlessly integrated with the image processing algorithm to generate the real time

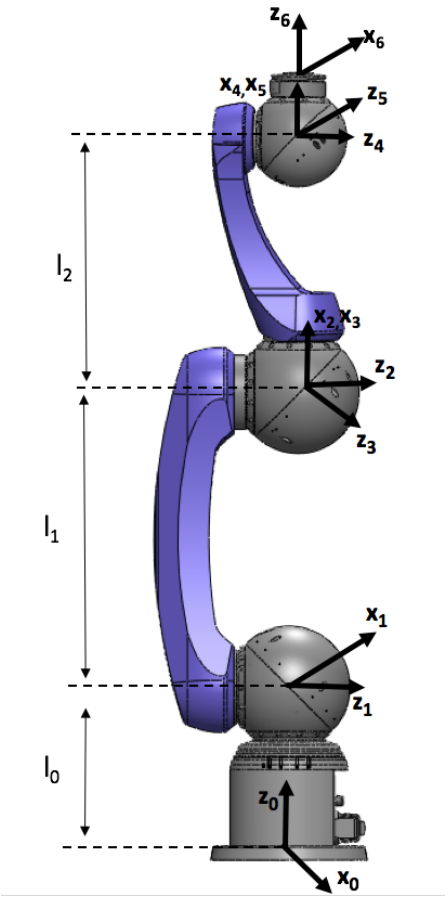

FIGURE 7.4: Schunk LWA 4P Forward Kinematics: assigned coordinate frame for the Denavit-Hartenberg Representation.

stiffness map.

The kinematic of a robotic arm provides an analytical description of its spatial movements by relating the position and orientation of the end-effector and its joint variables. The kinematic modelling of a manipulator's position is sub-divided into two sub-problems: inverse and direct kinematics. The direct kinematics maps the joint angles of the robot to a pose, that is, position and orientation, in the Cartesian space. The inverse kinematics converts a pose in the Cartesian space into a set of joint angles. The Denavit-Hartenberg (DH) convention defines a parametrization of each joint describing the relative position and orientation of two consecutive links. The DH parameters are d, a, θ, which is the input of variable of the rotational joint, and α, which is the input variable of the prismatic joint. The transformation from one joint to the next in the kinematic chain is defined by the four DH parameters: θ defines the rotation between the z-axis; α defines the angle between z-axes of joints; d defines the distance along z-axis between joints; a defines the distance along x-axis between joints. The Schunk LWA 4P is composed by 6 rotational Powerballs, hence θ is the input variable for each set of the DH parameters. Table 7.1 shows the DH parameters for the coordinate frame assigned as

shown in Figure 7.4. The DH parameters allow the computation of each successive joint

i	a_i	α_i	d_i	θ_i
1	0	$\frac{-\pi}{2}$	0.205	θ_1
2	0.35	0	0	θ_2
3	0	$\frac{\pi}{2}$	0	θ_3
4	0	$\frac{-\pi}{2}$	0.304	θ_4
5	0	$\frac{\pi}{2}$	0	θ_5
6	0	0	0	θ_6

TABLE 7.1: Denavit-Hartenberg parameters for the Schunk LWA 4P: the coordinate frame are shown in 7.4. The distance from the base to the first powerball d_1 is 0.205 m, the length of the first link, a_2, is 0.35 m and the length of the second link, d_4, is 0.304 m.

transformation matrix, which is multiplied to derive the homogeneous transformation matrix that expresses the pose of the end-effector in the base frame ${}^0T_6$:

$$ {}^0T_6 = {}^0T_1 {}^1T_2 {}^2T_3 {}^3T_4 {}^4T_5 {}^5T_6 \tag{7.2} $$

where each ${}^{\text{i-1}}T_i$ has the form:

$$ {}^{\text{i-1}}T_i = \begin{bmatrix} \cos\theta_i & -\sin\theta_i \cos\alpha_i & \sin\theta_i \sin\alpha_i & a_i \cos\theta_i \\ \sin\theta_i & \cos\theta_i \cos\alpha_i & -\cos\theta_i \sin\alpha_i & a_i \sin\theta_i \\ 0 & \sin\alpha_i & \cos\alpha_i & d_i \\ 0 & 0 & 0 & 1 \end{bmatrix}. \tag{7.3} $$

The transformation matrix which expresses the local frame with origin on the stiffness probe into the base frame :

$$ {}^0T_p = {}^0T_6 {}^6T_p. \tag{7.4} $$

Given the six joint values, [θ_1,..., θ_6] and the DH parameters, the pose of the end-effector is fully determined by the homogeneous transformation matrix ${}^0T_6$. Consequently, the position of the local frame with origin on the stiffness probe is obtained by

multiplying the homogeneous matrix for the translation matrix ${}^{6}T_{p}$, which expresses a translation along the z-axis.

7.3 Experimental Results

Manual and robotic palpations of silicone phantoms have been performed in order to map the measured stiffness into a colour-coded three-dimensional map. The first set of experiments was conducted to evaluate the ability of the stiffness probe to map the stiffness of materials that present different elastic properties. In the second set, a customised silicone phantom with an embedded area of different stiffness values was used to detect stiffness changes.

During the manual palpation tests, the Aurora tracker is fixed to an allocated position on the stiffness probe as shown in Figure 7.2(a). The movements of each indenter are evaluated by tracking the corresponding spherical feature in the camera image. The pose of the indenters into the local frame with origin on the stiffness probe is expressed in the tracker reference frame by using equation 7.1. A schematic representation of the working principle is shown in Figure 7.2(b). Equation 7.2.2.1 is used during the robotic tests to relate the pose of the indenters with the position and orientation of the end-effector of the robot, as shown in Figure 7.7.

The sliding of each indenter is mirrored on to the sliding of spherical features along the horizontal axis of the camera image. Thus, the variation in position of the visual features in the image is used to determine the movements of the indenters in the local reference frame. The approaching pan and tilt angles, the displacements of the soft tissue in the points of contact with the indenters, and the stiffness of the examined area are measured in real-time using the mathematical model derived in Chapter 5.5.1, Three of the indenters are allocated in the vertex of a triangle and one on its barycentre. The mapping of the positions and orientations of the indenters is used to visualise and record a triangle in a global colour-coded stiffness map. The colour of the visualised triangle is function of the measured stiffness, i.e. light colours are associated to low values of the soft tissue stiffness and dark colours to higher values.

The association of the stiffness of the examined area to the displayed colour in the map allows for the easy determination of the variation of the mechanical properties of the soft tissue. Besides, after the examination of the anatomical area, the colour-coded stiffness map can be used to evaluate the stiffness distribution on the whole of the surface. The sensory system works in real-time and does not require any model or prior knowledge of the examined anatomical area.

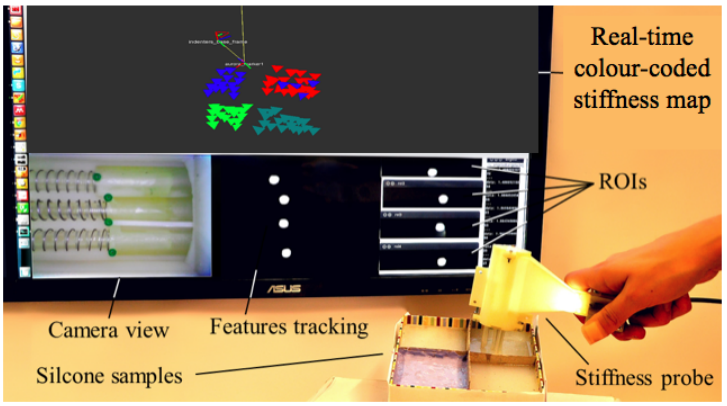

FIGURE 7.5: Stiffness mapping of homogeneous silicone phantoms: the experimental setup. The real-time image processing and stiffness mapping of the probed material are displayed in real-time during the examination. The stiffness values associated to the examined areas are recorded and used to generate a colour-coded stiffness map.

7.3.1 Stiffness mapping of Homogeneous Silicone Phantoms

The hand-held stiffness probe is equipped with the Aurora reference disk tracker, as shown in Figure 7.5, and used to palpate silicone phantoms presenting different stiffness values while at the same time visualising and recording a colour-coded stiffness map. Four homogeneous silicone phantoms made by different materials have been used during these tests. The material used are: Oomoo®30A, Dragon Skin® 20A, Ecoflex®00-50 and Ecoflex®00-10 by Smooth-On. The test results in Figure 7.6 show that our sensor is able to successfully distinguish materials with different stiffness levels even if the difference is relatively small as for example when comparing Dragon Skin®20A to Ooomo® 30A - a scenario in which manual finger palpation fingers fails. The values

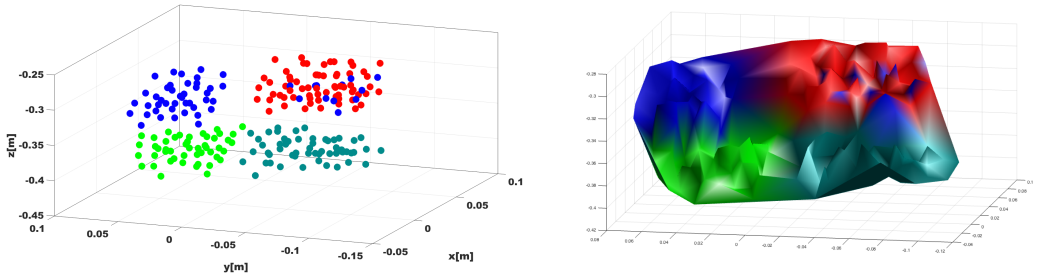

(a) (b)

FIGURE 7.6: Evaluation tests with four different types of silicone materials: the discrimination between the different stiffness values of the silicone samples is visible in the coloured points in (b); the post-processed stiffness map is illustrated in (c). In (b) and (c), the four colours represent the different stiffness values of the material: the green colour is associated with the Oomoo®30A, the blue with the Dragon Skin® 20A, the cyan with the Ecoflex®00-50 and the red with the Ecoflex®00-10.

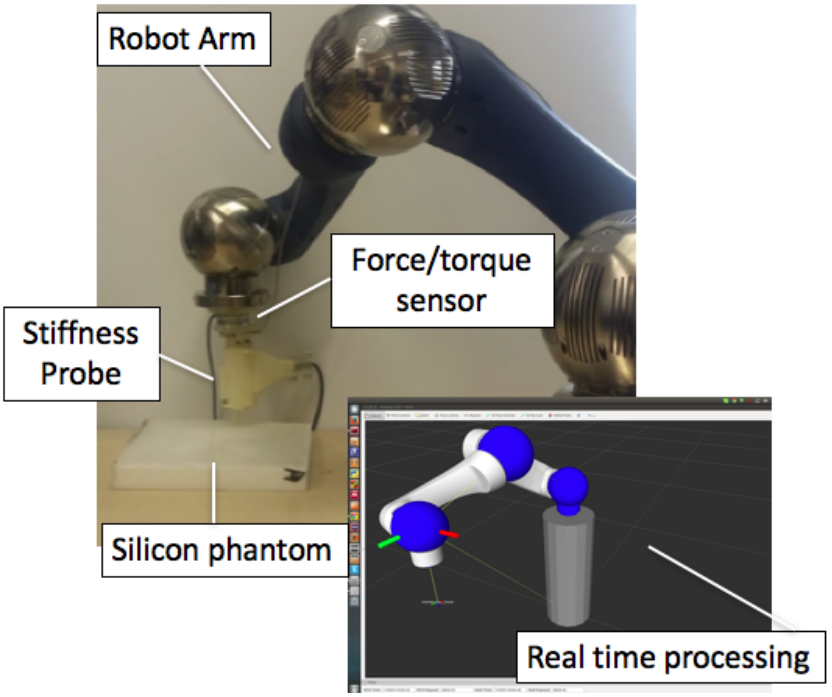

FIGURE 7.7: Stiffness mapping of silicone phantom presenting different stiffness values: The experimental setup. The stiffness probe is attached to the end-effector of the robot arm and used to palpate the phantom. A real-time processing algorithm relates the movements of the visual features in the camera images to the sliding of the indenters by employing the forward kinematics of the robot arm.

associated to those two materials are represented in blue and green in Figure 7.6 (a) and Figure 7.6 (b). The stiffness probe fails to distinguish between those two materials in 8% of cases.

7.3.2 Palpation of Silicone Phantom embedding area of different stiffness

Evaluation tests have been performed using the SCHUNK Lightweight Arm LWA 4P. A multi-axis ATI force/torque sensor was attached to the end-effector of the robotic arm and the stiffness sensor was fixed to the front plate to palpate silicone phantoms, as shown in Figure7.7. The forward kinematics of the robotic arm were used to compute the pose of the stiffness probe while the force/torque sensor recorded the reaction forces in real time. The silicone phantom used in this test is made of Ecoflex®00-10 by Smooth-On, a material which is similar in its mechanical behaviour to the human skin. The mathematical function that directly expresses forces measured in terms of the indenters' displacement is derived using Matlab Curve Fitting Tool, where the best fit to the data points is found. Figure 7.8 shows the experimental results obtained from the benchmarking sensor, the proposed visual processing algorithm and the fitted curve

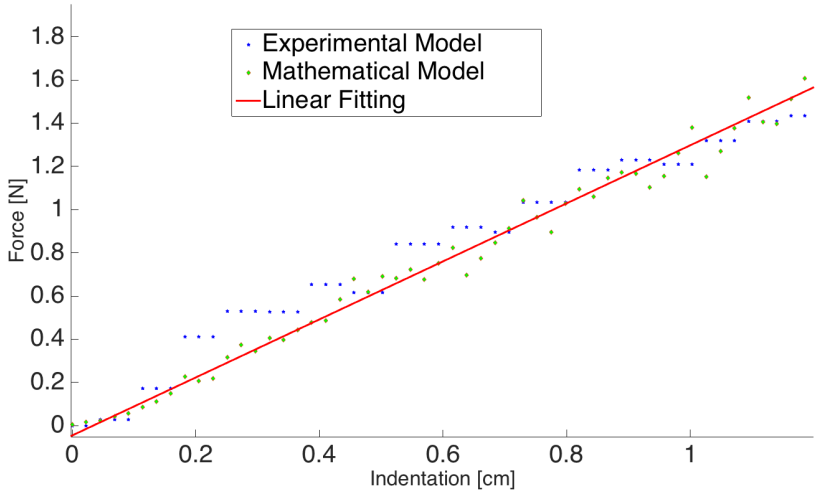

FIGURE 7.8: Experimental Results: the experimental data obtained from the benchmarking sensor (blue), the output of the visual processing algorithm (green) and the model fitting curve (red).

which is obtained using the linear function in Equation 7.5.

$$F(x) = p_1 \cdot x. \tag{7.5}$$

The value of the parameter found was $p_1 = 1.3$. The fit has a prediction interval of 95% and its RMSE is 0.03.

A customised phantom presenting areas of different stiffness values as shown in Figure 7.9(a) has been used to validate the ability of the proposed system in mapping the phantom's stiffness in real time. The phantom mould has an embedded K-shaped track, which is etched (2 mm depth) on the flat ABS surface, and has been filled with Ecoflex®00-10 by Smooth-On.

The experimental rig and the results of the tests are shown in Figure 7.9. The final stiffness map is shown in Figure 7.9(c). Using the stiffness probe, it is possible to capture the difference in stiffness between the embedded silicone and the K-shaped track as shown in Figure 7.9(c) and Figure 7.9(d). For these reasons, our sensing mechanism has high potential in applications where clinicians need to distinguish between soft and stiff tissue areas for the detection of abnormalities.

7.4 Discussion and Conclusions

In this chapter, the multi-directional stiffness probe presented in chapter 5 has been used in combination with an electro-magnetic tracking system and a robotic arm to create a real time colour-coded stiffness map. Experimental results show that the proposed sensor

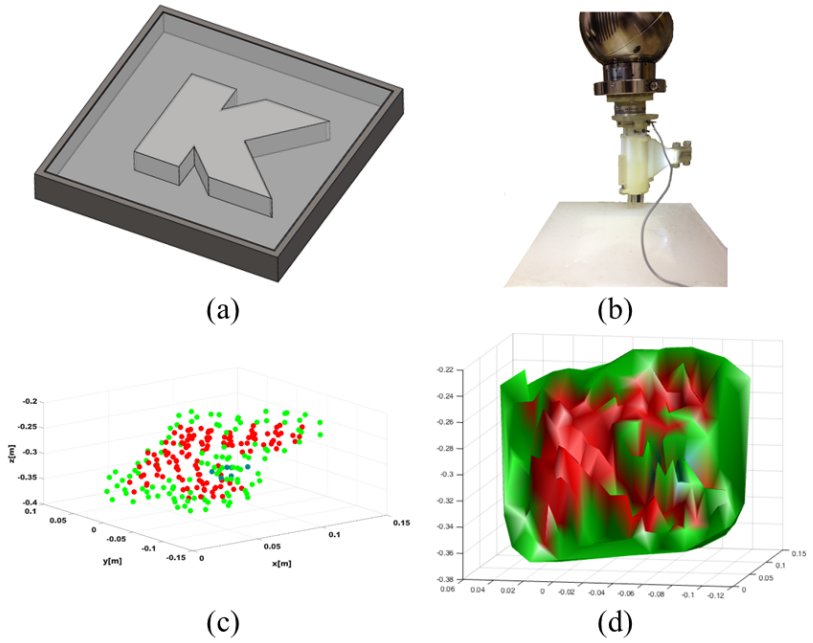

FIGURE 7.9: Computation of the stiffness map: (a) shows the CAD model of the phantom mould, the experimental setup is shown in (b), the post-processed map and generated surface are shown in (c) and (d). The stiffness of the track (red) is successfully distinguished from the surrounding silicone (green).

can successfully distinguish between materials of different stiffness values, thus, it has the potential to detect tumours that are stiffer than the surrounding healthy soft tissue. The obtained colour-coded stiffness map gives a clear-cut representation of the stiffness of the examined area. Furthermore, it can be used to evaluate the stiffness distribution of all the surface. If used for medical diagnosis, it can help clinicians to obtain valuable information about the presence of a mass inside a soft tissue organ. That being so, it can be potentially used for tumour localisation.

CHAPTER 8

Conclusions & Future Work

This chapter summarises and highlights the main achievements of this research. The limitations of the vision-based stiffness sensing mechanism are also identified leading to suggestions for future work.

8.1 Summary of the main findings

This thesis proposed a novel vision-based sensing mechanism for soft tissue stiffness estimation. The following conclusions are drawn:

1. A thorough and consolidated literature was presented to classify sensing devices and technologies for medical diagnosis. The review determined that effective evaluation of the mechanical properties of soft tissues and accurate diagnosis highly depends on the ability of robotic medical instruments to reproduce the sense of touch. Medical imaging and instrumented palpation are novel technologies which aim to replace manual palpation. However, due to some limitations, such as size, costs, ergonomics, real-time requirements, accuracy, precision and compatibility with the medical environments, most of the proposed solutions cannot be used in real applications. There is a need for practical systems which are able to characterise soft tissue stiffness.

2. The proposed sensing mechanism employs several elastic elements to indent soft tissues, and a camera sensor to measure the tissue deformations. Each elastic element is jointly linked to a geometric feature which is enclosed in the camera's field of view. The movements of each elastic element are retrieved by tracking the movements of the correlated feature in the image. Moreover, knowing the elasticity of the embedded element, the interaction force can be calculated by measuring the feature's displacements in the image. Experimental results demonstrate that the model can estimate the interaction force with high accuracy.

3. A mathematical model relies on an image processing algorithm to robustly estimate the soft tissue stiffness as a function of relative forces inferred from the deformation of elastic elements under load.

4. While many of the tactile and force sensors have a subset of desired characteristics, limitations such as repeatability, ease of manufacturing, sterilization and cost, have slowed widespread adoption in clinical settings [78].

   The sensory system described in this thesis measures stiffness mechanically. This system can be adapted and customised for different medical applications where stiffness sensing is likely to play a key role, such as diagnostic palpation of skin or inner body part, teleoperation and medical training. It is easy to use, low-cost, does not use any electronic components and does not require any calibration process, thus can be used as a single-use devices. Additionally, the sensing range and resolution can be easily customised.

5. The literature revealed that most of the proposed diagnostic instruments work only if the orientation of the tool is kept constant during indentation. Thus, such diagnostic instruments cannot be used in real applications. Further exploration of the sensing mechanism has been conducted with the aim to add multi-directional capability to the system. As a result, a multi-directional stiffness probe for diagnostic palpation has been developed. Experimental results showed that the accuracy of stiffness measurements does not depend on the orientation of the probe during the contact.

6. In minimally invasive procedures, long and thin instruments are used to visualise, palpate or operate the anatomical surface. The use of these instruments prevent physicians from directly assessing soft tissues by manual palpation and thus in minimally invasive procedures the sense of touch is completely lost. In order to retrieve touch sensations, researchers have been developing and exploring novel sensing technologies. A solution to the sense of touch issue is yet to be found.

   In view of these technological needs, the developed sensing mechanism has been used to develop a clip-on stiffness sensor for the endoscopic camera. This sensor enhanced the functionality of the endoscopic camera by giving a tool used to visualise anatomical areas the additional function of a diagnostic instrument for tumour localisations. Moreover, the endoscopic camera is already part of the operating theatre equipment, thus the proposed sensor does not require either the introduction of any additional instrument or any additional trocar port. Besides, the developed sensory system is versatile and adaptable to different medical tasks. For instance, detection of blood vessels and differentiation between the artery and vein can be achieved with the developed system.

7. The knowledge of the 3D position of the device is required to compute the stiffness distribution of the overall surface. The multi-directional stiffness probe has been used to generate a global colour-coded stiffness map. The pose of the probe is estimated through both a magnetic tracker and a fixed base robot arm of known kinematics. The magnetic tracker was fixed to the device and used to reconstruct the 3D position of the indenters which are in contact with the soft tissue. The hand-held probe has been used to palpate silicone phantoms of different stiffness values. During this procedure a colour-coded stiffness map was recorded and displayed into a screen. In order to evaluate the performance of the probe in robotic applications, such as teleoperation, the probe was attached to the end-effector of a robot arm and used to palpate the soft tissues while recording the colour-coded stiffness map. Results proved the effectiveness of the stiffness probe in both manual and robotics palpations. The system provides a intuitive user interface for real-time stiffness mapping of the stiffness distribution of anatomical surfaces. The colour-coded

map allows to assess the stiffness distribution of the overall examined area, thus to easily detect abnormalities.

8. Experimental tests with several silicone phantoms showed the accuracy of the stiffness probe in distinguishing between materials presenting different stiffness. A customised phantom, embedding a stiffer track, was used to test the ability of the probe in detecting tumours. Results demonstrate the accuracy of the sensor in discerning between different materials, thus this device can be potentially used for localising tumours.

9. Experimental tests with silicone phantoms demonstrated the effectiveness of the system for in vivo tests.

8.2 Directions for Further Research

The work presented in this thesis creates a base for developing novel stiffness sensory technologies which can serve as the starting point for further research in soft tissue characterization. The limitations of the system provide a basis for future work. More specifically:

1. The cross talk effect between the elastic elements and the boundary condition should be considered and modelled.

2. The design of the sensory mechanisms can be customised and improved in function of the specific application. For instance, the spatial resolution of the multi-directional stiffness probe could be reduced using different springs and reducing the distance between the indenters.

3. Different materials could be explored in order to determine which ones are the most suitable for the beams embedded in the endoscopic camera sensor. Therefore, Finite Element Analysis can be employed to determine the best size of the beams. Furthermore, in order to preserve the visualisation function of the camera, the sensors should not consistently affect the camera field of view.

4. Further validation tests with the designed sensors could be conducted in order to determine the robustness of the sensory system. Besides, tests with medical experts could reveal the ergonomics, practicality and benefit of the sensory system.

5. In this study, linear approximation has been used to model the soft tissue. In order to increase the accuracy of the sensor the soft tissue should be modelled as a inhomogeneous and non-linear viscoelastic material.

6. The design of the cantilever beams integrated into the endoscopic camera should avoid sharp corners which could cut the anatomical areas.

APPENDIX A

Pinhole Camera Model.

The pinhole camera model expresses the mathematical relationship between the coordinates of a 3D point and its projection onto the image plane of an ideal pinhole camera (where the camera aperture is described as a point and no lenses are used to focus light). This geometric mapping is called perspective projection. The pin-hole camera is described by its optical centre **C** (also known as camera projection centre) and the image plane. The distance of the image plane from **C** is the focal length *f*. The line from the camera centre perpendicular to the image plane is called the principal axis or optical axis of the camera. The plane parallel to the image plane containing the optical centre is called the principal plane or focal plane of the camera.

The projection of a 3D world point $(X, Y, Z)^T$ onto the image plane at pixel position $(u, v)^T$can be written as:

$$u = \frac{Xf}{Z} \qquad\qquad v = \frac{Yf}{Z} \tag{A.1}$$

If the world and image points are represented by homogeneous vectors, then perspective projection can be expressed in terms of matrix multiplication as:

$$\lambda \begin{pmatrix} u \\ v \\ 1 \end{pmatrix} = \begin{bmatrix} f & 0 & 0 & 0 \\ 0 & f & 0 & 0 \\ 0 & 0 & f & 0 \\ 0 & 0 & 0 & 1 \end{bmatrix} \begin{pmatrix} X \\ Y \\ Z \\ 1 \end{pmatrix} \tag{A.2}$$

where $\lambda = Z$ is the homogeneous scaling factor.

APPENDIX B

Kalman Filter.

The Kalman filter is an algorithm that operates recursively on streams of noisy input data to produce a statistically optimal estimate of the underlying system state. The algorithm works in two distinct phases: the prediction phase and the update phase. In the prediction phase an estimate of the current state variables is produced along with their uncertainties. This predicted state estimate is also known as the *a priori* state estimate. In the update phase the current *a priori* prediction is combined with the current observation to refine the state estimate. If the state and the control inputs vectors at the time t are $\mathbf{x}_t$ and $\mathbf{u}_t$, and the state transition and the control input matrices are $\mathbf{A}_t$ and $\mathbf{B}_t$, then the vector of the process noise for each parameter in the state vector,$\mathbf{w}_t$, can be drawn from a zero mean multivariate distribution given the covariance matrix $\mathbf{Q}_t$. In this case, Kalman's equations can be used to express the evolution of the state vector $\mathbf{x}_t$ from the prior state $\mathbf{x}_{t\text{-}1}$ as:

$$\mathbf{x}_t = \mathbf{A}_t\mathbf{x}_{t\text{-}1} + \mathbf{B}_t\mathbf{u}_t + \mathbf{w}_t, \tag{B.1}$$

considering the vector of the measurements $\mathbf{z}_t$ the state-measurements transformation matrix $\mathbf{H}_t$ and the observation vector $\mathbf{z}_t$. The measurements of the system can be expressed as:

$$\mathbf{z}_t = \mathbf{H}_t\mathbf{x}_t + \mathbf{v}_t, \tag{B.2}$$

in which the measurement noise has been assumed with zero mean and covariance matrix $\mathbf{R}_t$.

APPENDIX C

The Levenberg-Marquardt Algorithm.

Least squares problems arise when fitting a parameterized function to a set of measured data points by minimizing the sum of the squares of the errors between the data points and the function. Nonlinear least squares is the form of least squares analysis used to fit a set of m observations with a model that is nonlinear in n unknown parameters ($m > n$). The basis of the method is to approximate the model by a linear one and to refine the parameters by successive iterations. The Levenberg-Marquardt algorithm (LMA) is a standard technique used to solve nonlinear least squares problems.

Let the function $f : \mathbb{R}^n \to \mathbb{R}$ be the function to minimize. If f can be written as a sum of squares of the form $f(\mathbf{x}) = \sum_{i=1}^{m}(f_i(\mathbf{x}))^2$, where the functions $f_i : \mathbb{R}^n \to \mathbb{R}$ are linear with respect to $\mathbf{x}$. Least squares, in general, is the problem of finding a vector $\mathbf{x}$ that is a local minimizer of the function f. Which can be stated in matrix form as:

$$\min_{\mathbf{x}} \|F(\mathbf{x})\|^2 \tag{C.1}$$

When at least one of the normal equations of F involves nonlinear functions, closed form-solutions of Equation (C.1) are not always possible. Hence, numerical methods are used to find an approximate solution. These methods are iterative algorithms, i.e. they start from an initial value $\mathbf{x}_0$ which is then iteratively updated. Therefore, an iterative optimization algorithm builds a sequence $\{\mathbf{x}_k\}_{k=1}^{k*}$ that may converge towards a local minimum of the cost function, i.e. $\mathbf{x}_{k*}$ may be close to a local minimum of the solution. With a cost function that has several minima, the initial value $\mathbf{x}_0$ determines which minimum is found. An important aspect of iterative optimization algorithm is the stopping criterion. For the algorithm to be valid, the stopping criterion must be a condition that will be satisfied in a finite and reasonable amount of time. A stopping criterion is usually the combination of several conditions. For instance, one can decide to stop the algorithm when the change in the solution becomes very small, i.e. when

$\|\mathbf{x}_{k+1} - \mathbf{x}_k\| < \varepsilon$ with ε a small fixed constant. A standard stopping criterion is the change in the cost function value: $\|F(\mathbf{x}_{k+1}) - F(\mathbf{x}_k)\| \leq \varepsilon_2$. A maximal number of iterations must also be determined to guarantee that the optimization algorithm will finish in a finite amount of time [142].

The LMA combines the advantages of two minimization methods: the gradient descent method and the Gauss-Newton method, to solve non-linear least squares problems [127]. In the gradient descent method, the sum of the squared errors is reduced by updating the parameters in the steepest-descent direction. In the Gauss-Newton method, the sum of the squared errors is reduced by assuming the least squares function is locally quadratic, and finding the minimum of the quadratic. The LMA acts more like a gradient-descent method when the parameters are far from their optimal value, slow but guaranteed to converge, and acts more like the Gauss-Newton method when the parameters are close to their optimal value [143].

The general update rule of $\mathbf{x}$, generated in one iteration of tan optimization algorithms, is defined as:

$$\mathbf{x}_{k+1} = \mathbf{x}_k + d_k, \tag{C.2}$$

where d_k is a direction of descent. The LMA uses a search direction d that is a solution of the linear set of equations:

$$\left(J(\mathbf{x}_k)^T J(\mathbf{x}_k) + \lambda_k diag(J(\mathbf{x}_k)^T J(\mathbf{x}_k))\right) d_k = -J(\mathbf{x}_k)^T F(\mathbf{x}_k), \tag{C.3}$$

where $J(\mathbf{x}_k)$ is the Jacobian matrix of F evaluated at $\mathbf{x}_k$, $J(\mathbf{x}_k)^T J(\mathbf{x}_k)$ is an approximation of the Hessian matrix and λ_k represents the non-negative damping factor that is adjusted at each iteration to interpolate between the gradient descent and the Newton's method. Using high values for λ favours gradient descent, whereas using lower values favours Newton's method. Thus, the choice of λ in the LMA affects both the search direction and the length of the step d.The value of the damping parameter λ can be updated along with the iterations using different strategies. Typically, if the current λ results in an improvement of the cost function, then the step is applied and λ is divided by a constant v. On the contrary, if the step resulting of the current λ increases of the cost function, the step is discarded and λ is multiplied by v.

APPENDIX D

Stiffness sensor for endoscopic camera: Mechanical drawings of the cantilever prototypes.

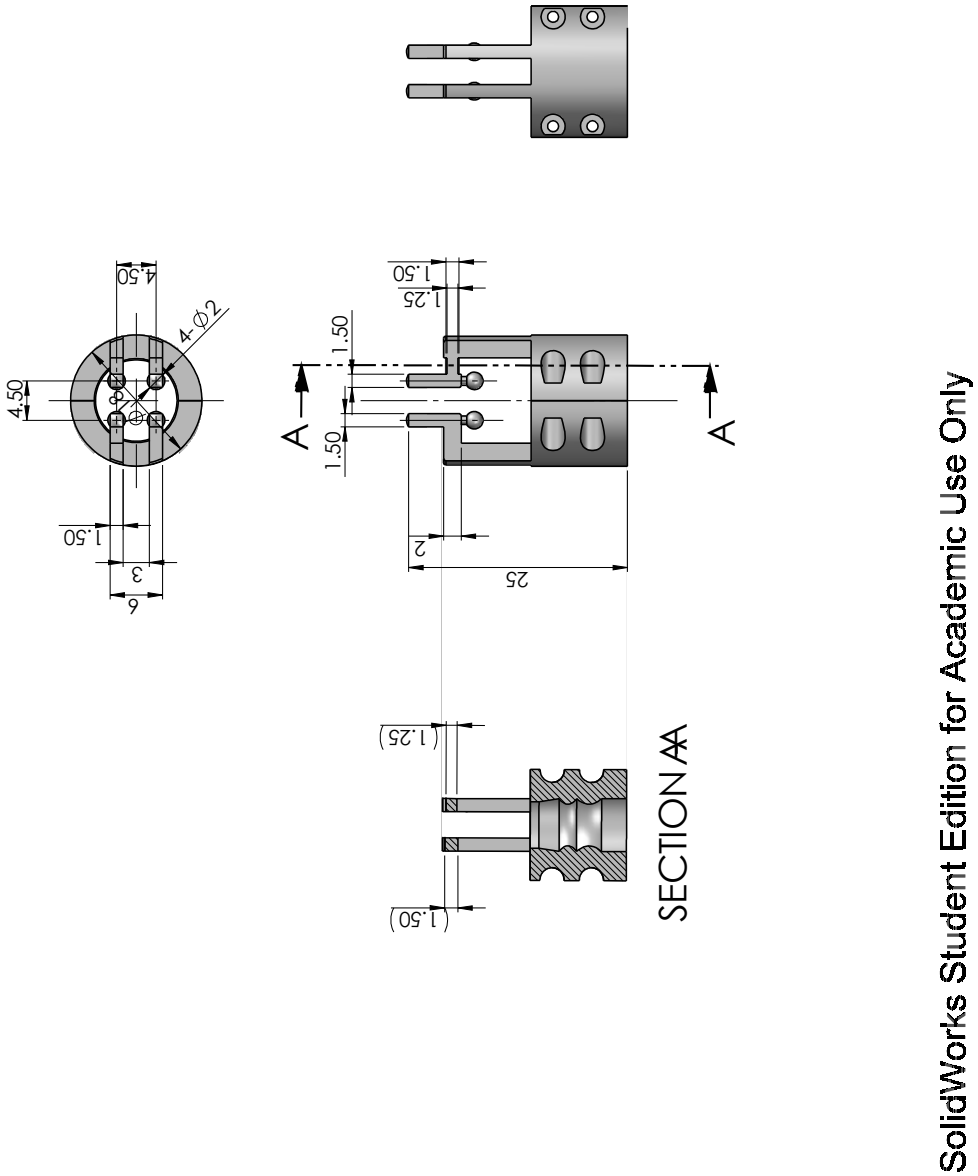

FIGURE D.1: Mechanical drawing of the L-shaped stiffness sensor prototype.

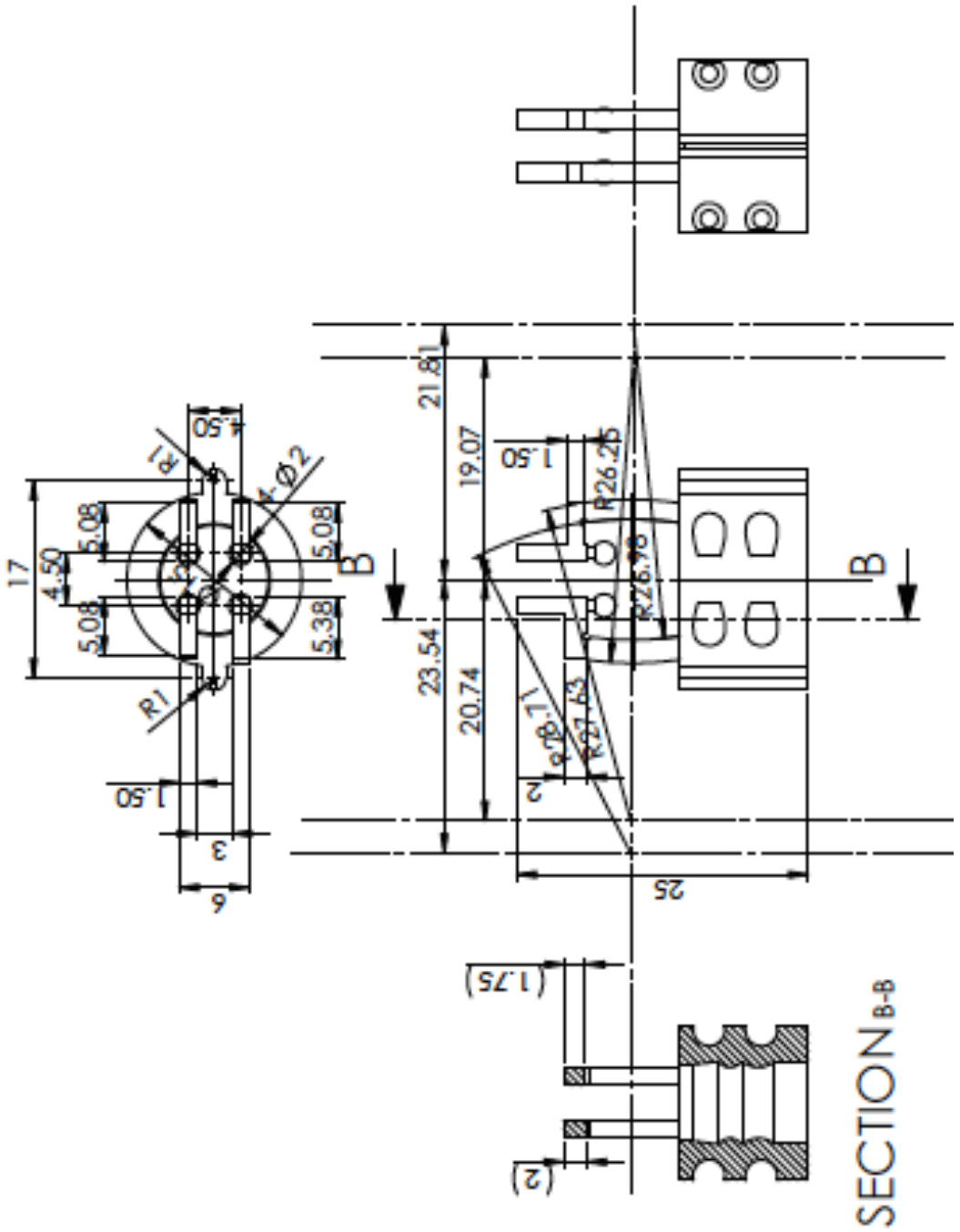
21.81
19.07
23.54
20.74
17
4.50
5.08
5.08
5.08
5.38
1.50
1.50
R1
R1
R26.25
R26.98
R27.63
25
6
3
2
(1.75)
(2)
B
B
SECTION B-B

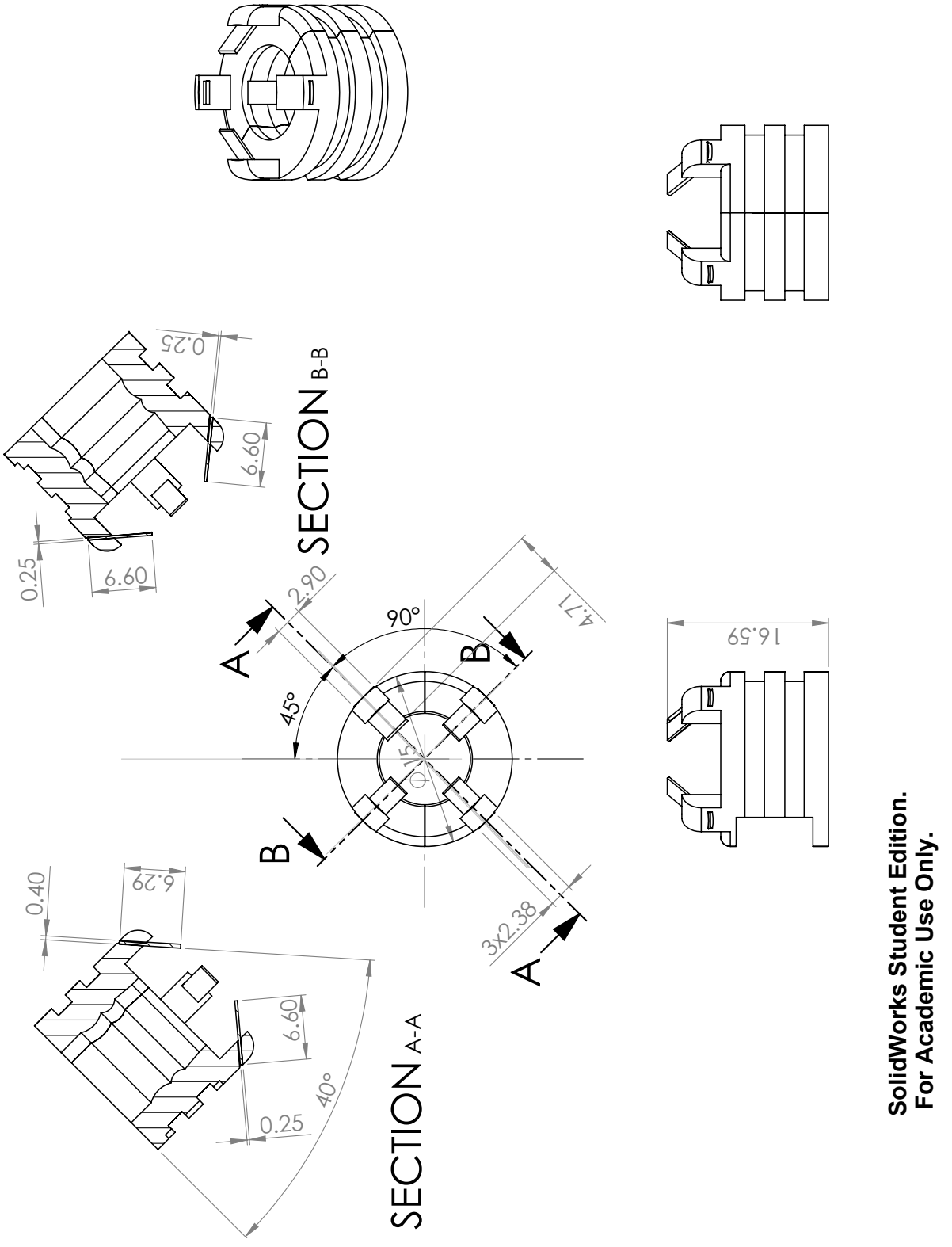

FIGURE D.3: Mechanical drawing of the nitilon cantilever beam stiffness sensor prototype.

References

[1] A. R. Lanfranco, A. E. Castellanos, J. P. Desai, and W. C. Meyers, "Robotic surgery: a current perspective," *Annals of surgery*, vol. 239, no. 1, pp. 14–21, 2004.

[2] D. P. Olson and K. E. Roth, "Journal discussion Diagnostic tools and the hands-on physical examination," *American Medical Association Journal of Ethics*, vol. 9, no. 2, pp. 113–118, 2007.

[3] D. S. Paauw, M. D. Wenrich, J. R. Curtis, J. D. Carline, and P. G. Ramsey, "Ability of primary care physicians to recognize physical findings associated with hiv infection," *Jama*, vol. 274, no. 17, pp. 1380–1382, 1995.

[4] Y. Zhang, R. Phillips, J. Ward, and S. Pisharody, "A survey of simulators for palpation training.," *Studies in health technology and informatics*, vol. 142, pp. 444–446, 2009.

[5] T. GH, G. H, and R. CC, "Solitary thyroid nodule: Comparison between palpation and ultrasonography," *Archives of Internal Medicine*, vol. 155, no. 22, pp. 2418–2423, 1995.

[6] A. Manduca, T. E. Oliphant, M. A. Dresner, J. L. Mahowald, S. A. Kruse, E. Amromin, J. P. Felmlee, J. F. Greenleaf, and R. L. Ehman, "Magnetic resonance elastography: Non-invasive mapping of tissue elasticity," *Medical Image Analysis*, vol. 5, pp. 237–254, May 2015.

[7] S. Phipps, T. Yang, F. Habib, R. Reuben, and S. McNeill, "Measurement of tissue mechanical characteristics to distinguish between benign and malignant prostatic disease," *Urology*, vol. 66, no. 2, pp. 447 – 450, 2005.

[8] V. Jalkanen, B. Andersson, A. Bergh, B. Ljungberg, and O. Lindahl, "Prostate tissue stiffness as measured with a resonance sensor system: a study on silicone and human prostate tissue in vitro," *Medical and Biological Engineering and Computing*, vol. 44, no. 7, pp. 593–603, 2006.

[9] S. M. Hosseini, S. M. T. Kashani, S. Najarian, F. Panahi, S. M. M. Naeini, and A. Mojra, "A medical tactile sensing instrument for detecting embedded objects, with specific application for breast examination," *The international journal of medical robotics and computer assisted surgery*, vol. 6, no. 1, pp. 73–82, 2010.

[10] A. Hughes-Hallett, E. K. Mayer, P. J. Pratt, J. A. Vale, and A. W. Darzi, "Quantitative analysis of technological innovation in minimally invasive surgery," *British Journal of Surgery*, vol. 102, no. 2, pp. 151–157, 2015.

[11] T. R. Stanton and G. N. Kawchuk, "Reliability of assisted indentation in measuring lumbar spinal stiffness," *Manual Therapy*, vol. 14, no. 2, pp. 197 – 205, 2009.

[12] A. Vexler, I. Polyansky, and R. Gorodetsky, "Evaluation of skin viscoelasticity and anisotropy by measurement of speed of shear wave propagation with viscoelasticity skin analyzer," *Journal of Investigative Dermatology*, vol. 113, no. 5, pp. 732–739, 1999.

[13] L. H. Cohn, D. H. Adams, G. S. Couper, D. P. Bichell, D. M. Rosborough, S. P. Sears, and S. F. Aranki, "Minimally invasive cardiac valve surgery improves patient satisfaction while reducing costs of cardiac valve replacement and repair.," *Annals of surgery*, vol. 226, pp. 421–6; discussion 427–8, Oct. 1997.

[14] S. A. Darzi and Y. Munz, "The impact of minimally invasive surgical techniques.," *Annual review of medicine*, vol. 55, pp. 223–37, Jan. 2004.

[15] J. C. Hu, Q. Wang, C. L. Pashos, S. R. Lipsitz, and N. L. Keating, "Utilization and outcomes of minimally invasive radical prostatectomy.," *Journal of clinical oncology : official journal of the American Society of Clinical Oncology*, vol. 26, pp. 2278–84, May 2008.

[16] H. Stassen, J. Dankelman, and C. Grimbergen, "Developments in Minimally Invasive Surgery and Interventional Techniques (MISIT)," *Conference on human decision making and manual control*, pp. 212–218, 1997.

[17] J. Whynott, "The critical questions when micromolding for an mis device," *Medical Design Technology*, 2010.

[18] M. Beccani, C. D. Natali, C. E. Benjamin, C. S. Bell, N. E. Hall, and P. Valdastri, "Wireless tissue palpation: Head characterization to improve tumor detection in soft tissue," *Sensors and Actuators A: Physical*, vol. 223, pp. 180 – 190, 2015.

[19] M. A. van Veelen, E. A. L. Nederlof, R. H. M. Goossens, C. J. Schot, and J. J. Jakimowicz, "Ergonomic problems encountered by the medical team related to products

used for minimally invasive surgery," *Surgical Endoscopy And Other Interventional Techniques*, vol. 17, no. 7, pp. 1077–1081, 2003.

[20] T. Wilson and R. Torrey, "Open versus robotic-assisted radical prostatectomy: which is better?," *Current Opinion in Urology*, vol. 21 (3), pp. 200–205, 2011.

[21] W. Ji, Z. Zhao, J. Dong, H. Wang, F. Lu, and H. Lu, "One-stage robotic-assisted laparoscopic cholecystectomy and common bile duct exploration with primary closure in 5 patients," *Surgical Laparoscopy Endoscopy Percutaneous Techniques*, vol. 21 (2), pp. 123–126, 2011.

[22] P. Zehnder and I. S. Gill, "Cost-effectiveness of open versus laparoscopic versus robotic-assisted laparoscopic cystectomy and urinary diversion," *Current Opinion in Urology*, vol. 21 (5), pp. 415–419, 2011.

[23] M. E. Currie, J. Romsa, S. Fox, W. Vezina, C. Akincioglu, J. Warrington, R. McClure, L. Stit, A. Menkis, W. Boyd, and B. Kiaii, "Long-term angiographic follow-up of robotic-assisted coronary artery revascularization," *The Annals of Thoracic Surgery*, vol. 93 (5), pp. 1426–1431, 2012.

[24] S. Masroor, C. Plambeck, and M. Dahnert, "Complex repair of a barlows valve using the da vinci robotic surgical system," *ISOs Work on Guidance for Haptic and Tactile Interactions*, vol. 19 (5), pp. 593–595, 2010.

[25] T. Coles, D. Meglan, and N. John, "The role of haptics in medical training simulators: A survey of the state of the art," *Haptics, IEEE Transactions on*, vol. 4, pp. 51–66, Jan 2011.

[26] D. M. Herron and M. Marohn, "A consensus document on robotic surgery.," *Surgical endoscopy*, vol. 22, pp. 313–25; discussion 311–2, Feb. 2008.

[27] N. Alt, Q. Rao, and E. Steinbach, "Haptic exploration for navigation tasks using a visuo-haptic sensor," in *Interactive Perception Workshop, ICRA 2013*, (Karlsruhe, Germany), May 2013.

[28] A. P. Advincula and K. Wang, "Evolving role and current state of robotics in minimally invasive gynecologic surgery," *Journal of Minimally Invasive Gynecology*, vol. 16, no. 3, pp. 291 – 301, 2009.

[29] A. L. Trejos, R. V. Patel, and M. D. Naish, "Force sensing and its application in minimally invasive surgery and therapy: a survey," *Proceedings of the Institution of Mechanical Engineers, Part C: Journal of Mechanical Engineering Science*, vol. 224, pp. 1435–1454, Jan. 2010.

[30] N. Enayati, E. De Momi, and G. Ferrigno, "Haptics in robot-assisted surgery: Challenges and benefits," 2016.

[31] H. Oflaz and O. Baran, "A new medical device to measure a stiffness of soft materials," *Acta of Bioengineering and Biomechanics*, vol. 16, no. 1, pp. 125–131, 2014.

[32] J. T. Iivarinen, R. K. Korhonen, and J. S. Jurvelin, "Experimental and numerical analysis of soft tissue stiffness measurement using manual indentation device - significance of indentation geometry and soft tissue thickness," *Skin Research and Technology*, vol. 20, no. 3, pp. 347–354, 2014.

[33] H. Liu, J. Li, X. Song, L. Seneviratne, and K. Althoefer, "Rolling indentation probe for tissue abnormality identification during minimally invasive surgery," *Robotics, IEEE Transactions on*, vol. 27, no. 3, pp. 450–460, 2011.

[34] J. Rosen, B. Hannaford, M. P. MacFarlane, and M. N. Sinanan, "Force controlled and teleoperated endoscopic grasper for minimally invasive surgery–experimental performance evaluation.," *IEEE transactions on bio-medical engineering*, vol. 46, pp. 1212–21, Oct. 1999.

[35] J. Li, H. Liu, K. Althoefer, and L. D. Seneviratne, "A stiffness probe based on force and vision sensing for soft tissue diagnosis.," *Conference proceedings: Annual International Conference of the IEEE Engineering in Medicine and Biology Society. IEEE Engineering in Medicine and Biology Society. Conference*, vol. 2012, pp. 944–7, Jan. 2012.

[36] V. Ficarra, S. Cavalleri, G. Novara, M. Aragona, and W. Artibani, "Evidence from robot-assisted laparoscopic radical prostatectomy: A systematic review," *European Urology*, vol. 51, no. 1, pp. 45 – 56, 2007.

[37] C. Abbou, A. Hoznek, L. Salomon, L. Olsson, and A. Lobontiu, "Laparoscopic radical prostatectomy with a remote controlled robot," *The Journal of Urology*, vol. 165, pp. 1964–1966, 2001.

[38] R. Etzioni, N. Urban, S. Ramsey, M. McIntosh, S. Schwartz, B. Reid, J. Radich, G. Anderson, and L. Hartwell, "The case for early detection," *Nature Reviews Cancer*, vol. 3, no. 4, pp. 243–252, 2003.

[39] V. Swaminathan, K. Mythreye, E. T. O'Brien, A. Berchuck, G. C. Blobe, and R. Superfine, "Mechanical stiffness grades metastatic potential in patient tumor cells and in cancer cell lines," *Cancer Research*, vol. 71, no. 15, pp. 5075–5080, 2011.

[40] N. Forrest, S. Baillie, and H. Z. Tan, "Haptic stiffness identification by veterinarians and novices: A comparison," in *EuroHaptics conference, 2009 and Symposium on Haptic Interfaces for Virtual Environment and Teleoperator Systems. World Haptics 2009. Third Joint*, pp. 646–651, IEEE, 2009.

[41] J. Konstantinova, M. Li, G. Mehra, P. Dasgupta, K. Althoefer, and T. Nanayakkara, "Characteristics of manual palpation to localize hard nodules in soft tissues,"

[42] S. McDonald, D. Saslow, and M. H. Alciati, "Performance and reporting of clinical breast examination: a review of the literature," *CA: a cancer journal for clinicians*, vol. 54, no. 6, pp. 345–361, 2004.

[43] J. Eck, A. L. Kaas, and R. Goebel, "Crossmodal interactions of haptic and visual texture information in early sensory cortex," *NeuroImage*, vol. 75, pp. 123 – 135, 2013.

[44] S. Lacey and K. Sathian, "Chapter 11 - multisensory object representation: Insights from studies of vision and touch," in *Enhancing Performance for Action and PerceptionMultisensory Integration, Neuroplasticity and Neuroprosthetics, Part I* (J. F. K. Andrea M. Green, C. Elaine Chapman and F. Lepore, eds.), vol. 191 of *Progress in Brain Research*, pp. 165 – 176, Elsevier, 2011.

[45] K. Sathian and Z. A., "Feeling with the mind's eye: the role of visual imagery in tactile perception.," *Optom Vis Sci*, vol. 78, no. 5, pp. 276–281, 2001.

[46] A. Mechelli, C. J. Price, K. J. Friston, and A. Ishai, "Where bottom-up meets top-down: Neuronal interactions during perception and imagery," *Cerebral Cortex*, vol. 14, no. 11, pp. 1256–1265, 2004.

[47] K. Meyer, J. T. Kaplan, R. Essex, H. Damasio, and A. Damasio, "Seeing touch is correlated with content-specific activity in primary somatosensory cortex," *Cerebral Cortex*, vol. 21, no. 9, pp. 2113–2121, 2011.

[48] J. C. Snow, L. Strother, and G. W. Humphreys, "Haptic shape processing in visual cortex," *Journal of Cognitive Neuroscience*, vol. 26, pp. 1154–1167, 2016/01/18 2013.

[49] S. J. Lederman and R. L. Klatzky, "Hand movements: a window into haptic object recognition.," *Cognit Psychol*, vol. 19, pp. 342–368, July 1987.

[50] R. Dahiya, G. Metta, M. Valle, and G. Sandini, "Tactile sensin - from humans to humanoids," *Robotics, IEEE Transactions on*, vol. 26, pp. 1–20, Feb 2010.

[51] H. Yousef, M. Boukallel, and K. Althoefer, "Tactile sensing for dexterous in-hand manipulation in robotics—a review," *Sensors and Actuators A: Physical*, vol. 167, no. 2, pp. 171 – 187, 2011. Solid-State Sensors, Actuators and Microsystems Workshop.

[52] P. Saccomandi, E. Schena, C. M. Oddo, L. Zollo, S. Silvestri, and E. Guglielmelli, "Microfabricated tactile sensors for biomedical applications: A review," *Biosensors*, vol. 4, no. 4, pp. 422–448, 2014.

[53] S. Najarian, J. Dargahi, and A. Mehrizi, *Artificial tactile sensing in biomedical engineering*. McGraw Hill Professional, 2009.

[54] D. De Rossi, "Artificial tactile sensing and haptic perception," *Measurement Science and Technology*, vol. 2, no. 11, p. 1003, 1991.

[55] R. Ayres and S. Miller, *Robotics: Applications and social implications*. World Future Society,Bethesda, MD, Jan 1983.

[56] A. Shukla, A. Shukla, and R. Tiwari, *Intelligent Medical Technologies and Biomedical Engineering: Tools and Applications*. Hershey, PA: Information Science Reference - Imprint of: IGI Publishing, 2010.

[57] M. M. Lirici, V. Papaspyropoulos, and L. Angelini, "Telerobotics in medicine and surgery," *Minimally Invasive Therapy & Allied Technologies*, vol. 6, no. 5-6, pp. 364–378, 1997.

[58] J. Ward and T. Wright, "Sensory substitution as an artificially acquired synaesthesia," *Neuroscience & Biobehavioral Reviews*, vol. 41, pp. 26–35, 2014.

[59] C. Pacchierotti, D. Prattichizzo, and K. J. Kuchenbecker, "Cutaneous feedback of fingertip deformation and vibration for palpation in robotic surgery," *IEEE Transactions on Biomedical Engineering*, vol. 63, no. 2, pp. 278–287, 2016.

[60] A. Sarvazyan, "Computerized palpation is more sensitive than human finger," in *Proceedings of the 12th International Symposium on Biomedical Measurements and Instrumentation*, pp. 523–24, 1998.

[61] G. Y. Tan, R. K. Goel, J. H. Kaouk, and A. K. Tewari, "Technological advances in robotic-assisted laparoscopic surgery," *Urologic Clinics of North America*, vol. 36, no. 2, pp. 237–249, 2009.

[62] J. Gwilliam, Z. Pezzementi, E. Jantho, A. Okamura, and S. Hsiao, "Human vs. robotic tactile sensing: Detecting lumps in soft tissue," in *Haptics Symposium, 2010 IEEE*, pp. 21–28, March 2010.

[63] L. Sallaway, S. Magee, J. Shi, O. Lehmann, F. Quivira, K. Tgavalekos, D. Brooks, S. Muftu, W. Meleis, R. Moore, D. Kopans, and K.-T. Wan, "Detecting solid masses in phantom breast using mechanical indentation," *Experimental Mechanics*, vol. 54, no. 6, pp. 935–942, 2014.

[64] R. Hoffmann, "Laparoscopic laser cholecystectomy," *Therapeutische Umschau. Revue thérapeutique*, vol. 50, pp. 582–7, Aug. 1993.

[65] S. R. Kovac, H. Cruikshank, and H. F. RETTO, "Laparoscopy-assisted vaginal hysterectomy," *Jornal of Gynaecology Surgery*, vol. 6, no. 3, pp. 185–193, 2009.

[66] S. Schostek, M. O. Schurr, and G. F. Buess, "Review on aspects of artificial tactile feedback in laparoscopic surgery," *Medical Engineering & Physics*, vol. 31, no. 8, pp. 887 – 898, 2009.

[67] B. Morris, "Robotic surgery: applications, limitations, and impact on surgical education," *Medscape General Medicine*, vol. 7, no. 3, p. 72, 2005.

[68] A. M. Okamura, "Haptic feedback in robot-assisted minimally invasive surgery," *Current opinion in urology*, vol. 19, pp. 102–107, 01 2009.

[69] R. M. Pierce, "Increasing transparency and presence in teleoperation through human-centered design," 2015.

[70] J. Marescaux, J. Leroy, F. Rubino, M. Smith, M. Vix, M. Simone, and D. Mutter, "Transcontinental robot-assisted remote telesurgery: feasibility and potential applications," *Annals of surgery*, vol. 235, no. 4, pp. 487–492, 2002.

[71] S. Suzuki, N. Suzuki, M. Hayashibe, A. Hattori, K. Konishi, Y. Kakeji, and M. Hashizume, "Tele-surgical simulation system for training in the use of da vinci surgery.," *Studies in health technology and informatics*, vol. 111, pp. 543–548, 2004.

[72] G. H. Ballantyne, "Robotic surgery, telerobotic surgery, telepresence and telementoring," *Surgical Endoscopy and Other Interventional Techniques*, vol. 16, no. 10, pp. 1389–1402, 2002.

[73] D. B. Camarillo, T. M. Krummel, and J. K. Salisbury, "Robotic technology in surgery: past, present, and future," *The American Journal of Surgery*, vol. 188, no. 4, pp. 2–15, 2004.

[74] J. V. Frangioni, "New technologies for human cancer imaging," *Journal of Clinical Oncology*, vol. 26, no. 24, p. 4012, 2008.

[75] P. Puangmali, H. Liu, L. D. Seneviratne, P. Dasgupta, and K. Althoefer, "Miniature 3-axis distal force sensor for minimally invasive surgical palpation," *IEEEASME Transactions on Mechatronics*, vol. 17, no. 4, pp. 1–11, 2011.

[76] H. Yegingil, W. Y. Shih, and W.-H. Shih, "Probing model tumor interfacial properties using piezoelectric cantilevers," *Review of Scientific Instruments*, vol. 81, no. 9, 2010.

[77] J. Fu, X. Zhou, and F. Li, "An adaptive nanoindentation system based on electric bending of a piezoelectric cantilever," *Sensors and Actuators A: Physical*, vol. 216, pp. 249 – 256, 2014.

[78] J. Konstantinova, A. Jiang, K. Althoefer, P. Dasgupta, and T. Nanayakkara, "Implementation of tactile sensing for palpation in robot-assisted minimally invasive surgery: A review," *IEEE SENSORS JOURNAL*, vol. 14, no. 8, pp. 2490–2501, 2014.

[79] J. P. A. Arokoski, J. Surakka, T. Ojala, P. Kolari, and J. S. Jurvelin, "Feasibility of the use of a novel soft tissue stiffness meter," *Physiological Measurement*, vol. 26, no. 3, p. 215, 2005.

[80] J. Kim, *Vision-Based Haptic Feedback with Physically-Based Model for Telemanipulation*. INTECH Open Access Publisher, 2010.

[81] P. Valdastri, K. Harada, A. Menciassi, L. Beccai, C. Stefanini, M. Fujie, and P. Dario, "Integration of a miniaturised triaxial force sensor in a minimally invasive surgical tool," *Biomedical Engineering, IEEE Transactions on*, vol. 53, pp. 2397–2400, Nov 2006.

[82] M. Tavakoli, R. V. Patel, and M. Moallem, "A force reflective master-slave system for minimally invasive surgery," in *Intelligent Robots and Systems, 2003.(IROS 2003). Proceedings. 2003 IEEE/RSJ International Conference on*, vol. 4, pp. 3077–3082, IEEE, 2003.

[83] G. Tholey, A. Pillarisetti, and J. P. Desai, "On site three dimensional force sensing capability in a laparoscopic grasper," *Industrial Robot: An International Journal*, vol. 31, no. 6, pp. 509–518, 2004.

[84] R. Konietschke, U. Hagn, M. Nickl, S. Jorg, A. Tobergte, G. Passig, U. Seibold, L. Le-Tien, B. Kubler, M. Groger, F. Frohlich, C. Rink, A. Albu-Schaffer, M. Grebenstein, T. Ortmaier, and G. Hirzinger, "The dlr mirosurge - a robotic system for surgery," in *Robotics and Automation, 2009. ICRA '09. IEEE International Conference on*, pp. 1589–1590, May 2009.

[85] Y. Noh, S. Sareh, J. Back, H. Wurdemann, T. Ranzazni, E. Secco, A. Faragasso, H. Liu, and K. Althoefer, "A three-axial body force sensor for flexible manipulators," *IEEE International Conference on Robotics and Automation*, 2014.

[86] Y. Noh, S. Sareh, H. Wurdemann, H. Liu, J. Back, J. Housden, K. Rhode, and K. Althoefer, "Three-axis fiber-optic body force sensor for flexible manipulators," *Sensors Journal, IEEE*, vol. PP, no. 99, pp. 1–1, 2015.

[87] M. C. Yip, S. G. Yuen, and R. D. Howe, "A robust uniaxial force sensor for minimally invasive surgery.," *IEEE transactions on bio-medical engineering*, vol. 57, pp. 1008–11, May 2010.

[88] H. Liu, D. P. Noonan, B. J. Challacombe, P. Dasgupta, L. D. Seneviratne, and K. Althoefer, "Rolling mechanical imaging for tissue abnormality localization during minimally invasive surgery.," *IEEE transactions on bio-medical engineering*, vol. 57, pp. 404–14, Feb. 2010.

[89] D. Zbyszewski, P. Polygerinos, L. Seneviratne, and K. Althoefer, "A novel mri compatible air-cushion tactile sensor for minimally invasive surgery," in *Intelligent Robots and Systems, 2009. IROS 2009. IEEE/RSJ International Conference on*, pp. 2647–2652, Oct 2009.

[90] P. Puangmali, H. Liu, L. D. Seneviratne, P. Dasgupta, and K. Althoefer, "Miniature 3-axis distal force sensor for minimally invasive surgical palpation," *Mechatronics, IEEE/ASME Transactions on*, vol. 17, no. 4, pp. 646–656, 2012.

[91] M. Lee and H. Nicholls, "Review article tactile sensing for mechatronics?a state of the art survey," *Mechatronics*, vol. 9, no. 1, pp. 1 – 31, 1999.

[92] S. Ullrich and T. Kuhlen, "Haptic palpation for medical simulation in virtual environments," *IEEE Transactions on Visualization and Computer Graphics*, vol. 18, no. 4, pp. 617–625, 2012.

[93] A. M. R. F. E. Bab, T. Tamura, K. Sugano, T. Tsuchiya, O. Tabata, M. E. H. Eltaib, and M. M. Sallam, "Design and simulation of a tactile sensor for soft-tissue compliance detection," *IEEJ Transactions on Sensors and Micromachines*, vol. 128, no. 5, pp. 186–192, 2008.

[94] A. Fath El Bab, K. Sugano, T. Tsuchiya, O. Tabata, M. Eltaib, and M. Sallam, "Micromachined tactile sensor for soft-tissue compliance detection," *Microelectromechanical Systems, Journal of*, vol. 21, pp. 635–645, June 2012.

[95] C. M. N. de Jesus, L. A. Corrêa, and C. R. Padovani, "Complications and risk factors in transrectal ultrasound-guided prostate biopsies ," 2006.

[96] E. Frei, B. Sollish, and S. Yerushalmi, "Instrument for viscoelastic measurement," Mar. 20 1979. US Patent 4,144,877.

[97] S. Omata and Y. Terunuma, "Development of new type tactile sensor for detecting hardness and/or software of an object like the human hand," in *Solid-State Sensors and Actuators, 1991. Digest of Technical Papers, TRANSDUCERS '91., 1991 International Conference on*, pp. 868–871, June 1991.

[98] Y. Murayama and S. Omata, "Considerations in the design and sensitivity optimization of the micro tactile sensor," *Ultrasonics, Ferroelectrics, and Frequency Control, IEEE Transactions on*, vol. 52, pp. 434–438, March 2005.

[99] J. Dargahi, S. Najarian, V. Mirjalili, and B. Liu, "Modelling and testing of a sensor capable of determining the stiffness of biological tissues," *Electrical and Computer Engineering, Canadian Journal of*, vol. 32, pp. 45–51, Winter 2007.

[100] P. Peng, a. S. Sezen, R. Rajamani, and a. G. Erdman, "Novel MEMS stiffness sensor for in-vivo tissue characterization measurement.," *Conference proceedings: Annual International Conference of the IEEE Engineering in Medicine and Biology Society. IEEE Engineering in Medicine and Biology Society. Conference*, vol. 2009, pp. 6640–3, Jan. 2009.

[101] P. N. Wells and H.-D. Liang, "Medical ultrasound: imaging of soft tissue strain and elasticity," *Journal of the Royal Society Interface*, vol. 8, no. 64, pp. 1521–1549, 2011.

[102] K. J. Parker, L. S. Taylor, S. Gracewski, and D. J. Rubens, "A unified view of imaging the elastic properties of tissue," *The Journal of the Acoustical Society of America*, vol. 117, no. 5, pp. 2705–2712, 2005.

[103] D. L. Cochlin, R. Ganatra, and D. Griffiths, "Elastography in the detection of prostatic cancer," *Clinical radiology*, vol. 57, no. 11, pp. 1014–1020, 2002.

[104] A. Sarvazyan, T. J. Hall, M. W. Urban, M. Fatemi, S. R. Aglyamov, and B. S. Garra, "An overview of elastography–an emerging branch of medical imaging," *Current medical imaging reviews*, vol. 7, no. 4, p. 255, 2011.

[105] R. Cao, Z. Huang, T. Varghese, and G. Nabi, "Tissue mimicking materials for the detection of prostate cancer using shear wave elastography: A validation study," *Medical physics*, vol. 40, no. 2, p. 022903, 2013.

[106] E. Szczepanek-Parulska, K. Woliński, A. Stangierski, E. Gurgul, M. Biczysko, P. Majewski, M. Rewaj-Łosyk, and M. Ruchała, "Comparison of diagnostic value of conventional ultrasonography and shear wave elastography in the prediction of thyroid lesions malignancy," *PloS one*, vol. 8, no. 11, p. e81532, 2013.

[107] D. Junker, G. Schäfer, F. Aigner, P. Schullian, L. Pallwein-Prettner, J. Bektic, W. Horninger, E. J. Halpern, and F. Frauscher, "Potentials and limitations of real-time elastography for prostate cancer detection: a whole-mount step section analysis," *The Scientific World Journal*, vol. 2012, 2012.

[108] J. B. Osborn, P. A. Lenton, S. A. Lunos, and C. M. Blue, "Endoscopic vs. tactile evaluation of subgingival calculus," *American Dental Hygienists Association*, vol. 88, no. 4, pp. 229–236, 2014.

[109] T. Kawahara and M. Kaneko, "Non-contact stiffness imager for medical application," in *Information Acquisition, 2005 IEEE International Conference on*, pp. 6–pp, IEEE, 2005.

[110] J. Li, H. Liu, K. Althoefer, and L. Seneviratne, "A stiffness probe for soft tissue abnormality identification during laparoscopic surgery," in *World Automation Congress (WAC), 2012*, pp. 1–6, June 2012.

[111] K. Takashima, K. Yoshinaka, and K. Ikeuchi, "Vision-based tactile sensor for endoscopy," in *Complex Medical Engineering* (J. Wu, K. Ito, S. Tobimatsu, T. Nishida, and H. Fukuyama, eds.), pp. 13–23, Springer Japan, 2007.

[112] T. Iwai, T. Koyama, H. Kagawa, T. Yoneyama, and T. Watanabe, "Visualization method based stiffness sensing system for endoscopes," in *Engineering in Medicine and Biology Society (EMBC), 2015 37th Annual International Conference of the IEEE*, pp. 6449–6452, Aug 2015.

[113] T. Iwai, Y. Fujihira, L. Wakako, H. Kagawa, T. Yoneyama, and T. Watanabe, "Three-axis force visualizing system for fiberscopes utilizing highly elastic fabric," in *Advanced Intelligent Mechatronics (AIM), 2014 IEEE/ASME International Conference on*, pp. 1110–1115, July 2014.

[114] T. Watanabe, T. Iwai, Y. Fujihira, L. Wakako, H. Kagawa, and T. Yoneyama, "Force sensor attachable to thin fiberscopes/endoscopes utilizing high elasticity fabric," *Sensors*, vol. 14, no. 3, pp. 5207–5220, 2014.

[115] Y. C. Fung, "Biomechanics: Mechanical Properties of Living Tissues," *Springer*, Dec. 1993.

[116] J. Bimbo, L. Seneviratne, K. Althoefer, and H. Liu, "Combining touch and vision for the estimation of an object's pose during manipulation," in *Intelligent Robots and Systems (IROS), 2013 IEEE/RSJ International Conference on*, pp. 4021–4026, Nov 2013.

[117] B. Frank, R. Schmedding, C. Stachniss, M. Teschner, and W. Burgard, "Learning the elasticity parameters of deformable objects with a manipulation robot," in *Intelligent Robots and Systems (IROS), 2010 IEEE/RSJ International Conference on*, pp. 1877–1883, Oct 2010.

[118] D. Stoyanov, "Surgical vision," *Annals of biomedical engineering*, vol. 40, no. 2, pp. 332–345, 2012.

[119] P. Valdastri, M. Simi, and R. J. Webster, "Advanced technologies for gastrointestinal endoscopy.," *Annual review of biomedical engineering*, vol. 14, pp. 397–429, Jan. 2012.

[120] J. Mitchell, "Endoscopy," *Annal of the Royal College of Surgeon of England*, vol. 62, pp. 106–111, 19780.

[121] T. V. Evreinova, G. Evreinov, and R. Raisamo, "From Kinesthetic Sense to New Interaction Concepts: Feasibility and Constraints," *International Journal of Advanced Computer Technology*, vol. 3, no. 4, pp. 1–33, 2014.

[122] A. Sarvazyan, V. Egorov, and N. Sarvazyan, "Tactile sensing and tactile imaging in detection of cancer," *Biosensors and Molecular Technologies for Cancer Diagnostics*, p. 337, 2012.

[123] A. Khalil, B. Bouma, and M. Kaazempur Mofrad, "A combined fem/genetic algorithm for vascular soft tissue elasticity estimation," *Cardiovascular Engineering*, vol. 6, no. 3, pp. 93–102, 2006.

[124] R. Muthupillai, D. Lomas, P. Rossman, J. Greenleaf, A. Manduca, and R. Ehman, "Magnetic resonance elastography by direct visualization of propagating acoustic strain waves," *Science*, vol. 269, no. 5232, pp. 1854–1857, 1995.

[125] Y. K. Mariappan, P. J. Rossman, K. J. Glaser, A. Manduca, and R. L. Ehman, "Magnetic resonance elastography with a phased-array acoustic driver system," *Magnetic Resonance in Medicine*, vol. 61, no. 3, pp. 678–685, 2009.

[126] A. Faragasso, A. Stilli, J. Bimbo, Y. Noh, H. Liu, T. Nanayakkara, P. Dasgupta, H. A. Wurdemann, and K. Althoefer, "Endoscopic add-on stiffness probe for real-time soft surface characterisation in mis," *IEEE Engineering in Medicine and Biology Society (EMBC)*, 2014.

[127] M. I. a. Lourakis, "A Brief Description of the Levenberg-Marquardt Algorithm Implemened by levmar," *Matrix*, vol. 3, p. 2, 2005.

[128] P. Bettess, "The finite element method vol. 1: Basic formulation and linear problems, fourth edition by o. c. zienkiewicz and r. l. taylor, mcgraw-hill, maidenhead, england, 1989. no. of pages: 648.," *International Journal for Numerical Methods in Engineering*, vol. 30, no. 3, pp. 565–567, 1990.

[129] C. Laugier, C. Mendoza, and K. Sundaraj, "Towards a realistic medical simulator using virtual environments and haptic interaction," *In Proc. of the International Symposium in Reserach Robotics, Sidney (AU*, 2001.

[130] Y. Fung, *Biomechanics: Mechanical properties of living tissue*. New York: Springer-Verlag, 1993.

[131] N. Huber, D. Munz, and C. Tsakmakis, "Determination of young's modulus by spherical indentation," *Journal of materials research*, vol. 12, no. 9, pp. 2459–2469, 1997.

[132] W. C. Oliver and G. M. Pharr, "Measurement of hardness and elastic modulus by instrumented indentation: Advances in understanding and refinements to methodology," *Journal of materials research*, vol. 19, no. 01, pp. 3–20, 2004.

[133] T. Nakayoshi, H. Tajiri, K. Matsuda, M. Kaise, M. Ikegami, and H. Sasaki, "Magnifying endoscopy combined with narrow band imaging system for early gastric cancer: correlation of vascular pattern with histopathology (including video)," *Endoscopy*, vol. 36, p. 1080—1084, December 2004.

[134] R. Shahidi, M. Bax, J. Maurer, C.R., J. Johnson, E. Wilkinson, B. Wang, J. West, M. Citardi, K. Manwaring, and R. Khadem, "Implementation, calibration and accuracy testing of an image-enhanced endoscopy system," *Medical Imaging, IEEE Transactions on*, vol. 21, pp. 1524–1535, Dec 2002.

[135] N. Tanigawa, "Advantages and Problems with Endoscopic," vol. 137, no. 9, pp. 1833–1837, 2009.

[136] B. E. Schneider, "Advanced therapy in minimally invasive surgery," *Annals of Surgery*, vol. 244, no. 5, p. 837, 2006.

[137] H. Liu, P. Puangmali, D. Zbyszewski, O. Elhage, P. Dasgupta, J. S. Dai, L. Seneviratne, and K. Althoefer, "An indentation depth–force sensing wheeled probe for abnormality identification during minimally invasive surgery," *Proceedings of the Institution of Mechanical Engineers, Part H: Journal of Engineering in Medicine*, vol. 224, pp. 751–763, June 2010.

[138] D. Stoeckel, "Nitinol medical devices and implants," *Minimally invasive therapy & allied technologies*, vol. 9, no. 2, pp. 81–88, 2000.

[139] I. Wanninayake, E. Secco, L. Seneviratne, and K. Althoefer, "A novel probe designed to estimate soft tissue stiffness in mis," in *Workshop on Cognitive Surgical Robotics, IEEE IROS*, 2013.

[140] T. Peters and K. Cleary, *Image-guided interventions: technology and applications.* Springer Science & Business Media, 2008.

[141] R. A. Faust, *Robotics in surgery: history, current and future applications.* Nova Publishers, 2007.

[142] P. E. Gill and W. Murray, "Algorithms for the solution of the nonlinear least-squares problem," *SIAM Journal on Numerical Analysis*, vol. 15, no. 5, pp. 977–992, 1978.

[143] D. W. Marquardt, "An algorithm for least-square estimation of nonlinear parameters," *SIAM Journal on Applied Mathematics*, vol. 11, no. 2, 1963.